Australian Government
Bureau of Meteorology

bushfire&natural HAZARDSCRC

bnhcrc.com.au

IMPROVED PREDICTIONS OF SEVERE WEATHER TO REDUCE COMMUNITY IMPACT

Midterm report 2014-17

Jeffrey D. Kepert, Kevin J. Tory, William Thurston, Dragana Zovko-Rajak, Eng Ching and Robert J. B. Fawcett
Bureau of Meteorology and Bushfire and Natural Hazards CRC

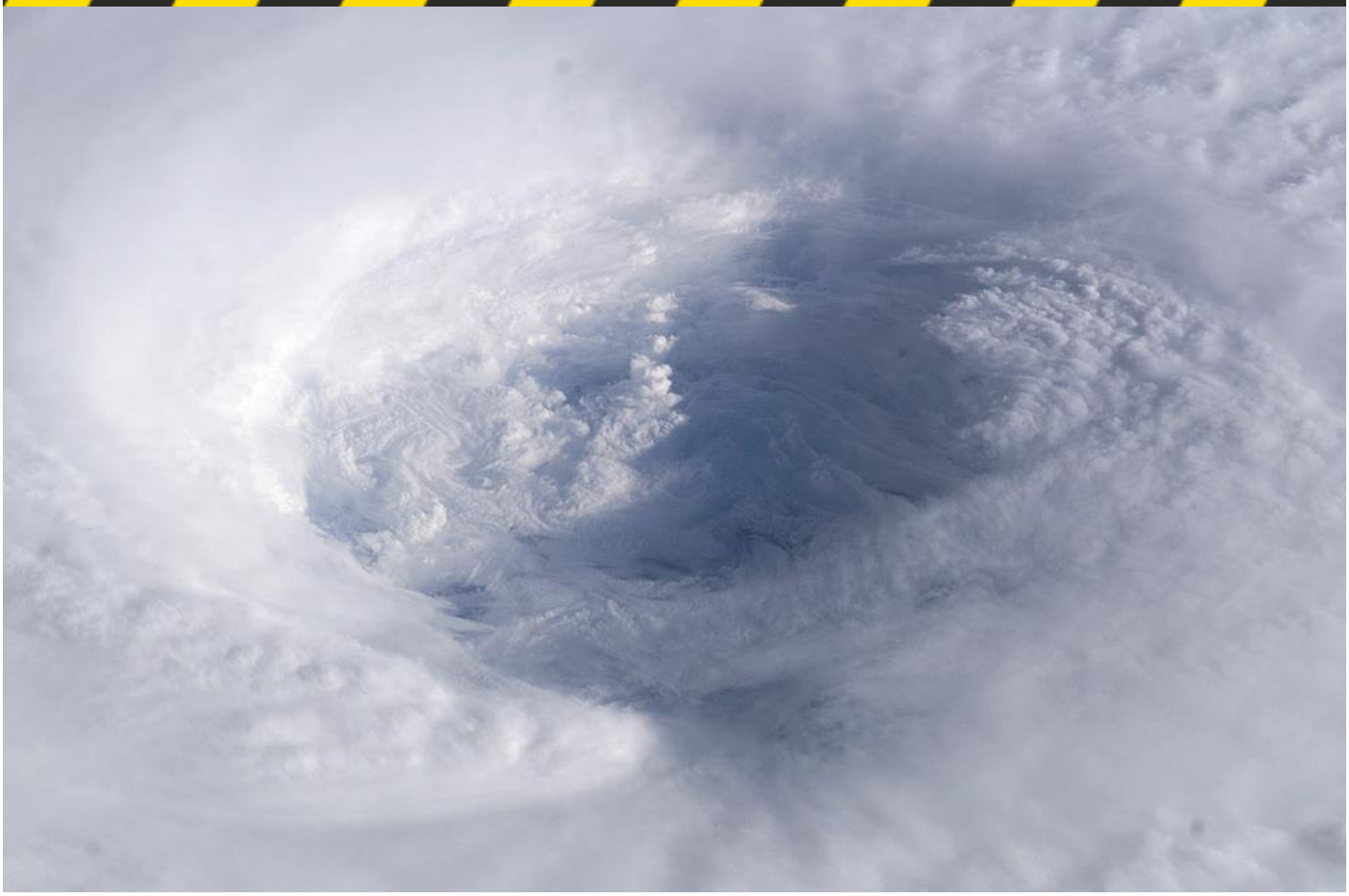

Version	Release history	Date
1.0	Initial release of document	13/09/2017

Australian Government
Department of Industry, Innovation and Science

Business Cooperative Research Centres Programme

Disclaimer:
The Bureau of Meteorology and the Bushfire and Natural Hazards CRC advise that the information contained in this publication comprises general statements based on scientific research. The reader is advised and needs to be aware that such information may be incomplete or unable to be used in any specific situation. No reliance or actions must therefore be made on that information without seeking prior expert professional, scientific and technical advice. To the extent permitted by law, The Bureau of Meteorology and the Bushfire and Natural Hazards CRC (including its employees and consultants) exclude all liability to any person for any consequences, including but not limited to all losses, damages, costs, expenses and any other compensation, arising directly or indirectly from using this publication (in part or in whole) and any information or material contained in it.

Publisher:
Bushfire and Natural Hazards CRC

September 2017

Citation: Kepert JD, Tory KJ, Thurston W, Zovko-Rajak D, Ching E & Fawcett RJB (2017) Improved predictions of severe weather to reduce community impact: annual project report 2016-17. Bushfire and Natural Hazards CRC, Melbourne

Cover: The eye of Hurricane Isabel as seen from the International Space Station

TABLE OF CONTENTS

ABSTRACT

IMPROVED PREDICTIONS OF SEVERE WEATHER TO REDUCE COMMUNITY IMPACT

Jeff Kepert Bureau of Meteorology, Melbourne, Vic

This report marks the end of the initially-approved 3½ years of the project. To mark that milestone, this annual report is much longer than previous annual reports, for it is also the final report of that initial part of the project, and as such contains detailed descriptions of the six main activities in the first 3½ years.

We have studied the dynamics, predictability and processes of severe weather, including fire weather, with the purpose of improving forecasts of severe weather and better depicting forecast uncertainty in these events, thereby facilitating better risk management and more cost-effective mitigation.

Two of the six main chapters of this report relate to our work with large-eddy modelling of turbulent plumes. We have used this technology, in which the model is run on a 50-m grid to capture the most energetic size range of the turbulent eddies, to both simulate ember transport and to model pyrocumulus formation. The mean travel distance of firebrands depends mainly on wind speed and fire intensity, but the spread in the landing positions shifts from being substantially cross-wind at light winds, to dominantly along-wind at high winds. This spread is greatly increased by the turbulence in the plume, and the maximum spotting distance can be more than double the mean for this reason.

We have also used our plume modelling to study pyrocumulus clouds. We have analyzed the processes that lead to pyrocumulus, with special attention on the relative importance of moisture from two sources, the atmosphere and combustion, and shown that the latter is negligible except in very dry environments. This somewhat controversial result has been confirmed by a conceptual study of the thermodynamics of pyrocumulus formation.

We have prepared three detailed studies of severe weather events. East coast lows are intense low-pressure systems that form over the sea adjacent to the east coast of Australia, most commonly along the New South Wales coast. We analyzed the 20-23 April 2015 event using, for the first time, an ensemble of 24 simulations rather than just a single forecast. The use of an ensemble allows us to better discern the degree of risk, and to account for the inherent uncertainty in any forecast. It also enables insight into the processes that lead to the rapid intensification of these systems.

The Blue Mountains fires of October 2013 were most damaging on the 17th. This was expected to be a day of high fire risk, but the extreme fire spread was not anticipated and the causes were unknown. Our high resolution simulations showed that the downward extension of high upper-level winds to the vicinity of the fire ground, caused by mountain wave activity, was a factor. A dry slot – that is, a long, relatively narrow band of dry air – which moved over the fire, further contributed to the conditions.

Lastly, we have analyzed a simulation of a secondary eyewall formation and eyewall replacement cycle in a tropical cyclone, yielding better understanding of the underlying processes and the important factors in predicting these developments. Eyewall replacement cycles are associated with marked expansions of the tropical cyclone wind field, leading to a wider damage swath, earlier onset of damaging winds, and increased storm surge and wave damage.

We are pleased that the project will continue for another three years. Our focus will shift to a greater emphasis on utilization activities during this period. In particular, we aim to develop simple methods of calculating ember transport and pyrocumulus development, so as to transfer the knowledge we have developed in these areas into operations. We will also continue to study severe weather events in detail.

END USER STATEMENT

Paul Fox-Hughes, Bureau of Meteorology, Tasmania

It is a privilege to be asked to write the end user statement for such a successful, wide-ranging and important project within the Bushfire and Natural Hazards CRC.

Over the last three years, the project team, led by Jeff Kepert, have made advances in the science in a number of areas of high-impact severe weather. These advances have applicability, in the first instance, in improved forecaster and emergency manager understanding of severe weather events, and how they may unfold. The team have ensured that awareness of their work has been disseminated widely within operational meteorologist and emergency management end-user groups through a number of presentations in a variety of different forums, and through scientific and summary publications targeting not only the research community but also practitioners.

It is useful to highlight some of the specifics of the topics examined by the team during the course of the project. Using a Large Eddy Model, the team investigated spotting and pyrocumulus at very high spatial resolution, of the order of tens of metres. This is very computationally intensive, and is not feasible to attempt in real time. However, the insights gained from this modelling have opened a path to parametrising the processes involved, so as to build very simple models that exhibit most of the behaviours of the more detailed simulations and can be run in an operational environment. Both spotting and pyrocumulus are important processes in fire behaviour modelling, and need simple, reliable models for fire meteorologist and fire behaviour analyst use in operations. This work has taken a large step in that direction.

The pyrocumulus work, in particular, resulted in the unexpected conclusion that pyrocumulus development is strongly dependent on moisture from the atmospheric environment, rather than from the underlying fire. This has led to a closer examination by the research team of the thermodynamics of pyrocumulus formation, and the first steps in development of numerical weather prediction guidance to identify regions particularly prone to pyroconvection on any given day – a very exciting, practical and direct application of the work done by the severe weather research team.

On a completely different tack, the research team's case study of the Dungog east coast low (ECL) of April 2015 has provided insights into ECL dynamics, as well as the potential for operational use of forecast ensembles. Low-level onshore jet intensification, for example, occurred as a result of the development of a strong pressure gradient between the low evolution itself and upper-level ridging descending to near-surface levels. The 24-member 1.3 km resolution modelling pointed to the extent of the predictability of the ECL development, and to ways that operational meteorologists and emergency managers can employ ensembles to better forecast severe weather events, knowledge that is important with the increasing use of ensembles in operational forecasting.

These outputs alone would have justified the investment of time and resources into the project. However, there are several additional outputs that are each significant research accomplishments: a case study of the 2013 State Mine fire in NSW revealed the importance of mountain wave activity during (unusually) daylight hours to rapid fire progress and the non-typical formation of a band of dry air that impacted on the fire; and teasing apart the role of frictional convergence and convection in the development of tropical cyclone eyewall replacements has contributed substantially to greater understanding of this process, which can affect up to 50% of intense TC's.

In summary, the "Improved Predictions of Severe Weather to Reduce Community Impact" project team have, in the first three and a half years of the CRC, delivered outstanding value in enhanced understanding of severe weather events, and in pointing to better means for their prediction.

INTRODUCTION AND BACKGROUND

This project aims to study the dynamics, predictability and processes of severe weather, including fire weather. We seek also to improve forecasts of severe weather, and to better depict forecast uncertainty in these events, thereby facilitating better risk management and more cost-effective mitigation. Our studies span a range of time and space scales and require a range of different methods.

Extreme weather often occurs at relatively small scales – here, the devil really is in the detail. Even when the meteorology driving the event is not small scale, small-scale perturbations within the overall framework can have a significant effect. Accurate forecasts and understanding of such small-scale processes requires high-resolution modelling. Developing and validating such modelling, and extending it to all hazards, is the first aim of this project.

Forecasts are never perfect, but they are nevertheless useful. Forecasts are especially useful in severe weather events, since they play an essential role in allowing communities, industry and emergency services to prepare and mitigate the impacts. Forecasting therefore underpins the work of emergency services and related agencies, and makes the PPRR (Prevention, Preparedness, Response and Recovery) process more efficient and effective. Because forecasts are inherently uncertain in the severity, location and duration of an event, preparation needs to be more widespread than the eventual impact – but this over-preparation comes at a cost. Detailed prediction of the probabilities of severe impacts would avoid the risk of failing to alert areas with the chance of an impact, while minimising the cost of over-warning. Thus the second aim of this project was to provide pilot predictions of not just the most likely course of events, but also the level of uncertainty, by identifying plausible alternative scenarios and their likelihoods.

A key aim of this project is to develop scientific understanding and to assist with the "lessons learned" from severe events. Our research thus adds to the collective wisdom of fire fighters, emergency services personnel and weather forecasters, improving our ability to manage these events and reducing the risk of adverse outcomes in the future.

The principal numerical weather prediction (NWP) modelling system used in this project is ACCESS, the Australian Community Climate and Earth-System Simulator. ACCESS is used operationally within the Bureau of Meteorology and is based on the UK Met Office's NWP system. Several other overseas national weather services similarly use this system. ACCESS therefore benefits from a wide user base, and the discipline of operational use and continual verification. The Met Office system is presently the second-best performing operational NWP system in the world, and the only system to consistently outperform it for global prediction is a global-only model which cannot be run in the high-resolution limited-area mode necessary to simulate fine-scale meteorology.

For situations where extremely high resolution modelling with a grid spacing of tens of metres, and the capacity to explicitly resolve atmospheric turbulence is needed, we use the UK Met Office's Large-Eddy Model (LEM). This specialised

model is designed not for forecasting, but rather for understanding phenomena that are highly sensitive to turbulence, including boundary layers, fire plumes and convective clouds.

Our ember transport work has confirmed that the mean travel distance of firebrands for a given fire intensity depends mainly on wind speed. However, the spread in the landing positions shifts from being substantially cross-wind at light winds, to dominantly along-wind at high winds. This spread is greatly increased by the turbulence in the plume, and the maximum spotting distance can be more than double the mean for this reason. A paper describing this work has been published in the *International Journal of Wildland Fire* (Thurston et al. 2017).These sophisticated and computationally intensive ember transport calculations can be used to inform the development of physically realistic and computationally cheap parameterizations of ember transport for use in fire models.

We have also used our plume modelling to study pyrocumulus clouds. Intense fire plumes in suitably moist environments can lead to cloud development, with the possibility of strong downbursts. We have analyzed the processes that lead to pyrocumulus formation, with particular attention to the relative importance of moisture from two sources, the atmosphere and combustion, and shown that the latter is negligible except in very dry environments. This result was something of a surprise to us, and is certainly controversial. We were prompted to better understand the thermodynamics – that is, the interaction of fire heat and moisture with that from the atmosphere – in pyrocumulus, resulting in a detailed study of the basic underpinning processes, which confirmed our large-eddy simulation results. Manuscripts are in advanced preparation on both the pyrocumulus modelling and the thermodynamic analysis. We aim to use the knowledge gained to develop a forecast tool for pyrocumulus formation. The lack of sensitivity to fire moisture has important practical implications – fire moisture is not well characterized, and would otherwise present a barrier to a forecasting system. However, our work shows that the forecasts will be insensitive to the value used, thereby simplifying the forecast process and increasing its accuracy.

We have made substantial progress on our case study of the April 2015 east coast low, which produced severe flooding, winds and coastal erosion on the north coast of NSW. This study is the first we have undertaken using ensemble modelling, and the results of this study, as well as helping to understand the dynamics of this event, will also help guide users to make better use of this coming data source in the future. The ensemble dataset has demonstrated many of the benefits of ensemble modelling which are becoming well known – for instance, the fact that the ensemble mean tends to be a more accurate forecast, and that it provides the ability to compute probabilities and to consider a range of possible scenarios in responding to an event. It also enables a more rigorous approach to understanding the underlying meteorological processes. Often, we tentatively conclude that two factors which occur together also have some causal relationship, but since we have only one simulation cannot be certain. Now, we can examine the full ensemble for this association and potentially increase our confidence.

We completed a detailed analysis of the meteorology of the Blue Mountains fires of October 2013, focusing on the most severe weather conditions and damaging fire activity of that event, the State Mine fire on October 17. We found two meteorological factors that likely contributed to the fire conditions on that day, mountain waves and a dry slot of unusual origin. The occurrence of mountain waves was interesting, since this was the third severe fire case in which we have made this link, and the first that occurred during the day rather than at night. Although this link has been suggested before, actual examples have been very thin on the ground, so we prepared a Hazard Note on mountain wave influence on bushfires, discussed further below.

About half of all intense tropical cyclones experience an eyewall replacement cycle, in which a new eyewall forms concentrically around the existing one and then contracts, eventually replacing the original eyewall. These events cause an initial weakening, followed by a re-intensification of the storm, and are associated with a marked expansion of the wind field, and hence broadening of the damage swath and increase in storm surge. We are investigating a high-resolution simulation of an eyewall replacement cycle, with a particular focus on the role of boundary-layer convergence and its interaction with convection. Changes in the internal structure of tropical cyclones cause difficulties with their mitigation, particularly approaching landfall, so improved knowledge of a major cause of such change will lead to better forecasts and mitigation.

We undertook a significant utilization activity this year with the publication of a *Hazard Note* on the effects of mountain waves on bushfires. This work drew on our analysis of the State Mine fire, as well as previous work on the Ellensbrook and Aberfeldy fires for the former Bushfire CRC. In it, we discussed how mountain waves can lead to strong winds on the lee slope of a hill or mountain, which are often stronger at night, contrary to the normal diurnal cycle. This *Hazard Note* drew considerable attention, and the material has subsequently been adapted for the Bureau of Meteorology's blog, for a feature article in *Fire Australia*, and for an article in the *Weekly Times*. It can be difficult to foresee where a piece of research will lead, but we are very pleased that this work has clearly struck a chord with people exposed to or responsible for managing fire risk, and we trust it will lead to improved mitigation in the future.

This project has now reached the end of its original term. All major deliverables have been met with the exception of some journal article writing, which are well advanced but not quite complete. We expect to complete one more journal article than the original project plan called for, due to the extra work on pyrocumulus. We are very pleased that the BNHCRC has decided to extend the project for an additional 3 years. This extension will allow us to become more focused on utilization activities, particularly arising from the fire plume work where we plan to turn our improved knowledge of plume effects on ember transport and pyrocumulus formation into practical forecasting tools.

This report is not just the annual report for the 2016-17 year, but is also the final report for the originally-approved project. As such, it is longer and more detailed than our previous annual reports. It comprises six main chapters, framed around our research areas. We would like especially to draw the readers' attention to the "practical implications" section at the end of each of those chapters.

THE EFFECTS OF TURBULENT PLUME DYNAMICS ON LONG-RANGE SPOTTING

This chapter is adapted from our paper at the 2016 AFAC conference, *Thurston, W., K.J. Tory, R.J.B. Fawcett and J.D. Kepert, 2016: The effects of turbulent plume dynamics on long-range spotting.* A fuller account can be found in *Thurston et al. (2017)*.

INTRODUCTION

Fire spotting is a hazardous phenomenon which leads to unpredictable fire behaviour and accelerated fire spread. Spot fires occur when embers are launched by bushfire plumes into the background wind, which then carries the embers a significant distance from the fire front. If the embers land in a suitable fuel bed and are still burning a spot fire is ignited. The magnitude of the problem is illustrated by Cruz et al. (2012), who provide evidence of long-range spotting in excess of 30 km during the Black Saturday bushfires of February 2009. Therefore a better understanding of the processes that contribute to long-range spotting is essential for the prediction of fire spread. In this contribution we aim to assess the contribution of turbulent plume dynamics to the process of long-range spotting.

METHODOLOGY

We use a two-stage modelling approach to calculate the landing positions of potential firebrands launched by bushfire plumes. Firstly, we use the UK Met Office large-eddy model (LEM), described by Gray et al. (2001), to perform numerical simulations of idealised bushfire plumes. A number of plumes are simulated for background winds varying from 5 to 15 m s^{-1}. Secondly, the three-dimensional, time-varying velocity fields produced by the LEM are used to drive a simple Lagrangian particle-transport model. Potential firebrands are released near the base of the plume and then advected by the LEM velocity field with a constant fall velocity of 6 m s^{-1} applied, representative of jarrah and karri bark flakes (Ellis, 2010). The time-varying particle-transport calculations are then repeated using a steady plume velocity, calculated from the one-hour mean plume fields, in order to assess the contribution of the in-plume turbulence to the firebrand transport.

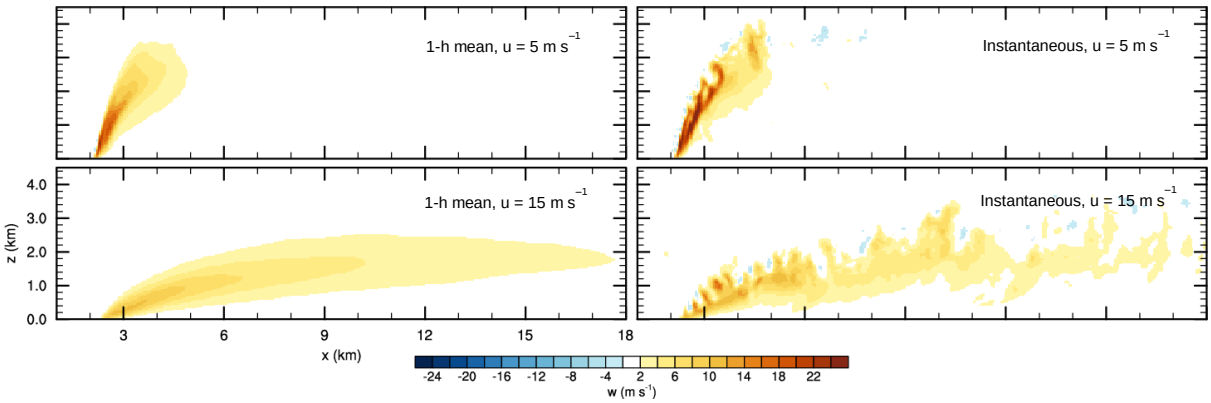

Figure 1. Vertical cross-sections of the mean (left) and instantaneous (right) vertical velocity, m s^{-1}, through the plume centre line, for background wind speeds of 5 (top) and 15 (bottom) m s^{-1}.

RESULTS

Vertical cross sections of the instantaneous and 1-h mean updrafts for plumes in the weakest (5 m s^{-1}) and strongest (15 m s^{-1}) background winds are shown in Figure 45. The instantaneous plumes in strong wind have weaker updrafts, and are more bent over than the plumes in weak wind. The instantaneous strong-wind plume is turbulent over its whole height, whereas its weak-wind counterpart is only turbulent above a height of about 2 km. Plan views of the weak-wind plume, not shown here but seen in Thurston et al. (2014), reveal that the plume has two updraft cores that form a counter-rotating vortex pair. The 1-h mean plumes do not exhibit any of the turbulence that is visible in the instantaneous plume updrafts, and as a result have a weaker peak updraft.

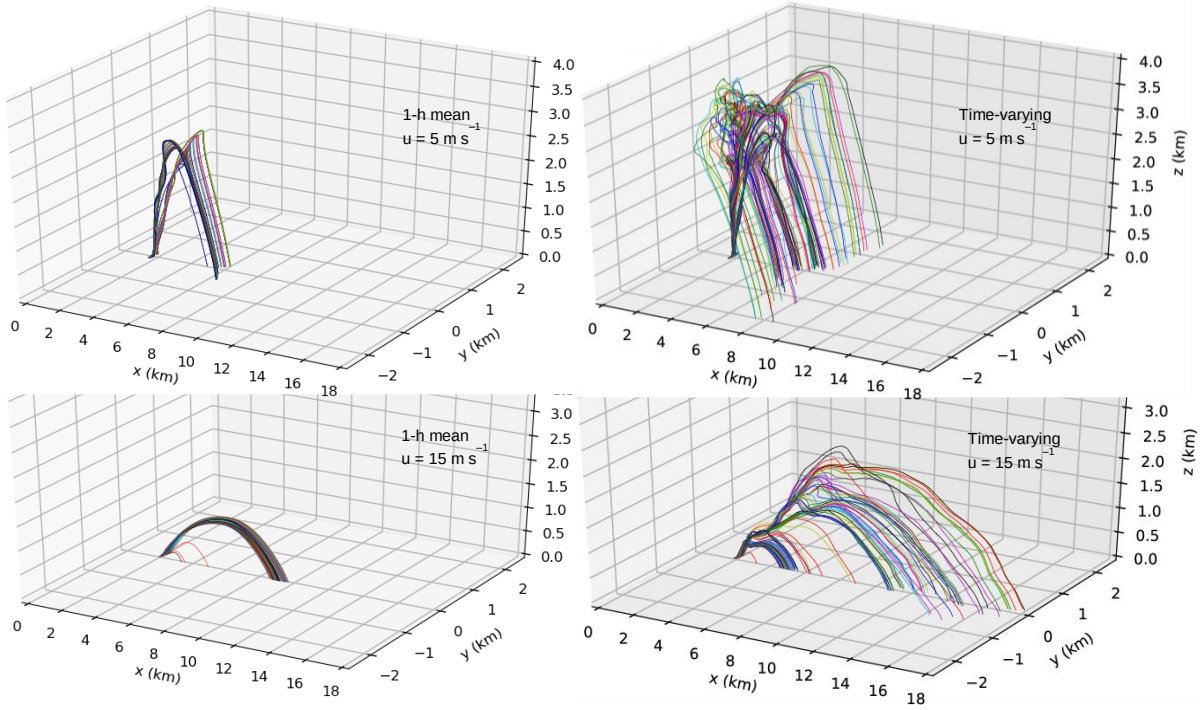

Figure 2. Trajectories of 100 firebrands lofted by the mean (left) and time-varying (right) plumes under background wind speeds of 5 (top) and 15 (bottom) m s–1.

The trajectories of 100 firebrands lofted by each of the plumes in Figure 1 are shown in Figure 2. Firebrands lofted by the time-varying weak-wind plume initially travel up the two branches of the counter-rotating vortex pair, and are then spread out further laterally as the reach the turbulent region of the plume above a height of 2 km. Firebrands lofted by the time-varying strong-wind plume do no exhibit any of this lateral spread, instead landing near the plume centre line. These firebrands appear to be lofted in clumps by the turbulent puffing of the plume, and hence tend to fall out in clusters. The trajectories of firebrands lofted by the 1-hr mean plumes highlight the importance of the in-plume turbulence. In the weak-wind case the firebrands still travel up the two branches of the counter-rotating vortex pair, but there is less lateral dispersion above 2 km. In the strong-wind case the effect of the in-plume turbulence is more pronounced, with most firebrands now having similar trajectories.

Figure 3 shows the two-dimensional landing distributions for 1.5 million firebrands launched by each of the plumes in Figure 1. The counter-rotating vortex pair and upper-level turbulence of the time-varying weak-wind plume lead to the firebrands landing in a V-shaped pattern with considerable lateral spread. The landing positions of firebrands lofted by the 1-h mean plume in weak winds still land in a V-shaped pattern, but there is less lateral spread due to the lack of in-plume turbulence. Firebrands lofted by the time-varying strong-wind plume travel on average about twice as far as their weak-wind plume counterparts, have more longitudinal spread and less lateral spread in their landing distribution. The landing positions of firebrands lofted by the 1-h mean plume in strong winds show much less spread and crucially the maximum spotting distance is reduced by half from about 16.7 km to 8.4 km.

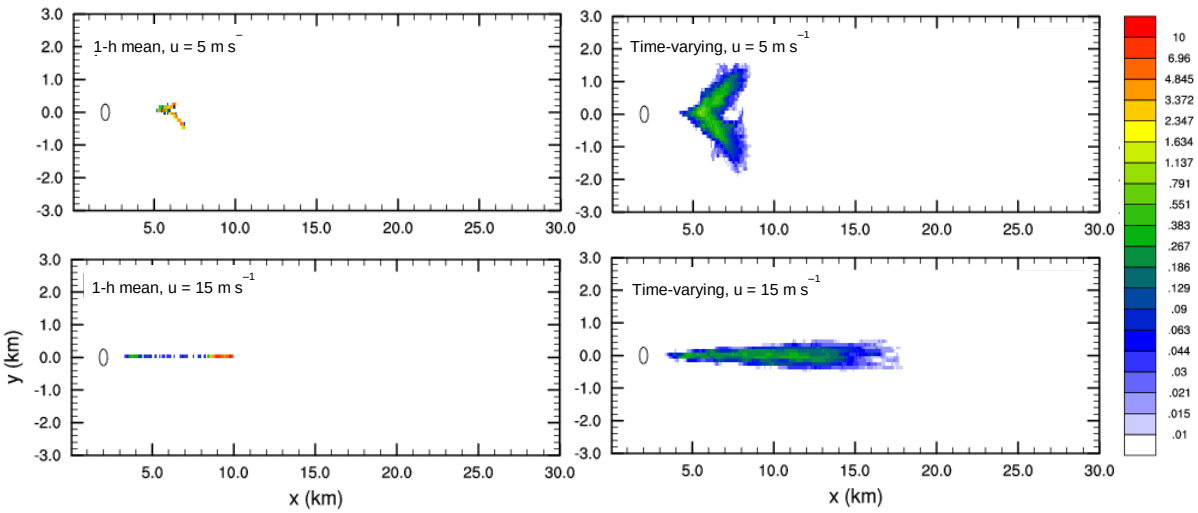

Figure 3. Spatial distributions of firebrand landing position (percent of particles launched per km2) for the mean (left) and time-varying (right) plumes under background wind speeds of 5 (top) and 15 (bottom) m s–1

A critical consideration in the potential for firebrands to start spot fires is whether they are still burning when they land. Therefore the flight times of the firebrands lofted by the time-varying weak-wind and strong-wind plumes are presented in Figure 4. Firebrands that are lofted by the weak-wind plume have a relatively long flight time, even if they do not travel a long distance. For example firebrands that are lofted by the weak-wind plume and subsequently travel only

0—2 km are in the air for 7.5—12.5 minutes, whereas firebrands that are lofted by the strong-wind plume and travel only 0—2 km are in the air for 1.5—3.5 minutes. This caused by the plume dynamics seen in Figure 1: the weak-wind plume is more upright and has a stronger updraft, causing the firebrands to go almost straight up, reach a greater height and therefore be in the air for longer. This behaviour is confirmed by the trajectory plots of Figure 2. The firebrands that have travelled the furthest (16—18 km, in the strong-wind case) have a median flight time of 21.5 minutes and a 1st—99th percentile range of 19.3—23.4 minutes. This is of the order of the maximum burnout time of ribbon gum bark observed in the wind tunnel studies of Hall et al. (2015) and would suggest that firebrands that took these trajectories would still be capable of starting spot fires.

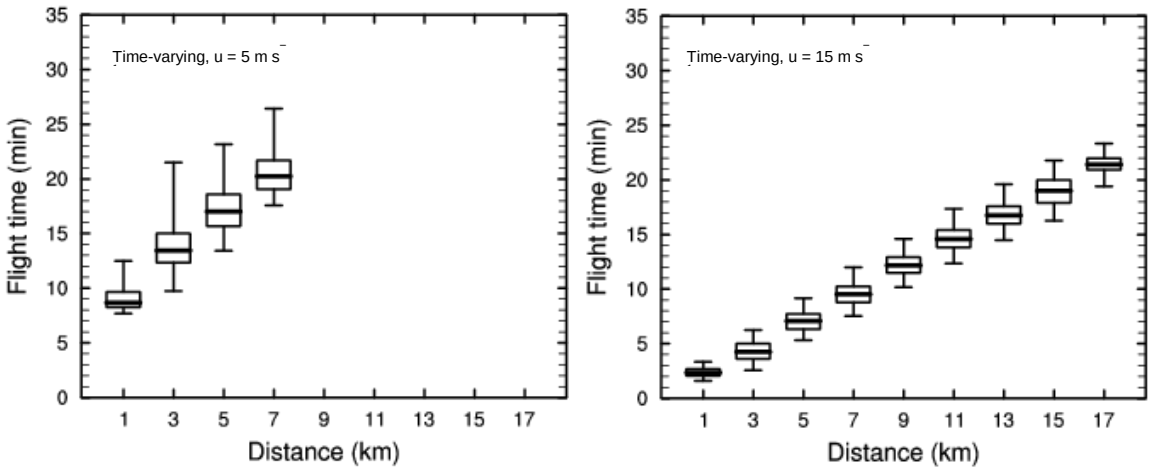

Figure 4. Box and whisker plots of flight times for firebrands lofted by the time-varying plumes under background wind speeds of 5 (left) and 15 (right) m s^{-1}. Flight times are binned according to the distance travelled by the firebrand, at 2 km intervals. The thick line shows the median flight time and the box spans the interquartile range. Whiskers represent the 1st and 99th percentile flight time.

SUMMARY

We have combined large-eddy simulations of bushfire plumes with Lagrangian particle transport modelling to investigate how turbulent plume dynamics can affect long-range spotting. Plumes exhibited different dynamical and turbulent behaviour depending on the background wind conditions and this consequently leads to differences in firebrand transport. Plumes in weak winds contain a counter-rotating vortex pair which leads to large lateral spread in firebrand landing position. Plumes in strong winds are more turbulent and bent over, leading to more longitudinal spread in firebrand landing position and a greater maximum spotting distance. In-plume turbulence was shown to substantially reduce the lateral and longitudinal spread in firebrand landing position and in the case plumes in strong background winds, reduce the maximum spotting distance by a half. Systematic studies such as this will inform the development of better empirical spotting models.

PRACTICAL IMPLICATIONS

This work has highlighted the processes that affect long-range ember transport, and we now have the necessary underpinning knowledge to develop an operational technique for calculating this important process. However, the present calculation is much too computationally expensive to be operationally feasible. Therefore, we will be developing a much simpler model, which nevertheless will incorporate the key important physical processes which this work has revealed. This model will be computationally cheap enough to be used in the field, or as part of a fire spread simulator.

LARGE-EDDY SIMULATION OF PYROCUMULUS

This chapter is adapted from our draft manuscript, *Thurston, W., K.J. Tory and J.D. Kepert, 2017: The modest role of pyrogenous moisture in pyrocumulus development.*

SUMMARY

Pyro-convective clouds have the potential to increase surface rates of wildfire spread, enhance ember transport, generate lightning and tornadic storms, and alter Earth's radiative balance through the stratospheric injection of combustion products. It is well known that sufficient moisture is required for a buoyant plume above a wildfire to generate pyro-convective cloud, and indeed this happens with some degree of regularity. However, the typical source of this moisture is less clear, with conflicting evidence available regarding the significance of pyrogenous moisture (that is, moisture released by combustion) in the development of moist pyro-convection. Here we attempt to fill this knowledge gap by quantifying the relative importance of environmental and pyrogenous moisture in pyrocumulus development. We expand upon previous case-study-based modelling approaches by performing large-eddy simulations of buoyant wildfire plumes of different intensities and over the parameter space of environmental moisture and pyrogenous moisture. Intense fires in sufficiently moist atmospheres can produce pyro-convective cloud in the absence of any moisture from the combustion process and the cloud is deeper for the more-intense fires and moister atmospheres. The addition of pyrogenous moisture only has a small effect on the development of pyro-convective cloud. Further analysis reveals that this is due to substantial entrainment of relatively dry environmental air into the sub-cloud buoyant plume. Entrainment dilutes pyrogenous moisture to the extent that very little remains once the plume has ascended to the level of the cloud base, suggesting that relative to environmental moisture, pyrogenous moisture plays only a modest role in pyrocumulus development. This has implications for forecasting pyro-convective cloud and its impacts.

INTRODUCTION

Intense heating of the air in the vicinity of a wildfire causes deep ascent. If deep enough to raise air above the lifting condensation level, this ascent leads to the formation of pyrocumulus (pyroCu) or pyrocumulonimbus (pyroCb). The generation of such pyro-convective cloud by wildfire plumes is significant because of the many ways in which it can potentially influence fire behavior. For example, moist pyro-convection has been associated with (i) amplified burn and spread rates (Peterson et al., 2015); (ii) tornadogenesis (McRae et al., 2013); (iii) ignition of new fires by pyroCb lightning, noting that pyroCb lightning conditions favor hotter and longer-lived lightning strikes (Rudlosky and Fuelberg, 2011); and (iv) enhanced spotting potential due to deeper and stronger updrafts (e.g., Koo et al., 2010) as a result of latent heat release in the convective column. The invigorated updrafts in moist pyro-convection are also capable of penetrating the tropopause, leading to stratospheric injection and

hemispheric-scale transport of aerosol and other combustion products (Fromm et al., 2006, 2010). Therefore, knowledge of the processes that contribute to the development of moist pyro-convection in wildfire plumes is an important component in understanding the behaviour of fires, their impacts and potential climatic influences.

Here we use large-eddy simulations to investigate the generation of pyro-convective clouds by buoyant wildfire plumes. Firstly, we perform simulations over a range of fire intensities and environmental moisture levels. We then repeat a subset of these simulations with differing amounts of pyrogenous moisture, allowing us to assess the relative importance of environmental moisture and fire-derived moisture in the development of pyro-convective clouds.

METHODOLOGY

The Large-Eddy Model

The simulations presented here are performed with Version 2.4 of the UK Met Office Large-Eddy Model (LEM). The LEM is a high-resolution cloud-resolving model which solves a quasi-Boussinesq, anelastic, equation set on a three-dimensional Cartesian grid. Sub-grid stresses are parametrized using a stability-dependent version of the Smagorinsky-Lilly scheme, described by Brown et al. (1994). Moist processes are represented by the three-phase microphysics scheme of Swann (1998), which accounts for phase changes between vapour, liquid (cloud and rain) and frozen (snow, ice and graupel) water species. Our simulations are performed without any radiation parametrization and the Coriolis force is also neglected, a reasonable assumption given the scale of the plumes simulated here. For further details about the LEM, the reader is referred to Gray et al. (2001) and references therein.

The LEM has traditionally been used to simulate a wide range of common turbulent and cloud-scale atmospheric phenomena, from the dry, neutral boundary layer (e.g. Mason and Thomson, 1987) to tropical deep convection (e.g. Petch and Gray, 2001), although more recently it has been used to study the behaviour of buoyant plumes from fires. Devenish and Edwards (2009) used the LEM to perform simulations of the Buncefield oil depot fire in the United Kingdom, the largest fire in Europe since the Second World War. The model was able to successfully reproduce the observed height and multi-directional spread of the plume. Devenish et al. (2010) performed further validation by comparing the entrainment and radial spreading rates of buoyancy and vertical velocity in LEM-simulated plumes to theoretical plume models.

All simulations presented here are performed on a model domain of 256 by 256 grid points in the horizontal, with a uniform horizontal grid length of 50 m, resulting in a domain size of 12.8 km by 12.8 km. The domain has a stretched vertical grid of 256 points in the vertical, with a vertical grid length of 20 m near the surface, increasing smoothly to 50 m at a height of 1.5 km. The vertical grid length is constant at 50 m between heights of 1.5 and 10 km and then smoothly increases to 60 m between 10 km and the model top, which is situated at 12.7 km. The lateral boundary conditions of the model are doubly periodic and a

no-slip condition is applied at the lower boundary, with a specified roughness length of 0.05 m. A free-slip condition is applied at the upper boundary of the model domain in conjunction with a Newtonian damping layer in the top 2.5 km of the domain, to prevent the reflection of vertically propagating gravity waves. The horizontal extent of the domain is sufficient that over the duration of the simulations presented here the pyro-convective clouds are not affected by the periodic lateral boundary conditions. None of the pyro-convective clouds deepen enough to encounter the Newtonian damping layer near the model top.

Experimental design

The wildfire plumes presented here are simulated using a two-stage process. The first stage is a "spin-up" phase, in which a realistic atmospheric boundary layer is generated. The model output at the end of the spin-up phase is then used as a set of initial conditions for the second stage, in which the buoyant plume from a wildfire is simulated.

At the beginning of stage one the model is initialized with horizontally homogeneous conditions, designed to be representative of a high fire danger day. An initial potential temperature profile is specified, consisting of a 4.0-km deep well-mixed layer with a constant value of 310 K. Above this, a troposphere with a constant lapse rate of 3 K km^{-1} is specified from the top of the mixed layer to the model top. The initial water vapour mixing ratio profile is also specified as a constant value throughout the 4.0-km deep well-mixed layer, and then reduced above the mixed-layer top at a rate such that the relative humidity remains constant throughout the troposphere. The model is initialized with zero environmental wind, allowing us to concentrate on the effects of the thermodynamics on the formation of pyro-convective cloud.

In order to explore the sensitivity of the development of moist pyro-convection to the environmental moisture, a range of simulations is performed in stage one. These simulations differ only in their initial value of the water vapour mixing ratio. Five simulations are performed, with constant mixed-layer water vapour mixing ratios, q_{vML}, of 2.0, 2.5, 3.0, 3.5 and 4.0 g kg−1. Random perturbations, with maximum amplitude of ±0.1 K, are added to the initial potential temperature field within the atmospheric boundary layer, in order to break the model symmetry and promote the development of turbulence, and a sensible heat flux of 50 W m^{-2} is applied uniformly at the surface. The model is then integrated forward in time with a variable time-step, determined by the Courant–Friedrichs–Lewy condition, until the boundary layer has spun up to a quasi-steady state, as determined by the time-series of the domain-average turbulent kinetic energy (TKE). At the end of the spin-up period we have five sets of initial conditions for use in stage two of the process, the simulation of wildfire buoyant plumes. These initial conditions are shown in Figure 5, in which the temperature and dew point traces together form the classic inverted-V profile, which is characteristic of conditions under which pyro-convective cloud forms (e.g. Peterson et al., 2017).

Then, in stage two of the simulation process we take the model state at the end of the first stage of the simulation and generate a buoyant wildfire plume, using the method employed by Devenish and Edwards (2009). A sensible heat flux

anomaly is applied at the model lower surface boundary over a circular area of radius 250 m, located in the centre of the model domain, equidistant from both lateral boundaries. It should be noted that there is no direct feedback of the atmosphere back onto the fire in these simulations and therefore no capacity to simulate fire spread. This means that in this configuration it is possible to isolate and consider only the interaction between the buoyant plume and the thermodynamic environment in which it exists, without the extra complication of surface-based fire behaviour feedbacks.

Fires of four different intensities, Q, of 5, 10, 20 and 30 kW m^{-2} are simulated and in each case the heat flux is linearly ramped up from zero to its peak value over five minutes, held constant for one hour, and then linearly ramped down back to zero over five minutes. The combination of five different environmental moisture profiles and four different fire intensities gives us twenty simulations in total. We denote these simulations "dry" fires, as there is no representation of the pyrogenous moisture flux, either from moisture within the fuels or from the combustion process itself. These dry fires permit the assessment of the sensitivity of pyro-convective cloud to environmental moisture and fire intensity.

Additionally, a set of "wet"-fire simulations is performed, in which all five Q = 30 kW m^{-2} dry-fire simulations are repeated twice, once with a latent heat flux, L_E, of 2.1 kW m^{-2} and once with L_E = 11.4 kW m_{-2}. These values are chosen to represent the range of realistic ratios of heat to moisture fluxes in wildfires, based on the calculations of Luderer et al. (2009), and are denoted the "least-moist" and "most-moist" fires, respectively. These wet fires permit the assessment of the sensitivity of pyro-convective cloud to pyrogenous moisture, and in combination with the dry fires an assessment of the relative roles of environmental and pyrogenous moisture.

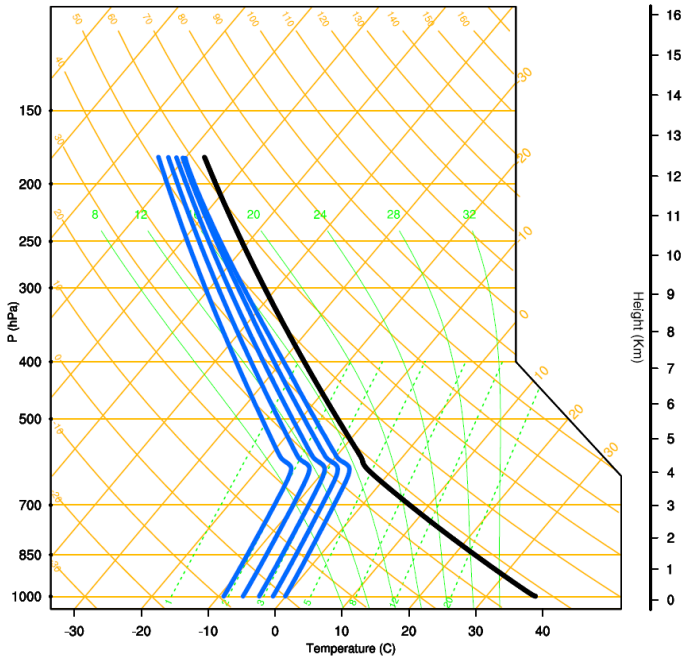

Figure 5. Skew-T log-p diagrams of the environmental atmospheric conditions spun up at the end of stage one. All simulations have the same temperature profile, shown in black, and the five different dew-point profiles are shown in blue.

RESULTS

"Dry" fires

Figure 6 shows a snapshot from the Q = 30 kW m^{-2} fire intensity and q_{vML} = 4.0 g kg^{-1} mixed-layer water vapour mixing ratio simulation, 22 minutes after the fire has reached maximum intensity. This is the simulation with the moistest background conditions and the highest fire intensity. The wildfire buoyant plume has a strong updraft throughout most of the extent of the boundary layer, with a maximum vertical velocity in excess of 25 m s^{-1} (Figure 6 (a)). The plume decelerates as it penetrates into the stably stratified troposphere, but the ascent is deep enough to trigger the formation of a pyro-convective cloud. The cloud base is located at 4.5 km above ground level (AGL) and the cloud extends to an altitude of 7.5 km AGL (Figure 6 (c)). Although the updraft core of the buoyant plume is reasonably slender within the boundary layer, the horizontal extent of the pyro-convective cloud is much greater, having a width in excess of 3 km (Figure 6 (d)).

Extensive condensation within the cloud, particularly notable in the liquid water mixing ratio field around (x, z) = (0.5, 6.5) km, leads to the release of latent heat which is evident in the potential temperature perturbation field at the same location (Figure 6 (b)). There is a co-located updraft greater than 10 m s^{-1} within the pyrocumulus cloud, which is separated from the main plume updraft within the boundary layer. This resurgence of the updraft is due to latent heat release increasing the local plume buoyancy.

Figure 7 shows a snapshot of the liquid water mixing ratio vertical cross-sections for all twenty combinations of Q and q_{vML}, at 22 minutes after the fires have reached full intensity. The potential formation of a pyro-convective cloud and the properties of that cloud are dependent on both the intensity of the fire and the environmental moisture. Pyrocumulus is more likely to form if the environment is moist and the fire intensity is high. The size of a pyro-convective cloud and its cloud-top height both increase with environmental moisture and fire intensity. In the driest environment, with a mixed-layer water vapour mixing ratio of 2.0 g kg^{-1}, pyro-convective cloud only forms for the most intense fire and the cloud that does form is very small. As the environmental moisture increases, pyro-convective cloud forms for weaker and weaker fire intensity, and by the time the mixed-layer water vapour mixing ratio reaches the maximum value of 4.0 g kg^{-1}, pyro-convective cloud forms for all values of fire intensity. For fixed fire intensity, increasing the mixed-layer water vapour mixing ratio lowers the cloud-base height, from 5.7 km AGL for the driest to 4.5 km AGL for the moistest. Conversely for a fixed mixed-layer water vapour mixing ratio, increasing the fire intensity does not substantially affect cloud-base height.

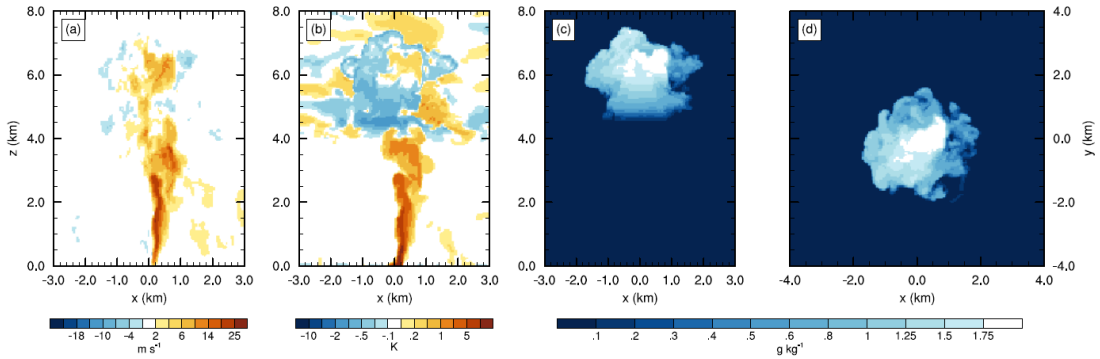

Figure 6. Vertical cross-sections of the instantaneous (a) plume vertical velocity, m s^{-1}, and (b) plume potential temperature perturbation, K, both in the y = 0 plane. Instantaneous liquid water mixing ratio, g kg^{-1}, maximum values in the (c) y− and (d) z−directions. All plots are shown at 22 minutes after the fire has reached full intensity and are for the Q = 30 kW m^{-2} fire intensity and qv = 4.0 g kg^{-1} mixed-layer water vapour mixing ratio case.

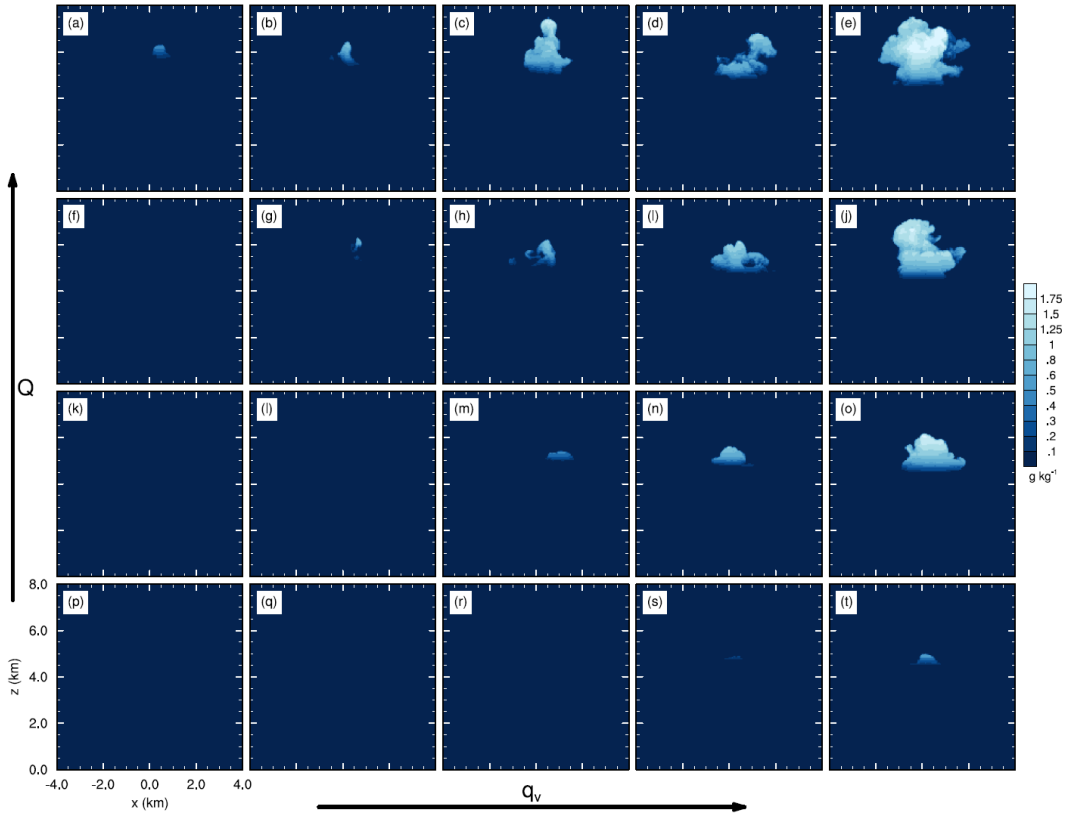

Figure 7. Vertical cross-sections of the maximum instantaneous liquid water mixing ratio in the y−direction, g kg^{-1}, at 22 minutes after the fires have reached full intensity. Panels show all twenty combinations of fire intensity, Q = (5, 10, 20, 30) kW m^{-2}, arranged vertically and mixed-layer water vapour mixing ratio, qvML = (2.0, 2.5, 3.0, 3.5, 4.0) g kg^{-1}, arranged horizontally. Fire intensity increases from the bottom row of panels to the top row of panels and boundary-layer water vapour mixing ratio increases from the left-hand column of panels to the right-hand column of panels, as indicated by the arrows.

"Wet" fires

Snapshots of the liquid water mixing ratio vertical cross-sections for all five Q = 30 kW m^{-2} fire intensity simulations, with latent heat fluxes LE of 0.0, 2.1 and 11.4 kW m^{-2} at 22 minutes after the fires have reached full intensity are shown in Figure 8. The effect of adding a latent heat flux to the fire is very small, slightly increasing cloud amount and cloud top height, for all of the mixed-layer water vapour mixing ratios shown.

To investigate why the addition of a moisture source, in the form of a latent heat flux, to the fire has only a small effect on pyrocumulus formation, we construct time-height diagrams of the maximum water vapour mixing ratio at each model level (Figure 9). In the zero latent heat flux case the boundary-layer water vapour mixing ratio is constant throughout the simulation and the lifting of the boundary layer air by the plume into the relatively dry free troposphere is evident after about 10 minutes. In the L_E = 2.1 kW m^{-2} case, the water vapour mixing ratio is greater near the surface, above which the moisture becomes more diffused with height and is similar to the zero latent heat flux case. Even in the L_E = 11.4 kW m^{-2} case, the moisture released by the fire is only just reaching the top of the boundary layer, where it is then able to have a minimal effect on pyrocumulus formation. The amount of moisture that gets transported upwards in the L_E = 11.4 kW m^{-2} case is made clear by the difference plot of time-height water vapour mixing ratio in Figure 9 (d).

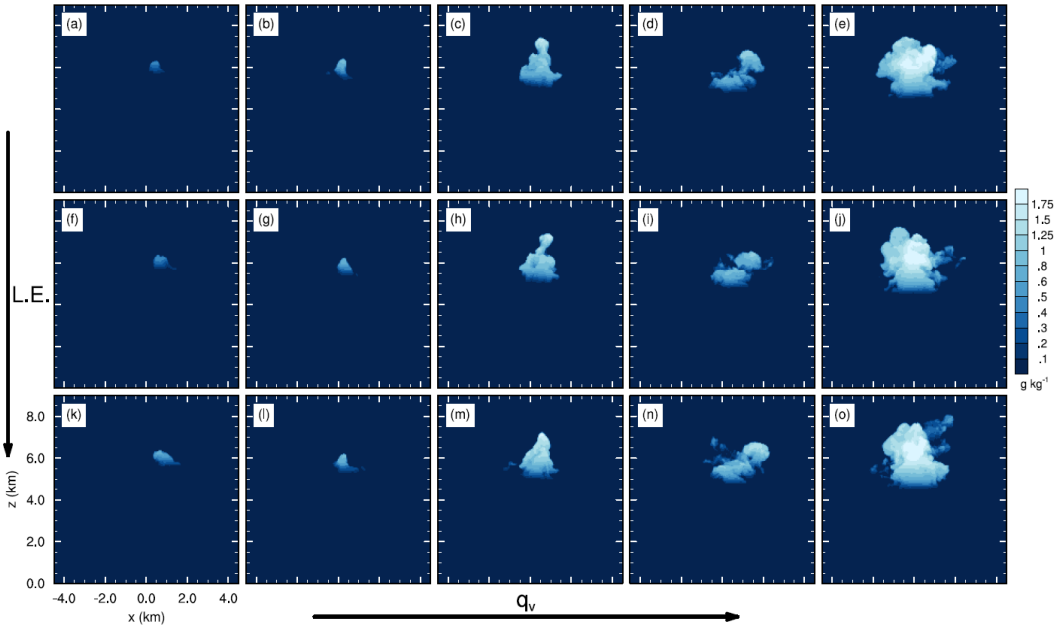

Figure 8. Vertical cross-sections of the maximum instantaneous liquid water mixing ratio in the y−direction, g kg^{-1}, at 22 minutes after the fires have reached full intensity. Panels show all fifteen combinations of fire latent heat flux, LE = (0, 2.1, 11.4) kW m^{-2}, arranged vertically and mixed-layer water vapour mixing ratio, q_{vML} = (2.0, 2.5, 3.0, 3.5, 4.0) g kg^{-1}, arranged horizontally. Fire latent heat flux increases from the bottom row of panels to the top row of panels and boundary-layer water vapour mixing ratio increases from the left-hand column of panels to the right-hand column of panels, as indicated by the arrows. All simulations are performed with a fire intensity Q = 30 kW m^{-2}.

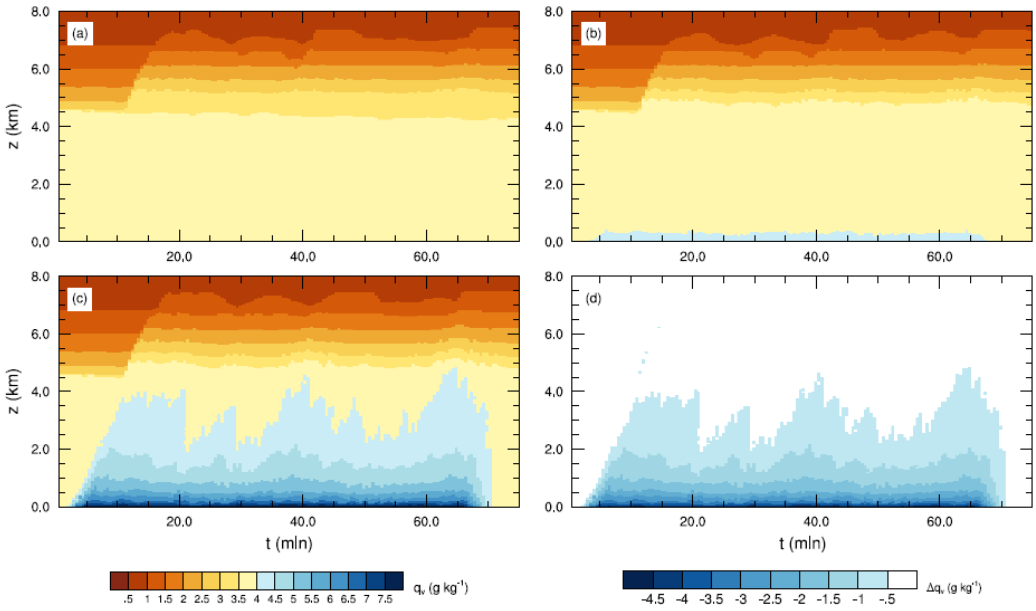

Figure 9. Time-height diagrams of the maximum instantaneous water vapour mixing ratio, g kg^{-1}, for simulations with fire latent heat fluxes, LE, of (a) 0.0 kW m^{-2}, (b) 2.1 kW m^{-2} and (c) 11.4 kW m^{-2}. Panel (d) shows the difference between (a) and (c). All simulations shown are for the Q = 30 kW m^{-2} fire intensity and q_{vML} = 3.5 g kg^{-1} mixed-layer water vapour mixing ratio case.

DISCUSSION AND CONCLUSION

Large-eddy simulations of buoyant wildfire plumes have been performed in background atmospheric conditions representative of high fire-danger days. The potential for the formation of pyro-convective cloud has been investigated by varying the environmental moisture and the fire intensity. Moister background atmospheres produce larger, more intense pyro-convective clouds and if the background atmosphere is moist enough, intense fires can produce pyro-convection even in the absence of any moisture from the combustion. Increasing the environmental moisture reduced the cloud-base height, whereas increasing the fire intensity had no discernible effect on cloud-base height.

The relative importance of environmental and fire-derived moisture has been assessed by repeating a set of fixed-intensity runs twice, with latent heat fluxes representative of dry and moist fuels respectively. Pyrogenous moisture was found to only have a small effect on pyrocumulus formation. This is because even for high rates of moisture release, this moisture becomes diluted as it is transported by the plume to the top of the boundary layer.

The resurgence of the plume updraft due to the latent heat released within a pyro-convective cloud has the potential to increase the height to which firebrands are lofted, particularly as the pyrocumulus updrafts are in excess of 10 m s^{-1}, considerably greater than the fall velocity of typical firebrands of 4–6 m s^{-1} (e.g. Ellis, 2010). Lofting the firebrands higher into the atmosphere has the potential to increase the distance they travel before landing, although detailed calculations similar to those described in the previous chapter (see also Thurston et al. 2017) would need to be performed to accurately assess the potential impact of pyro-convection on spotting distance.

Although we are currently unable to forecast the precise location and timing of an individual pyro-convective updraft or downburst, by performing studies such as this we are able to learn about the conditions under which they form, their dynamics and potential impact on fire behaviour.

PRACTICAL IMPLICATIONS

The ingredients for cloud formation are well known – moist air, and a cooling mechanism, which is usually ascent. In the case of pyrocumulus, there are two possible moisture sources, the atmosphere and the fire, and their relative role has been controversial. The moisture from the fire is difficult to characterize, for it depends on the total heat output from the fire, and the fuel characteristics. Hence, finding that forecasts are insensitive to a poorly-known parameter is good news, for it means that the forecast can probably make do with quite rough estimates of fire moisture output. Further good news is that the atmospheric contribution to moisture, particularly on likely pyroCu days, can be reasonably well estimated from surface observations near the fire.

In future, we plan to develop a pyrocumulus forecasting tool. This knowledge will be a crucial underpinning of that tool.

THERMODYNAMIC CONSTRAINTS ON PYROCUMULUS FORMATION

This chapter is based on a draft manuscript, *Tory, K.J., W. Thurston and J.D. Kepert, 2017: Thermodynamics of pyrocumulus: a conceptual study.*

SUMMARY

In favourable atmospheric conditions, large hot fires can produce pyrocumulonimbus (pyroCb) cloud in the form of deep convective columns resembling conventional thunderstorms, which may be accompanied by strong inflow, dangerous downbursts and lightning strikes. These in turn may enhance fire spread rates and fire intensity, cause sudden changes in fire spread direction, and the lightning may ignite additional fires. Dangerous pyroCb conditions are not well understood and are very difficult to forecast.

Here, a conceptual study of the thermodynamics of fire plumes is presented to better understand the influence of a range of factors on plume condensation. Recognising that plume gases are undilute at the fire source and approach 100% dilution at the plume top (neutral buoyancy), we consider how the plume condensation height changes for this full range of dilution and for a given set of factors that include: environmental temperature and humidity, fire temperature, and fire moisture to heat ratios. The condensation heights are calculated and plotted as saturation point (SP) curves on thermodynamic diagrams for a broad range of each factor. The distribution of SP curves on thermodynamic diagrams provides useful insight into pyroCb behaviour. Adding plume temperature traces from Large-Eddy Model simulations to the thermodynamic diagrams provides additional insight into plume buoyancy, how it varies with height, and the potential for dangerous pyroCb development.

INTRODUCTION

Pyrocumulus (pyroCu) clouds are produced by intense heating of air from fire or volcanic activity that leads to ascent and subsequent condensation when the rising air becomes saturated due to cooling from adiabatic expansion. The process is similar to conventional convective cloud formation, when a lifting mechanism (e.g., orographic lifting, intersection of two air masses) raises air above the level at which cloud forms (the lifting condensation level). Additional lifting and condensational heating may raise the air to the level of free convection, above which it is positively buoyant. Turbulent entrainment of cooler and drier air from outside the rising airmass dilutes the cloud buoyancy, which can limit the size and growth of the cloud (e.g., fair weather cumulus). Larger and more intense lifted regions can accelerate to the tropopause (e.g., cumulonimbus thunderstorms). The main difference between conventional cumulus and cumulonimbus and fire-sourced pyroCu and pyroCb (hereafter referred collectively as pyroCu/Cb) clouds is that the initial lifting in the latter cloud types is provided by the buoyancy from the heat and perhaps moisture released by the fire. In large fires with an intense convection column the cloud

may resemble towering cumulonimbus with updrafts that penetrate into the stratosphere. We refer to these plumes as pyroCb. (See Tory et al 2015, 2016 for a review of pyroCu/Cb literature and forecast techniques respectively).

There is abundant anecdotal evidence to suggest that the presence of pyroCb activity can have a significant impact on fire behaviour, including: (i) the amplification of burn- and spread-rates (Fromm et al. 2006, Trentmann et al. 2006, Rosenfeld et al. 2007, Fromm et al. 2012), (ii) enhanced spotting due to larger, taller and more intense plumes (e.g., Koo et al. 2010), and (iii) ignition of new fires by pyroCb lightning strikes due to pyroCb conditions favouring hotter and longer-lived lightning strikes (e.g., Rudlosky and Fuelberg 2011, Peace et al. 2017).

Given the potential threat posed by pyroCb there is great interest in being able to predict its development. Unfortunately, pyroCb are very difficult to forecast. Current forecast techniques draw on similarities between pyroCb and conventional thunderstorms, and the recognition that conditions that favour thunderstorm development will also favour pyroCb development. Ideal pyroCb conditions are thus similar to ideal thunderstorm conditions but with a dry rather than moist lower troposphere. These conditions appear on a thermodynamic diagram as the classic inverted-V profile, in which a dry adiabatic temperature profile of constant potential temperature (θ_{env}) forms the right side of the inverted-V, while the constant specific humidity (q_{env}) moisture profile makes up the left side.

In this paper we construct an idealized theoretical plume model in an inverted-V environment to aid our understanding of how the environment and fire properties influence pyroCu/Cb formation.

METHODS: PLUME MODEL

The fire plume is a mixture of hot combustion gases and entrained air from the immediate environment. For simplicity, it is assumed that the plumes are well-mixed and develop in a well-mixed atmospheric boundary layer of constant potential temperature (θ) and constant specific humidity (q), and that the plume condensation level (CL, which is the saturation point on a thermodynamic diagram) occurs within this well-mixed layer. While this assumption is likely to be unrealistic for deeper CLs, it has no impact on the conclusions. For simplicity the thermodynamics of the plume above the CL are not considered. However, useful information on plume thermodynamics can be determined from the plume θ and q at the CL, and diagnostic quantities derived from these variables.

The plume θ and q are expressed as functions of the environment θ and q and the fire θ and q, and the plume dilution fraction α,

$$\theta_{pl} = \alpha\theta_{env} + (1-\alpha)\theta_{fire} \quad (1)$$

$$q_{pl} = \alpha q_{env} + (1-\alpha)q_{fire}. \quad (2)$$

θ_{env} and q_{env} are specified for each scenario, and α is varied from 0 to 1, representing a range of plume dilution rates from pure combustion gases to pure environmental air (i.e., infinitesimal quantities of combustion gases). These

parameters and other variables introduced below are listed and described in Table 1.

Table 1: Plume model variables and constants

θ	Potential temperature (units K)
θ_{env}	Constant environment potential temperature (up to the condensation level)
θ_{fire}	Potential temperature of the fire (flames)
θ_{pl}	Plume potential temperature
$\Delta\theta_f$	Plume potential temperature contribution from combustion
q	Specific humidity (units $kg\ kg^{-1}$, mass of water vapour to total mass of air)
q_{env}	Constant environment specific humidity (up to the condensation level)
q_{fire}	Fire specific humidity (includes moisture from the air consumed in combustion)
q_{pl}	Plume specific humidity
Δq_f	Plume moisture contribution from combustion (evaporation of fuel moisture and moisture as a product of combustion)
α	Plume dilution factor. Ranges from 1 (100% dilute = environment value) to 0 (pure combustion gas)
β	Plume buoyancy factor. Ranges from 0 (plume 100% dilute) to $\gamma - 1$. (Useful range $0 \rightarrow \sim 10^{-1}$.)
γ	Fire heat multiplication factor to express θ_{fire} as a multiple of θ_{env}.
φ	Fire moisture to heat ratio (units $kg\ kg^{-1}\ K^{-1}$).

The potential temperature of combustion, θ_{fire}, can be expressed as a multiplier (γ) of the environment potential temperature, $\theta_{fire} = \gamma\theta_{env}$. Assuming θ_{env}~$300\ K$ γ ranges from $2 \rightarrow 5$ representing flame temperature estimates from forest fires of 600 K (flame tips) to 1500 K (flame base). The heat produced by the fire is, $\Delta\theta_f = (\gamma - 1)\theta_{env}$. The fire moisture to heat ratio, φ, is specified, which means fire moisture, $\Delta q_f = \varphi\Delta\theta_f$. Taking into account a 6 to 1 air to fuel ratio in combustion, the combustion gas includes an additional moisture contribution from the environment, $q_{fire} = \Delta q_f + 0.86 q_{env}$.

An iterative process is used to calculate the CL based on estimates of the CL pressure (P_{CL}). The CL temperature is calculated from θ_{pl} and P_{CL}, which are used to calculate the saturation vapour pressure at P_{CL}. If this saturation vapour pressure is less than (greater than) the actual vapour pressure the plume must be saturated (unsaturated) at P_{CL} and the process is repeated at a lower (higher) level until the plume CL is approached to the nearest 1 hPa.

A number of diagnostic equations have been developed to illustrate plume characteristics. Each can be expressed as a function of a buoyancy parameter,

$$\beta = (\theta_{pl} - \theta_{env})/\theta_{env} = (1-\alpha)(\gamma - 1), \qquad 3.$$

which reduces the experimental parameter space by replacing α and γ with β.

RESULTS

Two well-mixed boundary layer profiles are considered, one warm (Fig. 1a) and the other cold (Fig. 1b,). The first has $\theta_{env} = 303\,K = 30\,C$, $q_{env} = 5 \times 10^{-3} kg\ kg^{-1}$, 19% relative humidity, and an elevated lifting condensation level (LCL) about 3 km above the surface. The second has $\theta_{env} = 271\,K = -2\,C$, $q_{env} = 2 \times 10^{-3} kg\ kg^{-1}$, 61% relative humidity, and a relatively low LCL. This is representative of the Flatanger fire in Norway, January 2014, which destroyed 140 houses. The LCL is located at the apex of the θ_{env} and q_{env} curves. For clarity we refer to this LCL as the environment LCL (ELCL) to distinguish it from any in-plume LCLs.

Saturation point curves

Figure 10 includes SP curves for the hottest fire ($\gamma = 5$) in the warm environment (Figure 10a) and the coolest fire ($\gamma = 2$) in the cold environment (Figure 10b), and each with the two values of fire moisture to heat ratios that represent Luderer et al.'s (2009) driest ($\varphi = 3 \times 10^{-5} kg\ kg^{-1} K^{-1}$, red) and wettest ($\varphi = 15 \times 10^{-5} kg\ kg^{-1} K^{-1}$, blue) realistic fires. Each SP curve represents the position of the plume condensation level corresponding to α varying from 1 (100% dilution, lower left) to 0 (pure combustion gas, upper right) for the specified environment conditions, fire moisture to heat ratio, and fire heat. For example, the dots on the SP curves represent the apex of plume temperature and moisture traces for a plume consisting of 95% environment air and 5% combustion gas.

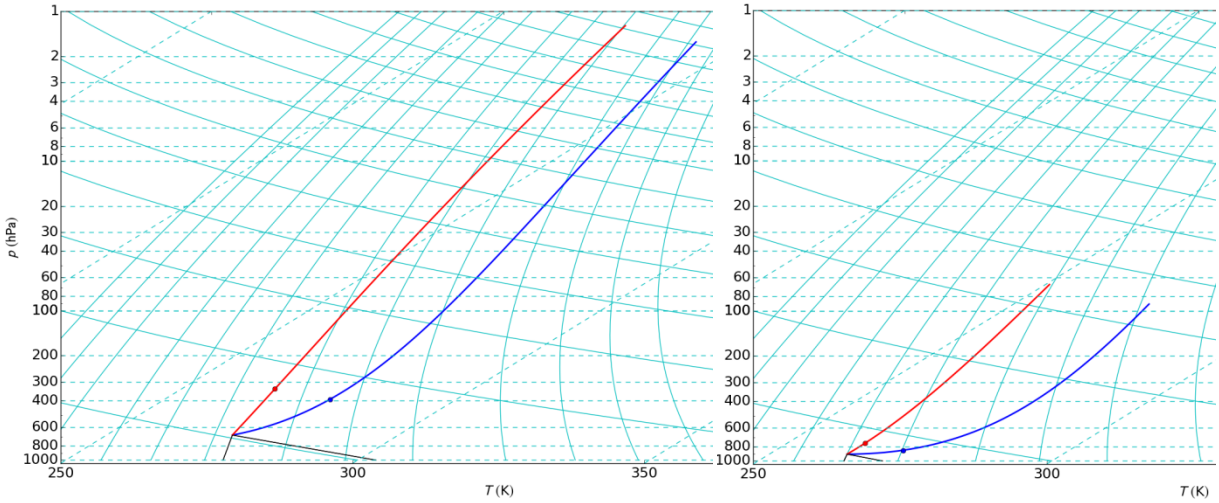

Figure 10: Saturation point curves for the dry (red) and moist (blue) fires, for the two cases (a) hot fire in a warm environment, and (b) cool fire in a cold environment, on a skewT-logp diagram. The 95% dilution points are indicated by dots. The environment LCL is located at the apex of the grey lines of constant θ_{env} and q_{env}. The pale blue lines are lines of constant pressure (dashed, horizontal), temperature (dashed, diagonal), potential temperature (solid, shallow gradient) and specific humidity (solid, steep gradient).

Of the parameter space investigated, the two most extreme cases are included in Fig. 1: hottest and driest fire in the warm environment (red curve in Figure 10a), and coolest and moistest fire in the cold environment (blue curve in Figure 10b).

100% dilution coincides with the ELCL, and zero dilution (at the upper right end of the coloured curves) shows exceptionally high CLs. These are ~1.5 hPa (> 40 km, Fig. 1a) and ~90 hPa (> 20 km, Fig. 1b).

Figure 10 shows that for pyroCu/Cb to form in the lower troposphere (e.g., below 500 hPa) significant dilution is necessary (e.g., > 95 % dilution for the hot fire, Figure 10a). Furthermore, Large-Eddy Model simulations (LEM, Thurston et al. 2016 and the previous chapter) suggest typical dilution amounts in the condensing plume are likely to be closer to 99%. It follows that substantial amounts of dilution must occur in typical pyroCu/Cb plumes, which corrects a common misconception that relatively undiluted plumes are necessary for pyroCu/Cb to form.

From Eq. 3 it can be seen that a plume from a hot fire (γ) with moderate dilution (α) could have the same buoyancy (β) as a plume from cooler fire with less dilution. This overlapping parameter space produces overlapping SP curves (e.g., the $\gamma = 2$ fire SP curve is almost exactly overlaid by the $\alpha = 1 \rightarrow 0.75$ part of the $\gamma = 5$ fire, not shown). Hereafter, we discuss plume buoyancy represented by the parameter β instead of fire heat and plume dilution. We conclude from Fig. 1 that for pyroCu/Cb to form in the lower troposphere, $\beta \leq O(10^{-1})$. Typical condensation level values of β in the LEM simulations are one to two orders of magnitude smaller than this.

Because β is small at condensation, the origin and gradient of the SP curves provide useful information about the height at which a plume will condense, and thus the potential for pyroCu/Cb formation. The origin ($\beta = 0$) coincides with the ELCL, which provides a first order estimate of the plume condensation level. The difference between the actual plume condensation height and the ELCL is of second order importance (for small β) which can be estimated from the product of β and the SP curve gradient. Thus for a given β, steep SP curves (e.g., dry fires) correspond to greater condensation heights than flatter (e.g., moister fires) SP curves.

Fortunately, the most important factor for estimating plume condensation heights (the ELCL) does not require any information about the fire. The secondary factor is dependent on the environment plus the fire moisture to heat ratio (φ) and the plume buoyancy (β). To determine β at the plume condensation height, we expect detailed knowledge would be required of how plume buoyancy is affected by fire size, distribution and intensity, and how the atmosphere (e.g., wind and thermodynamic stability) affect the entrainment rate (plume dilution), and thus the distribution of β with height. One might also expect detailed knowledge of the fire and fuels would be required to determine φ. However, within the assumptions of the simple theoretical plume model (i.e., plume moisture and heat are diluted at the same rate), φ remains constant throughout the plume (and is independent of β), which means it can be estimated from a single plume measurement anywhere in the plume and at any time,

$$\varphi \cong \frac{q_{pl}-q_{env}}{\theta_{pl}-\theta_{env}}. \qquad 4.$$

In reality φ is likely to vary with time (and perhaps spatially), as the fire burns through a variety of fuels, but as long as the measurement is taken above the flaming zone (so that additional radiative heat losses are relatively small) the measured plume element should maintain a constant φ throughout its ascent through a well-mixed boundary layer (constant θ_{env} and q_{env}). Thus, in practice it should be possible to produce thermodynamic diagrams with the ELCL and SP curves plotted, similar to Figure 10, from observations at the fire ground, provided a representative sample of q_{pl} and θ_{pl} measurements can be made.

Plume temperature traces

The SP curves provide insight into the height at which a plume or plume element might condense for a given environment (θ_{env}, q_{env}), fire moisture to heat ratio (φ)and plume buoyancy (β), but they do not tell us anything about specific plumes. In Figure 11 temperature and moisture traces from two LEM plume simulations (taken from Thurston et al. 2016) have been plotted on thermodynamic diagrams with SP curves included. An extra SP curve has been added representing the fire moisture to heat ratio from one of Potter's (2005) fireCAPE thought experiments (green curve), which Luderer et al. (2009) argued was unrealistically moist.

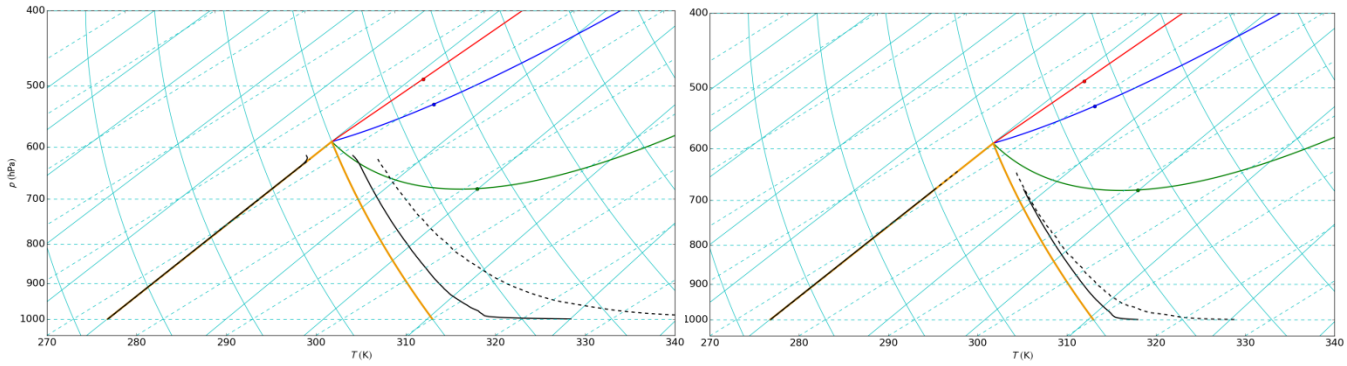

Figure 11. As in Fig. 1 but with mean (solid) and maximum (dashed) plume temperature and moisture traces in a hot and dry ($\theta_{env} = 310$ and $q_{env} = 4 \times 10^{-3}$), zero wind environment from LEM simulations with a constant circular surface heat flux (Q) of 250 m radius. Saturation point curves for the dry (red, $\varphi = 3 \times 10^{-5}$) moist (blue, $\varphi = 15 \times 10^{-5}$) fires and an extremely moist fire (green, $\varphi = 100 \times 10^{-5}$) are included. (a) hot fire ($Q = 30\ kWm^{-2}$) (b) cool fire ($Q = 5\ kWm^{-2}$).

As the LEM plume air ascends and approaches the ELCL it begins to entrain warm and dry environment air from above the boundary layer, which is a process that cannot be incorporated in our theoretical model. Thus, we discount the plume traces higher than about 620 hPa, and instead mentally extrapolate them to the SP curves. Additionally, in order to make a clear distinction between plume and environment air, only plume elements that are at least 1 K warmer than the environment were included in the plume-average temperature trace. In reality the plumes are expected to contain a mix of air parcels of temperature varying from the environment temperature (recently entrained parcels) up to the maximum temperature indicated by the dotted lines (least diluted air parcels).

For the hot fire (Figure 11a) the mix of plume element temperatures would be expected to have a range of condensation heights extending from the ELCL to where the extrapolated dashed line meets the SP curve corresponding to the fire's moisture to heat ratio. The corresponding buoyancies range from $\beta = 0 \rightarrow 0.14$, with the plume average, $\beta = 0.04$. This simulation produced deep pyroCb with rain and evaporatively cooled downdrafts. Whereas the plume dilution was generally too great for condensation to occur in the cool fire simulation (Fig. 2b) as it mostly lost buoyancy near 650 hPa before intersecting any of the SP curves. A few parcels of buoyant air did occasionally reach the condensation level, producing short-lived puffs of shallow cloud.

DISCUSSION: WHAT CAN WE LEARN FROM THESE DIAGRAMS?

There is a surprising amount of information about conditions that support pyroCu/Cb development and plume behavior that can be gleaned from Figure 10 and Figure 11.

- The positive gradients of the SP curves corresponding to the realistic range of fire moisture to heat ratios (red and blue) demonstrate that buoyant plume elements condense at levels higher than the ELCL (consistent with Luderer et al. 2009).
- An exception is for very moist fires (e.g., green SP curves in Figure 11) and/or very dry environments (e.g., Figure 10b) where the SP curve may have a negative gradient, in which case some buoyant elements might condense at levels lower than the ELCL (e.g., the Potter 2005 fireCAPE thought experiment). This is more likely to occur in cold and dry (small q) environments.
- Buoyant elements from moister fires will condense at lower levels than for drier fires.
- There is a broad range of temperatures and hence buoyancy within plumes, that decrease with height (due to dilution from entrainment, Figure 11).
- Plumes with non-trivial buoyancy near their condensation level (e.g., Figure 11a), contain plume elements with a range of buoyancy from zero to a maximum value corresponding to the least dilute plume element, with a corresponding range of condensation heights. These condensation heights are determined by the intersection of the plume element temperature trace and the relevant SP curve.
- Plumes that produce pyroCb (e.g., Figure 11a) have non-trivial buoyancy near the condensation level, suggesting the fireCAPE concept may be useful for pyroCb forecasting.
- The same LEM heat sources in environments with lower ELCLs (e.g., that might occur with the passage of a cold front or sea breeze) might produce very much more energetic pyroCb. At 900 hPa the hot fire mean and maximum plume values of β are about three times greater than at 600 hPa, and the cool fire mean and maximum plume values of β at 900 hPa are very similar to the hot fire at 600 hPa.

More insight will be described in a journal article (in preparation), based on a mathematical exploration of the model parameters. This paper describes among other things how the environment affects the SP curves, what values of plume buoyancy are important for pyroCu/Cb activity, and the sensitivity of fireCAPE to plume buoyancy.

CONCLUSIONS

PyroCb can produce dangerous fire behaviour, through changes in fire rate of spread and direction, increased spotting, and additional ignitions from lightning strikes. Unfortunately, pyroCb are difficult to predict and not well understood.

In this paper we have introduced a simple theoretical model that provides useful insight into the conditions that favour pyroCu/Cb formation, the thermodynamic composition of fire plumes, and the relative sensitivity of environment conditions to fire properties that determine pyroCu/Cb formation and behaviour. Some of the more general results are summarized here:

- A substantial amount of dilution is required for pyroCu/Cb cloud elements to condense. However, too much dilution and the plume may lose buoyancy before ascending high enough for condensation to occur.
- The environment lifting condensation level (ELCL) provides a good first order estimate of the plume condensation height.
- Typical forest fires that produce pyroCu/Cb will have buoyant plume elements that condense at elevations higher than the ELCL, because the additional heat provided by the fire contributes to raising the condensation level more than the additional moisture contributes to lowering the condensation level.
- PyroCu/Cb formation and behaviour is relatively insensitive to fire heat and moisture, but could be very sensitive to environment changes, such as might be experienced with the arrival of a cold front or sea-breeze that lowers substantially the ELCL due to the arrival of cooler and moister air.

PRACTICAL IMPLICATIONS

This work confirms the potentially controversial finding of the previous chapter, of the small role that fire moisture plays in pyrocumulus formation for typical forest fire conditions. It thus supports the simplifying assumptions that we will use in our development of a pyrocumulus forecasting tool. The elegant simplicity of the modelling in this component will also help inform our development of that tool, and ensure that it has a rigorous scientific foundation.

HIGH-RESOLUTION ENSEMBLE PREDICTION OF AN EAST COAST LOW

This chapter is adapted from a draft manuscript, *Zovko-Rajak, D., K.J. Tory, R.J.B. Fawcett and J.D. Kepert, 2017: High-resolution ensemble prediction of the east coast low of April 2015.*

SUMMARY

During autumn and winter months the eastern coast of Australia is periodically affected by rapidly developing and intense extratropical low-pressure systems that are known as East Coast Lows (ECLs). ECLs bring damaging winds and heavy rainfall with flooding that can last for several days. Due to their rapid development, many forecasting issues arise; such as: predicting the location of the system along the coast, and the intensity and location of maximum winds and rainfall. The use of ensembles can help overcome these forecast challenges and provide insight into how these systems form.

The event that is studied here occurred during 20-23 April 2015, with the worst impact on 21 April. This event was simulated using a 24-member ensemble of ACCESS nested models. Simulations show that forecast rainfall (averaged over the 24 ensemble members) is in good agreement with observed rainfall and the ensemble identifies Dungog as the area of substantial risk of extreme rainfall. A subset of ensemble members shows very little rain in the Dungog area; instead it is located further south or east, indicating that a large part of the coast is at risk of significant rain. Ensemble comparison shows that the strongest surface winds and highest rainfall occur to the south of the main low, together with the strengthening of the north-westerly jet and the upper cut-off low west of the surface low. However, localised differences between members produce large differences in location and strength of extreme winds and highest rainfall. A better understanding of the dynamics and predictability of ECLs has important implications not only for forecasters, but also for emergency services preplanning and preparedness.

INTRODUCTION

The focus of this study is a low-pressure system that affected the eastern coast of Australia between 20 and 23 April 2015 (known locally as an east coast low), with the worst impact on 21 April. This was a devastating event for the Dungog and Maitland area (map in Figure 12), with at least 4 deaths reported and widespread damage. Dozens of houses lost their roofs, over 200 000 houses were without power, and 57 schools closed. By studying this event, better understanding of the dynamics and processes that lead to the rapid intensification of these systems can be gained. Additionally, the predictability of the event can be studied as there are many issues associated with the forecasting of east coast lows (e.g., intensity and location of maximum winds and rainfall, location along the coast).

East Coast Lows (hereafter ECLs) are rapidly developing and intense extratropical low-pressure systems that periodically affect eastern coast of Australia during autumn and winter months. They form preferentially at night (Holland et al.1987) and although they are most common during winter months, they can occur at any time of the year (Speer et al. 2009). ECLs bring damaging winds and heavy rainfall with flooding that can last for several days. They are responsible for about 50-80 % of extreme rainfall events within the eastern seaboard of Australia (Dowdy et al. 2013), where a large majority of the Australian population live, and are also very important for catchment inflows and water security east of the Great Dividing Range (Pepler and Rakich 2010). Recently, the "Pasha Bulker" storm of June 2007 caused the grounding of the Pasha Bulker carrier ship as well as major socioeconomic losses, making it one of the most significant meteorological events for Australia (e.g., Mills et al. 2010, Verdon-Kidd et al. 2016).

Holland et al.'s (1987) study showed that ECLs are mesoscale phenomena that form on the coast within a distinctive synoptic system that consists of a trough (or "dip") in the easterly wind regime over eastern Australia. This pattern is locally known as an "easterly dip" and its development is similar to the one associated with a "bomb" that develops off the eastern U.S. seaboard (e.g., Sanders 1986). ECL's formation is also associated with strong oceanic temperature gradients. Based on whether ECLs form east of, on, or west of the dip axis, Holland et al. classified them into three types.

Type 1 ECLs form when a developing easterly dip is present over the continent; they are small in size and form preferentially over the ocean. In contrast, development of ECLs of type 2 is rapid and occurs within an easterly dip on the coast. The majority of ECLs that were studied by (Holland et al. 1987) were of this type. Type 3 systems form on the western side of an easterly dip in the Tasman Sea; they are small (100 km across), develop rapidly and often disperse within 24 hours of their formation.

There are many forecasting challenges associated with ECLs due to their rapid development. These include predicting the location of the system along the coast, the intensity and location of maximum winds and rainfall, their relationship to the centre of the developing low as well as the likelihood of the associated storm surges (Leslie and Speer 1998, Mills et al. 2010). Another challenge associated with ECLs is their representation in numerical weather prediction (NWP) models, especially since the area of most intense winds and heavy rainfall is usually very narrow. For example, in the "Pasha Bulker" storm the strongest wind and rainfall bands were on the order of 100 km wide.

Large scale atmospheric processes associated with explosive cyclogenesis are reasonably well represented by today's NWP models and by coarse-resolution global climate models (Mills et al. 2010, Dowdy et al. 2013). However, smaller scale structures and processes that occur within the overall system and often contribute significantly to extreme weather are poorly represented by these models and require higher horizontal resolution. Fine details are also less predictable and one way of overcoming these challenges is by using an ensemble of high-resolution simulations. Ensemble forecasts provide opportunity to study predictability of ECLs by analysing differences between the simulations,

as well as a more thorough analysis of processes that lead to rapid intensification of these systems.

Accurate forecasts of severe weather events such as ECLs are important not only for meteorologists but also for emergency services and communities as they enable better risk management and preparedness for the event. Therefore, the main aim of this study is to, by analysing a high-resolution ensemble of 24 simulations, elucidate processes associated with the development of the April 2015 east coast low and learn about the predictability of the event.

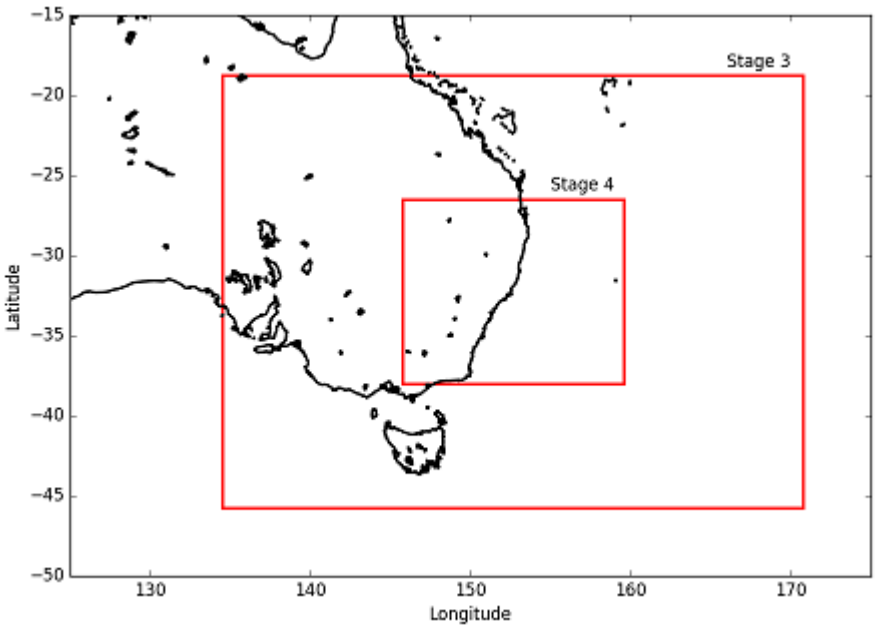

Figure 12. Outline of model domains, with larger domain having horizontal resolution of 4 km (stage 3) and smaller domain with horizontal resolution of 1.3 km (stage 4).

SET UP AND DESIGN OF ENSEMBLE SIMULATIONS

In this study, high-resolution ensemble forecasts are used to analyse the development and dynamics of the east coast low of April 2015. For all simulations, version 8.5 of the UK Met Office Unified Model (UM), the atmospheric component of Australian Community Climate and Earth-System Simulator (ACCESS) is used (Puri et al. 2013). The ensemble consists of 24 simulations (1 control + 23 perturbed) that are initialized from the 24 members of the Bureau of Meteorology prototype global ensemble prediction system (ACCESS-GE), which is based on the Met Office ensemble prediction system known as MOGREPS (Bowler et al. 2008). All simulations were initialized at 0000 UTC on 20 April 2015 (+ 10 hours for local time) and ran for 48 hours.

The model consists of a global model run that is nested down to 4 km (hereafter stage 3) and 1.3 km (hereafter stage 4) regional runs (Figure 12 shows the outline of stage 3 and stage 4 domains). The smallest grid spacing (1.3 km) sufficed to capture the dynamics of the event because of balance between the domain size and resolution. Each domain has 70 vertical levels and the

model top for nested domains is 40 km. Results from the 1.3 km domain are shown in this report.

RESULTS FROM ENSEMBLE SIMULATIONS

Overview of the mean forecast and comparison with observed rainfall

In this section an overview of the ensemble mean forecast is presented. Figure 13 shows 1200 UTC 20 April 2015 near-surface (1 km) and upper-level (10 km) flow comparison for the ensemble mean forecast. Strong south-easterly near-surface winds are seen to the south of the main low in Figure 13a, and at upper levels there is a clockwise tilted (towards the northeast) trough that moves toward the coast, with a strong north-westerly jet to the northeast of the upper-level trough (Figure 13b). This pattern seems to be common for most ECLs (Mills et al. 2010). However, there is large variability in the location and strength of maximum surface winds between the members, which is associated with differences in surface and upper-level flow characteristics and these are discussed in more detail in subsequent sections (note that this mean forecast has somewhat smooth features due to the ensemble averaging).

A comparison between the observed 48-hr rainfall total (up to 09 am 22 April 2015) and the forecast 48-hr rainfall total, which is averaged over the 24 ensemble members, is shown in Figure 14. It is evident that the forecast rainfall is in good agreement with the observed rainfall, even though the rainfall in the Dungog area is not as heavy as observed. Some individual members (Figure 15) had higher values than the ensemble mean and closer to the observed peak. The probability-matched ensemble mean (PMEM) of 48-hr rainfall total (Figure 14c) retains these peaks and shows even better agreement with the observed maximum rainfall. Forecast probability of 48-hr total rainfall exceeding 100 mm (Figure 14d), defined as the proportion of the ensemble exceeding this threshold, shows that the ensemble identifies the Dungog area as being of substantial risk of extreme rainfall.

Figure 15 shows that there is a large spread in 48-hr total rainfall between ensemble members. Some members predicted very little rain in the affected area (white circle in Figure 15); rather rain was located more to the south (e.g., member 11) or east-north-east of Dungog (e.g., members 17 and 20). This indicates that a substantial part of the coast is at risk of significant rain, and emphasizes the importance of studying ensemble simulations in order to improve prediction of this event but also of other severe weather events.

To examine reasons for differences in the flow development and location of maximum winds and rainfall, ensemble members 11, 17 and 22 are compared and analysed in the next section. Ensemble member 11 is an example of a "dry" member; the majority of predicted rainfall was located to the south of the white circle in Figure 15. Ensemble member 22 is an example of a "wet" member; the highest predicted rainfall amounts (Figure 15) were located inside the white circle surrounding Dungog. In contrast to these, ensemble member 17 was different as it had 2 "centres" of highest rainfall; one to the south of Dungog and one to the north-east (Figure 15r). Analysis of surface and upper-level low development will show that this member differs largely from other

members in the location and rotation of the main system, as well as secondary vortices that develop along the shear line.

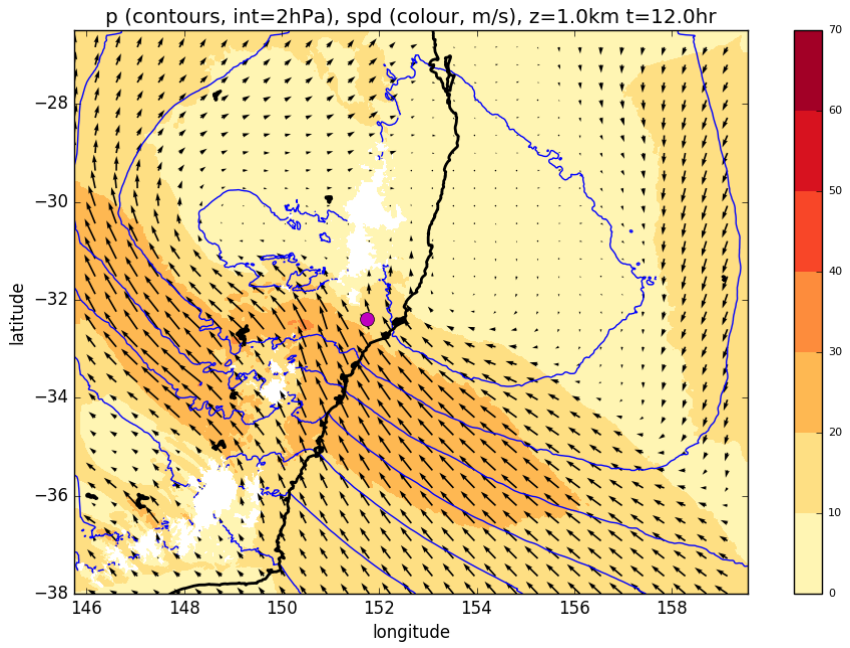

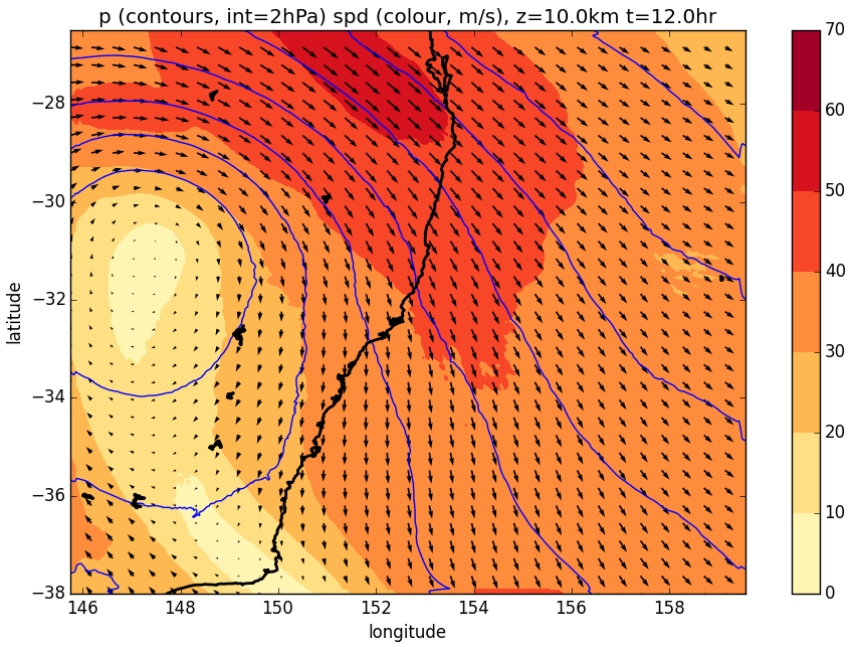

Figure 13: (top) Near-surface (1 km) and (bottom) upper-level (10 km) winds (m/s) and pressure (contours, hPa) for ensemble mean forecast at 1200 UTC 20 April 2015.

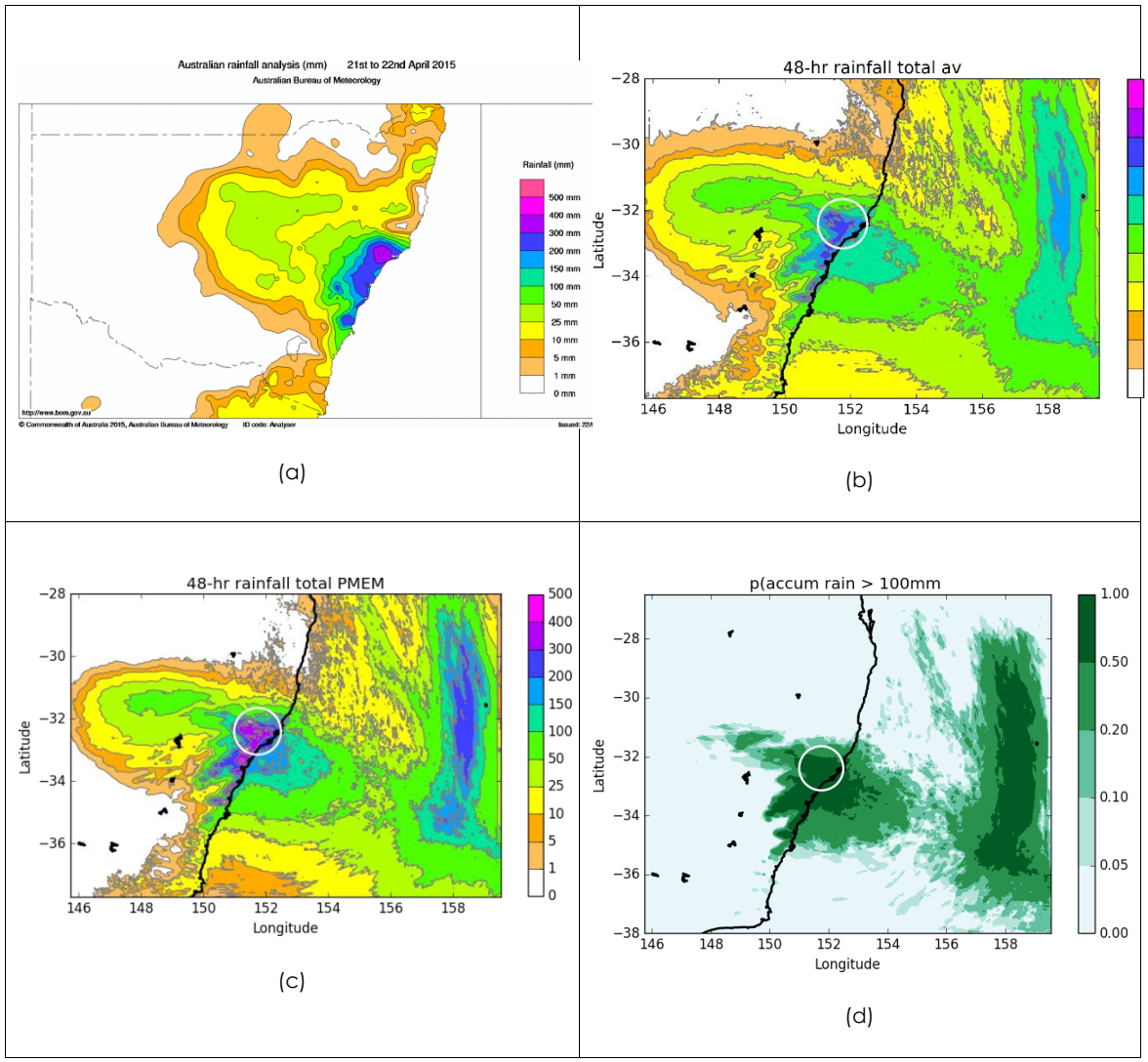

Figure 14: A comparison between (a) observed rainfall (up to 9 am 22 April 2015) and (b) forecast rainfall (averaged over the 24 ensemble members, for 20-22 April 2015). (c) Probability matched ensemble mean, and (d) rainfall probability exceeding 100 mm.

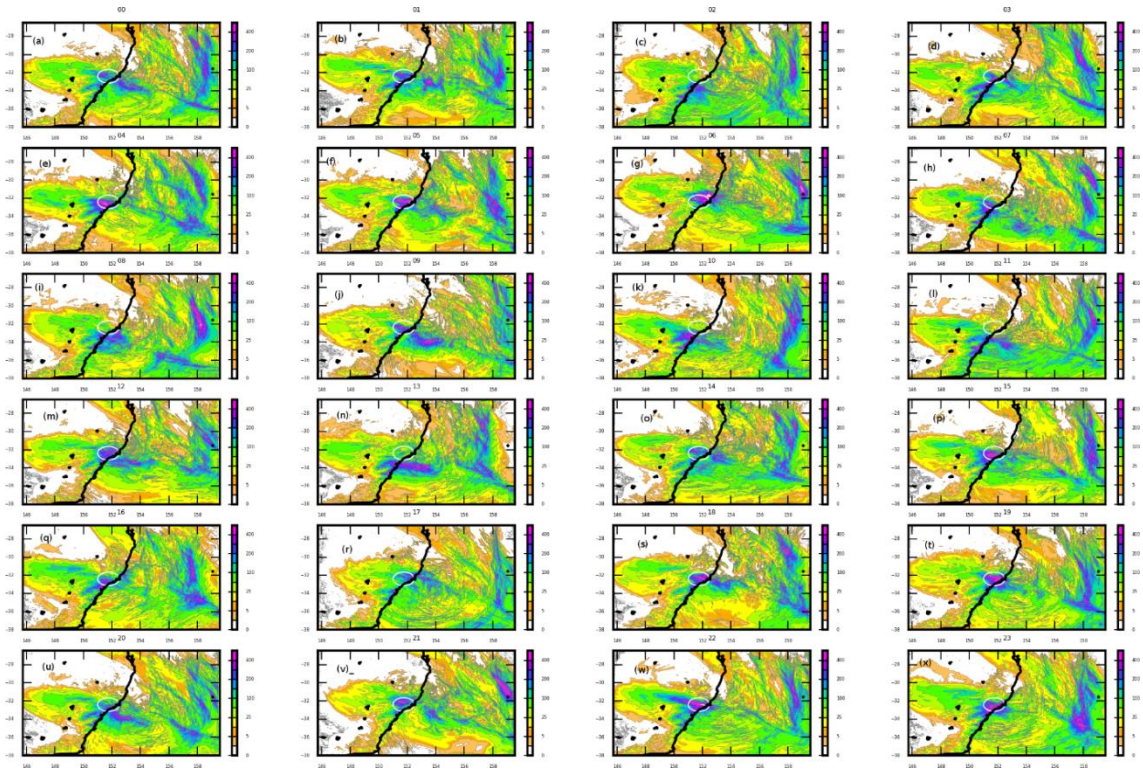

Figure 15. A postage stamp showing 48-hr total accumulated rainfall for all ensemble members.

Differences in surface- and upper-level flow development between the members

As mentioned previously, ECL development is characterized by the interaction of a pre-existing trough of low pressure and an upper-tropospheric cut-off low. Often, many small vortices form on the shear line at the southern edge of the main low, and these can bring the worst weather. Also, the strongest winds and heaviest rain usually occur to the south of the main low centre. A subsequent analysis investigates these features and their relationship in the April 2015 ECL in more detail. By studying the synoptic features as well as similarities and differences between ensemble members, a better understanding of the storm dynamics can be gained. Additionally, features that are more or less predictable can be identified in this way too.

Figure 16 and Figure 17 show near-surface (1 km) and upper-level (10 km) flow comparison for members 11, 17, and 22 at 1000 and 2000 UTC 20 April 2015, and at 0600 UTC 21 April 2015. All members in Figure 16 show strong south-easterly near-surface winds (> 20 m/s) to the south of the main low that are blowing across the isobars and toward lower pressure, with small low pressure centres along the shear line. This cross-isobar flow contributes to surface convergence which, as will be shown below, coincides with regions of highest rainfall. At the same time, the upper-level trough amplifies, cuts off and rotates clockwise, while moving eastwards towards the coast (Figure 17). The north-westerly jet on the northeast flank of the upper-level trough strengthens and splits into a cyclonic branch which curves to the south, and the anticyclonic branch which curves into the Tasman Sea (Mills et al. 2010). Although not evident in these figures due to the domain size, there is a strong ridge to the west and south of the upper-level low; this ridge extends all the way to the surface which contributes to the formation of a strong pressure gradient to the south of the low and subsequently to the strengthening of the low-level jet (LLJ).

Even though basic patterns of the evolution of the upper-level low and the strengthening of the surface low are similar among analysed ensemble members, there are localized differences which can produce large differences in location and strength of extreme wind and rain. It is evident from Figure 16 and Figure 17 that the south-easterly LLJ as well as the upper-level low have slightly different location and strength for the 3 members. These differences are also present amongst other ensemble members; however space does not permit us to show analyses for all ensemble members.

In member 11, the LLJ is located further south than in the other two members, with the rainfall maximum located also to the south rather than around Dungog (cf. Figure 15). The upper-level low is located to the west of the surface low. In member 22, the strong LLJ is directed towards Dungog and the upper-level low cuts off and is located to the west of the surface low. A secondary low forms offshore after 2000 UTC (Figure 16f), moves towards the coast, begins to counter rotate with the main low centre (Figure 16i) and aligns vertically towards the end of the simulation (not shown). Compared to members 11 and 17, member 22 has the highest rainfall accumulated around Dungog. Member 17 has very distinct vortices that develop on the shear line as evident from the pressure contours, and the strongest low developing offshore compared to the other two members (Figure 16b, e and h). Additionally, the LLJ has become southerly

and the upper-level low has moved further off-shore by 0600 UTC 21 April 2015 (Figure 16h and Figure 17h) compared to members 11 and 22.

A comparison of the low-level wind and hourly rainfall for the three members is shown in Figure 18. It is evident that the surface low is not symmetric, and that extreme winds are localized. Also, rain occurs in discrete regions within the low; along the low-level convergence lines to the south of the main low, and also on the eastern edge over the Tasman Sea. Strong near-surface temperature gradients are collocated with regions of extreme wind (not shown). From Figure 18 it is evident that for members 17 and 22 the rain band on the convergence line encompasses the Dungog area by 2000 UTC, however, in member 11 it is located further to the south.

In order to have a better understanding of the relationship between maximum winds and rainfall, mid-level winds and hourly rainfall are compared to a thermal advection rainfall diagnostic (Figure 18 and Figure 20). The diagnostic is based on the relationship between thermal advection and geostrophic winds turning with height (e.g. Holton 2004) which also applies for gradient winds that turn with height (Tory 2014). It has been used for decades by the Australian forecasting community in the prediction of subtropical and tropical heavy, and can be used successfully for most large scale and mesoscale systems, including ECLs. For both geostrophic and gradient wind formulations the relationship is the same, namely, anticyclonic (cyclonic) rotation with height is associated with warm (cold) air advection and isentropic ascent (descent). Here, the gradient wind formulation is used to calculate the thermal advection diagnostic (equation 15 in Tory 2014).

Comparison of mid-level winds with hourly rainfall in Figure 19 shows that areas of heavy rain coincide with winds that rotate anti-cyclonically with height, while the rain-free areas coincide with winds that rotate cyclonically with height. This agrees well with the thermal advection diagnostic shown in Figure 20, where positive warm air advection (WAA) or isentropic ascent (red in Figure 20) coincide with areas of heavy rain, while to the north negative WAA (blue in Figure 20) indicates cold air advection and rain-free areas. This comparison is valid for all three members analysed here, however as mentioned previously, they differ in location and strength of heavy rain and winds. This analysis also shows that the upper and lower-level circulations are not vertically aligned and that the tilt of the low is associated with ascent (corresponding to rain) and descent (no rain). Thus, localised differences in extreme wind and rain likely stem from different responses to upper-level and surface forcing and also to differences in tilting of the low core.

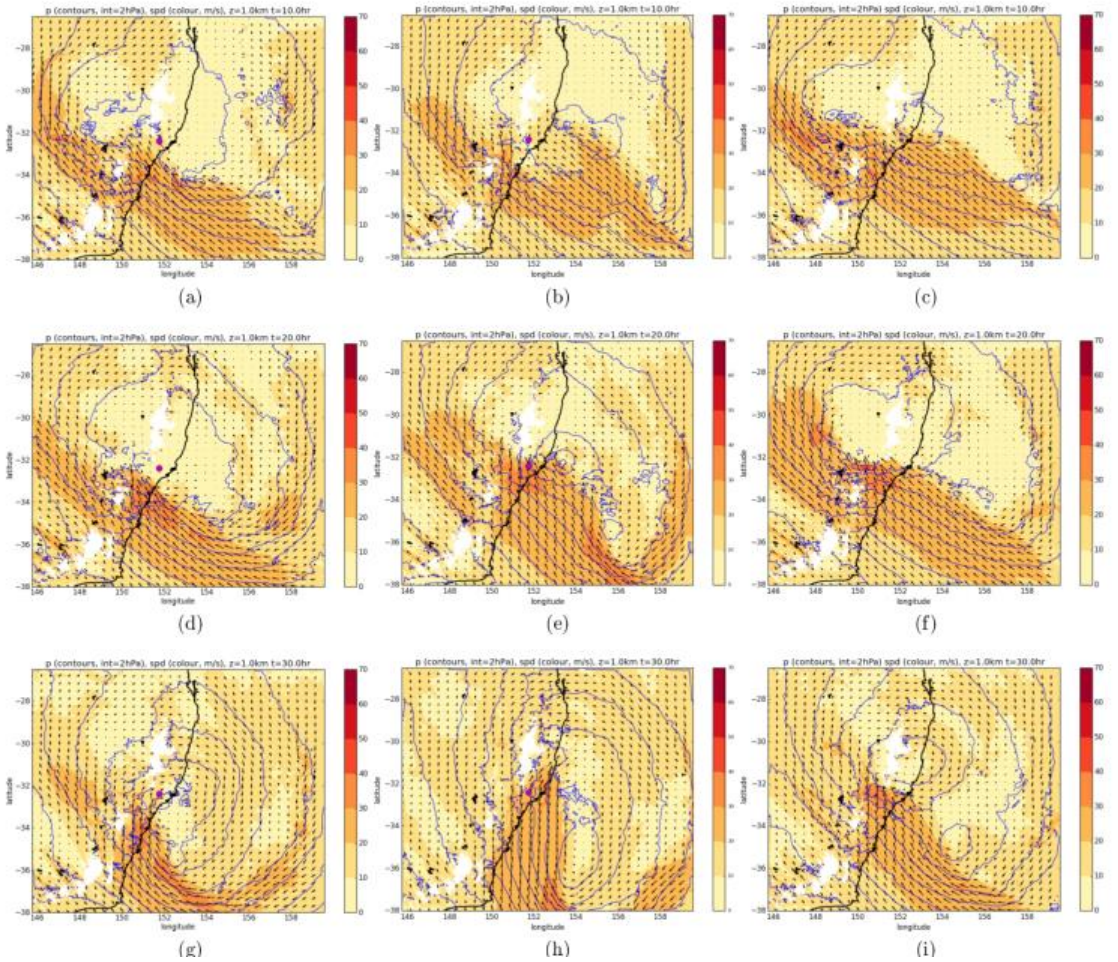

Figure 16: A sequence of 1 km winds (m/s) and pressure (contours, hPa) for (left) ensemble member 11, (middle) ensemble member 17 and (right) ensemble member 22 at (a,b,c) 1000 UTC 20 April 2015, (d,e,f) 2000 UTC 20 April 2015 and (g,h,i) 0600 UTC 21 April 2015.

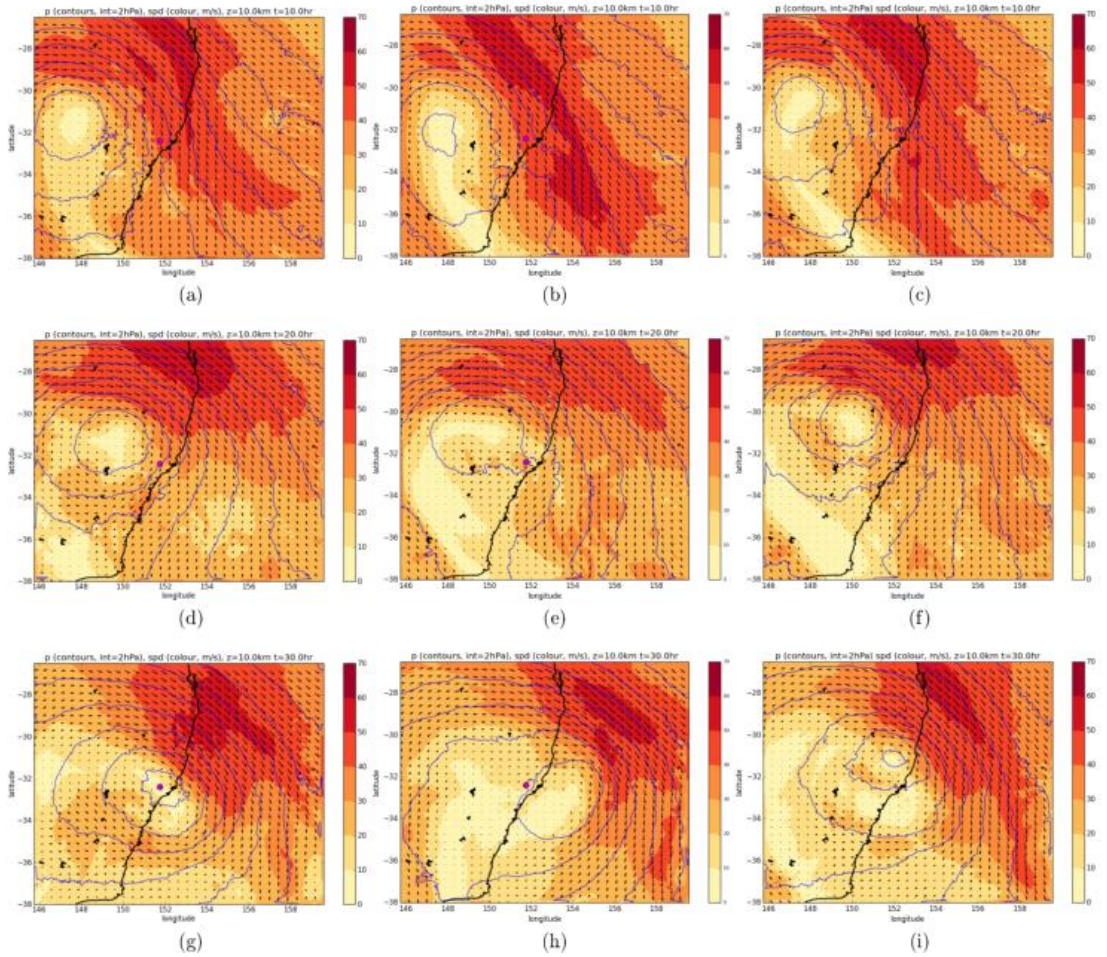

Figure 17: Same as Figure 16, except at 10 km.

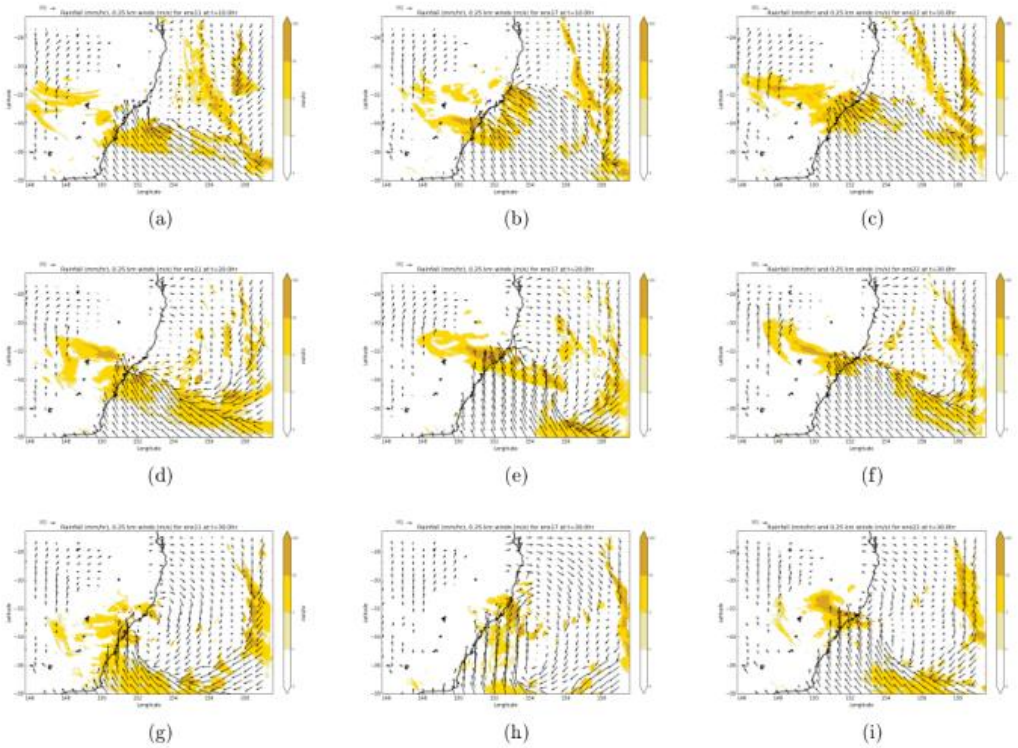

Figure 18. Same as Figure 16, except showing low-level wind (250-m wind vectors) and hourly rainfall (shading, mm).

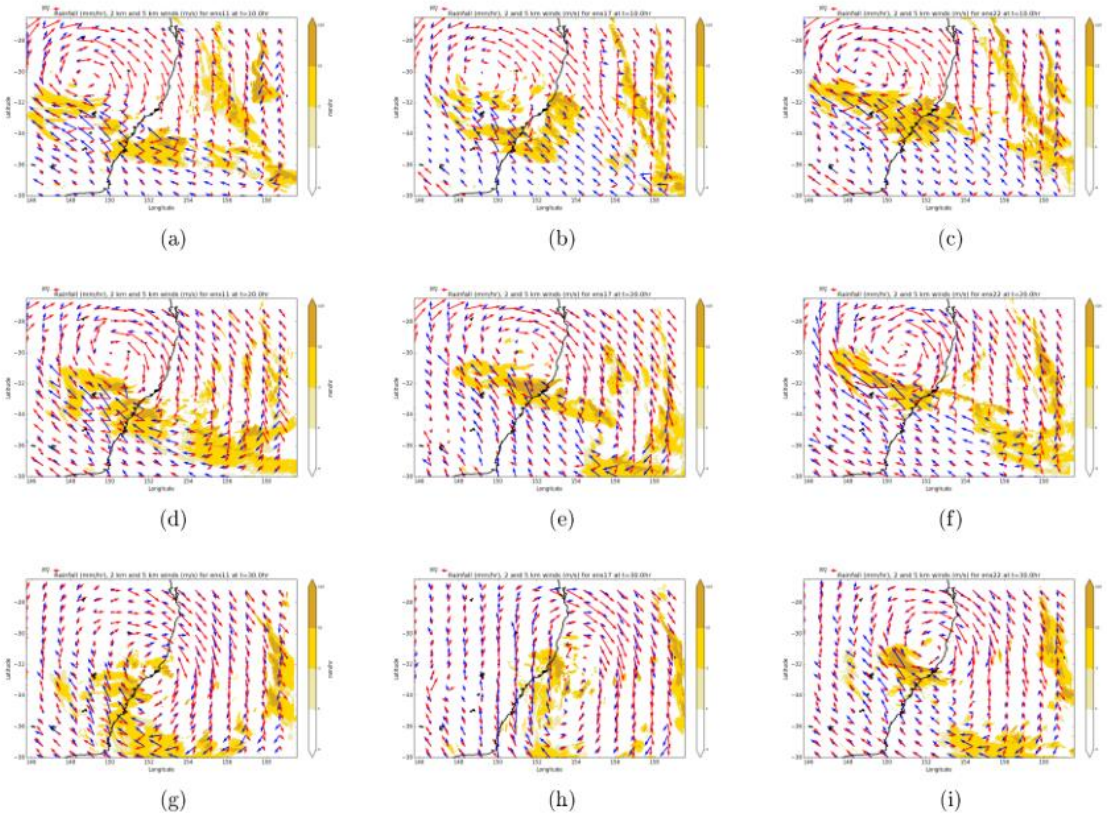

Figure 19. Same as Figure 16, except for 2 km (blue vectors) and 5 km (red vectors) winds, and hourly rainfall (shading, mm).

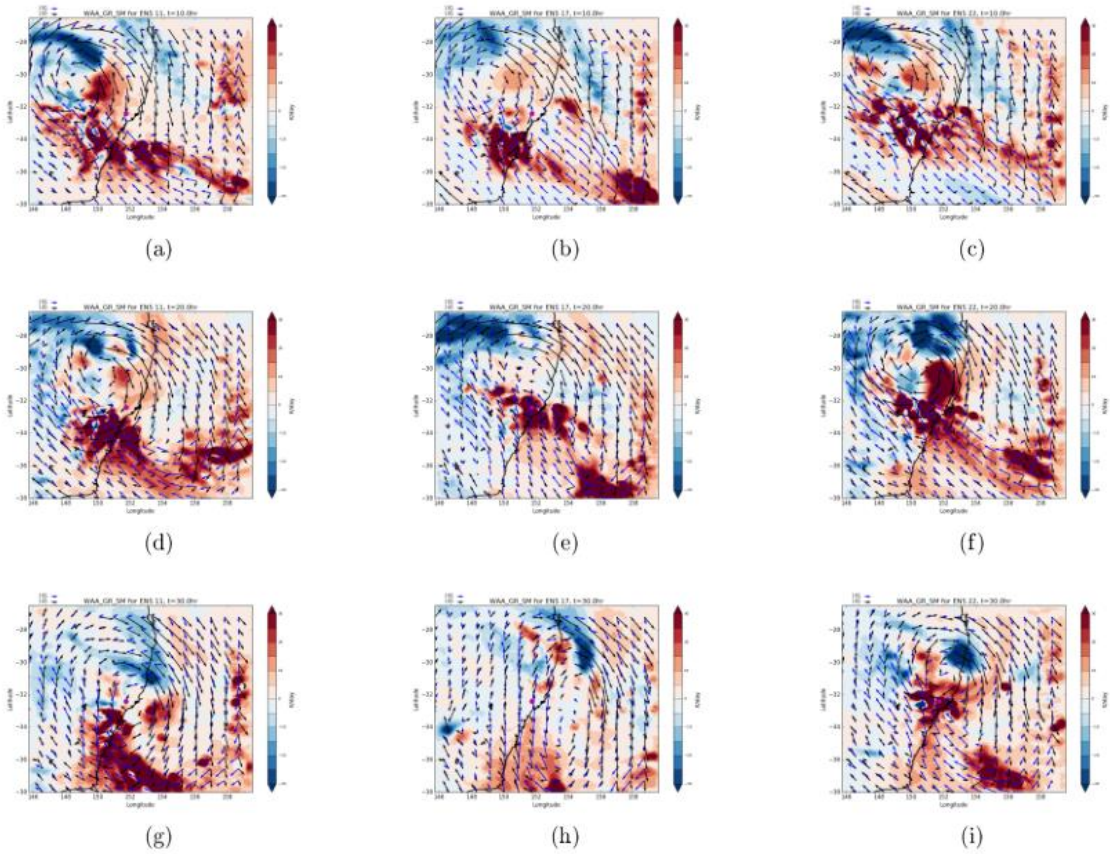

Figure 20. Same as Figure 16, except for thermal advection rainfall diagnostic (or WAA), with 1.5 km (blue vectors) and 5.5 km (black vectors) winds. Red indicates positive values, blue indicates negative values.

SUMMARY AND CONCLUSIONS

An analysis of the East Coast Low (ECL) that affected the eastern coast of Australia between 20 and 23 April 2015 is presented, to get a better understanding of the dynamics of the storm as well as its predictability. For this, an ensemble consisting of 24 high-resolution simulations using the ACCESS model was prepared.

A comparison between the observed and forecast rainfall of the event (averaged over the 24 ensemble members) showed that the forecast rainfall is in good agreement with the observed rainfall. Even though peak rainfall in the Dungog area of the mean forecast was not as high as observed, the forecast probability of rainfall exceeding 100 mm showed that the ensemble identified Dungog as the area of substantial risk of extreme rainfall. Ensemble analysis also showed a large variation in total rainfall, with some members having more rain located to the south or east of the Dungog area. This indicated that a substantial part of the coast was at risk of significant rain.

Comparison of ensemble members 11, 17 and 22 showed that, common to most ECLs, the strongest surface winds occur to the south of the main low. Each also shows the strengthening of the north-westerly jet and the upper cut-off low west of the surface low. The intensification of the onshore low-level jet was associated with the cut-off low development and upper-level ridging that extended all the way to the surface, thus creating a strong near-surface pressure gradient and strong onshore winds. For all members, rain occurred along the low-level convergence lines to the south of the main low, and also on the eastern edge over the Tasman Sea. However, localized differences between members produced large differences in location and strength of extreme winds as well as in rainfall. While member 22 had an onshore jet directed towards Dungog and maximum rainfall accumulated around the Dungog area, the low level jet and maximum rainfall in member 11 were located further south. In contrast to these two members, member 17 had the strongest low developing offshore and maximum rainfall to the south and to the north-east of the Dungog area.

Comparison of the thermal advection rainfall diagnostic (calculated using gradient wind approximation) with mid-level winds and hourly rainfall showed the tilting of the low core is important and that areas of heavy rain coincided with anticyclonic rotation of winds with height and positive warm air advection (WAA), while rain free areas coincided with negative WAA and cyclonic rotation of winds with height. This analysis showed that this diagnostic approach works well with high-resolution data and could be used for analysing ECL development.

PRACTICAL IMPLICATIONS

These results show how the use of ensembles in studying severe weather events such as ECLs provides a valuable insight into the processes that lead to the development and rapid intensification of these systems. It also provides the opportunity to study their predictability by analysing differences between the simulations. Ensemble prediction has advantages over deterministic methods, including that it is on average more accurate, and that it allows the calculation

of probabilities and the identification of alternative scenarios. These advantages are evident in this study. In addition, a better understanding of the dynamics and predictability of ECLs, as well as other high impact weather events, has important implications not only for forecasters, but also for emergency services preplanning and preparedness.

THE BLUE MOUNTAINS FIRES OF OCTOBER 2013

This chapter is abridged from the article *Ching, S.E., R.J.B. Fawcett, W. Thurston, K.J. Tory and J.D. Kepert, Mesoscale features related to the Blue Mountains Fires of 17 October 2013 revealed by high resolution numerical weather prediction modelling, submitted to Monthly Weather Review.*

SUMMARY

In October 2013, several fires broke out in the Blue Mountains of New South Wales, Australia, and were devastating to the region. Of particular interest is the State Mine Fire, which was lit on 16 October, then spread rapidly eastward during the afternoon of 17 October. To investigate the meteorological conditions during that day, the Bureau of Meteorology's numerical weather prediction (NWP) model was run at very high resolution, with a horizontal grid spacing of about 440 m, to simulate the weather conditions on the day. Several mesoscale features were identified which could account for the rapid fire spread. The first was a mountain wave structure with very strong downslope winds developing over the fire ground during the afternoon of 17 October, accompanied by hot and dry atmospheric conditions. The second was a slot of dry air with an approximate width of 50 km that passed over the fire ground around and shortly after midday which likely exacerbated the fires. The third was an undular bore that formed during the night of 16 October, which was related to the formation of the dry slot. The formation and evolution of these mesoscale features are described, and existing theories are considered to explain these phenomena.

INTRODUCTION

In October 2013, a number of significant fires broke out and created havoc in New South Wales, Australia. The most intensive fire activity occurred between 13 and 26 October, when there were 627 incidents and an estimated area of 164054 ha burnt. In particular, more than 200 houses in the Blue Mountains were damaged during the afternoon of 17 October, although, thankfully, no lives were lost (New South Wales Rural Fire Service 2014).

The fires in the Blue Mountains Region proper consist of the State Mine Fire and the Mount York Road Fire. The State Mine Fire was ignited on 16 October and spread to the south-east during the night and the morning of 17 October. Later, the fire spread very rapidly to the east from about noon. According to the analysis performed internally by New South Wales Rural Fire Services, the estimated burnt area increased from 1036 ha at 11:56 am to 12436 ha by 9:46 pm local time. The Mount York Road Fire was ignited on the afternoon of 17 October. While far less extensive than the State Mine Fire, it had an estimated burnt area of 492 ha by 7:46 am (AEDT) on 18 October (Figure 21).

The areal extension of the State Mine Fire during the afternoon of 17 October was phenomenal – an increase of 11400 ha (more than 10-fold) in less than 10 hours (Table 2). It is of both practical and academic interest to investigate whether the meteorological conditions had been conducive to the rapid

spread of the fire during that day; if so, what were those meteorological conditions or features? We have tried to answer this question by performing a simulation with an operational NWP system but with much higher horizontal resolution, and have identified several mesoscale features of interest.

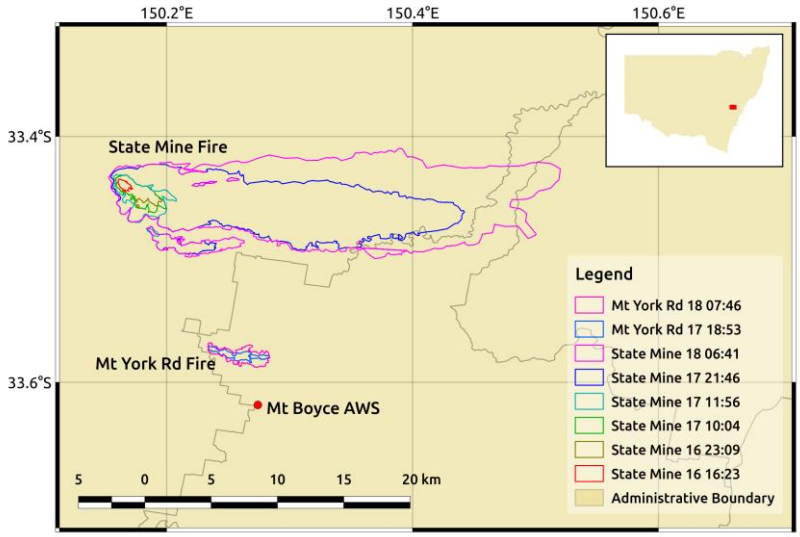

Figure 21. The progression of the perimeters of the State Mine Fire and the Mount York Road Fire. The times are in Australian Eastern Daylight Time (AEDT), which is 11 hours ahead of UTC. Location of Mount Boyce AWS is shown by the red dot. The inset shows the map of New South Wales, Australia, with the red box representing the areal extent of this map.

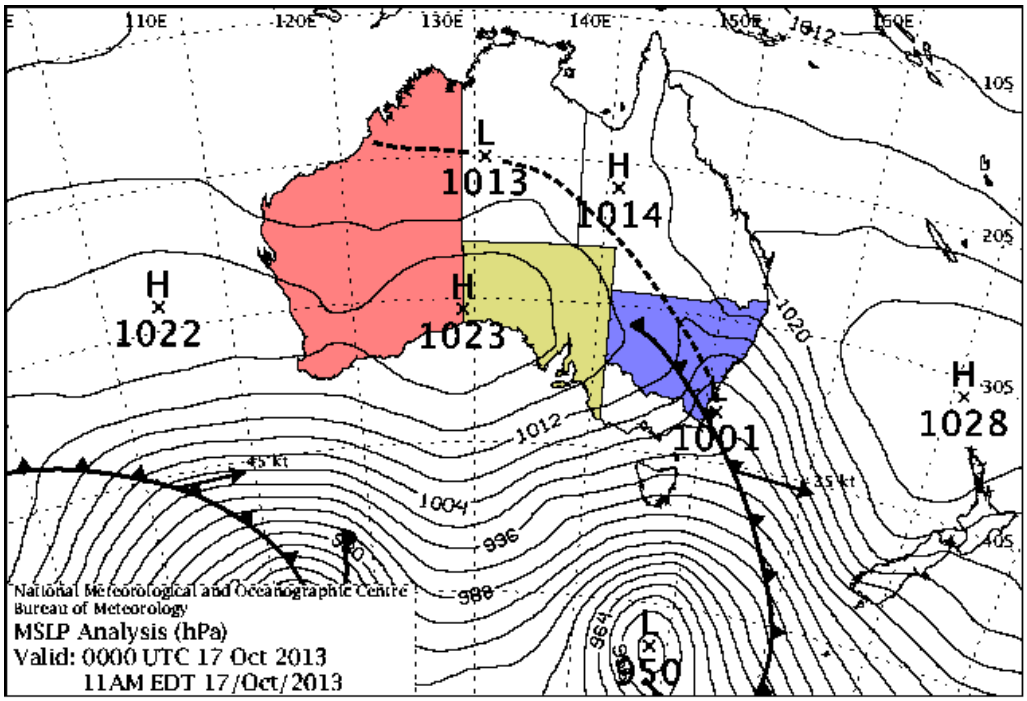

Figure 22. Operational mean sea level pressure chart by Bureau of Meteorology at 0000 UTC 17 October 2013. The States Western Australia, South Australia and New South Wales are tinted red, yellow and blue respectively.

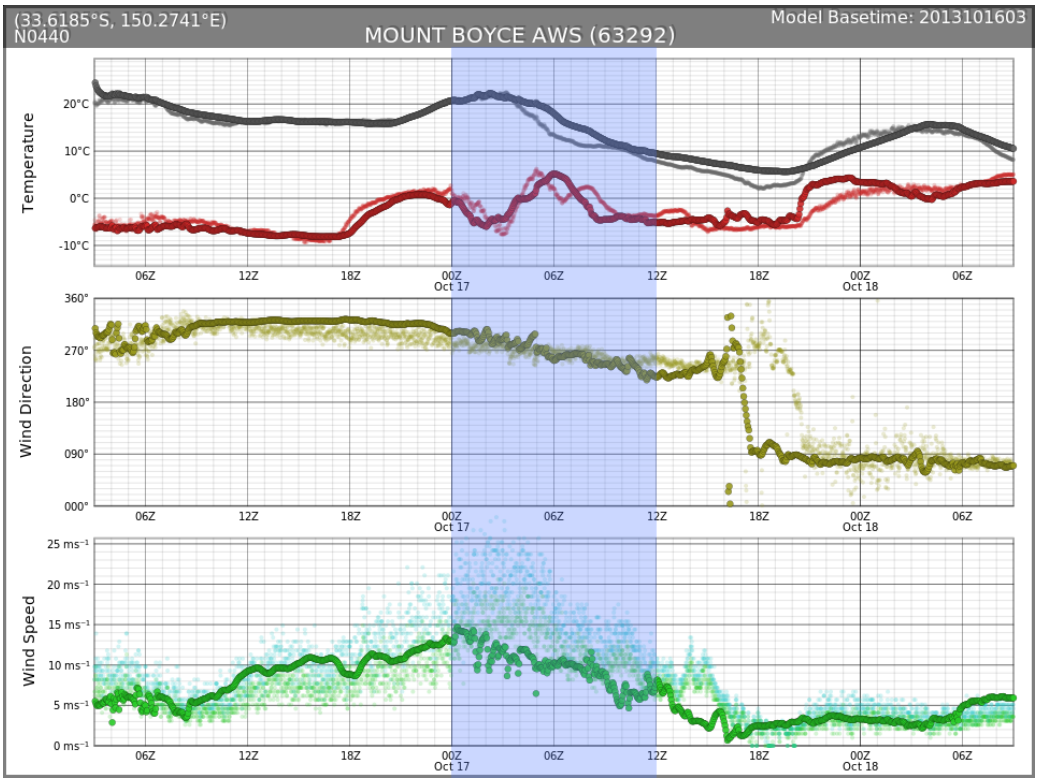

Figure 23. Meteogram of 2-metre temperature, 2-metre dew point, 10-metre wind direction, 10-metre wind speed and 10-metre wind gust at Mount Boyce with AWS observational data and N0440 model data. The solid dots in the foreground are NWP simulation data in 5-minute resolution. The fainter dots are AWS observation data in 1-minute resolution. Black dots are temperatures, red dots are dew point temperatures, yellow dots are wind directions, green dots are wind speeds and cyan dots are wind gusts. The translucent blue box highlights the time during the rapid spread of the State Mine Fire.

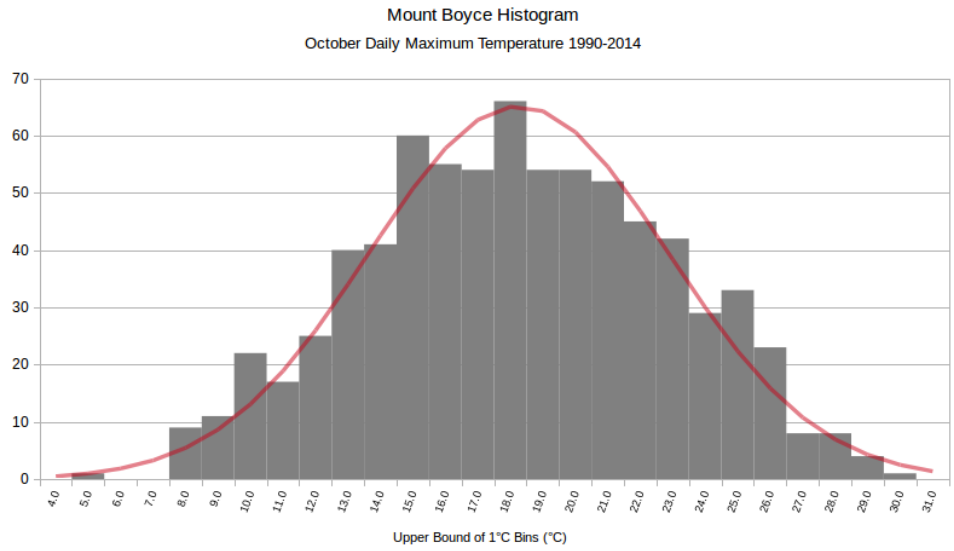

Figure 24. Histogram of daily maximum temperatures at Mount Boyce AWS in October from 1990 to 2004. The red curve is the fitted Gaussian distribution.

Table 2. Fire Perimeters.

Fire	Date	Local time (AEDT)	Estimated burnt area (ha)
State Mine Fire	16 October 2013	4:23 pm	65
		23:09 pm	433
	17 October 2013	10:04 am	578
		11:56 am	1036
		9:56 pm	12436
	18 October 2013	6:41 am	22780
Mount York Road Fire	17 October 2013	6:17 pm	183
		6:53 pm	201
		7:46 am	492
	18 October 2013	9:30 am	623

Table 3. Comparison of mean monthly rainfall and Year 2013 monthly rainfall at Mount Boyce from July to October.

Month	Mean	Year 2013
July	40.6mm	13.0mm
August	54.8mm	15.4mm
September	53.6mm	40.6mm
October	64.5mm	12.8mm

Table 4. Various measures indicating dryness in the Blue Mountains area in October 2013 and the lead up period. All entries are values at Mount Boyce interpolated from the AWRA L4.5 database at 0:25_ horizontal resolution, for October 2013 (unless otherwise stated) against previous and subsequent Octobers. Effective Rainfall is the difference between rainfall and evapotranspiration.

Dryness Measure	Value
Top Layer (0 cm to 10 cm) Soil Moisture	4.29 percentile
Mid Layer (10 cm to 100 cm) Soil Moisture	2.88 percentile
Rainfall	7.31 percentile
Mid Layer (10 cm to 100 cm) Soil Moisture Anomaly	-41.49mm
Effective Rainfall Anomaly	-41.55mm
Effective Rainfall Anomaly August to October 2013	-92.75mm

FIRE GROUND CONDITIONS

The several months leading up to October 2013 were quite dry in the Blue Mountains area. Rainfall recorded at Mount Boyce, a hill in the Blue Mountains area with a Bureau of Meteorology maintained Automatic Weather Station (AWS) that is closest to the Blue Mountains fire grounds (Figure 21), had been substantially below average since July (Table 3). The soil dryness from the Australian Water Resources Assessment System (AWRA) (Vase et al. 2013) analysis also shows that it was exceptionally dry in the Blue Mountains area in the lead up of the fires (Table 4). The drought factor at Mount Boyce, interpolated from the Bureau of Meteorology's operational gridded analysis (Finkele et al. 2006), was 8.7.

Figure 22 shows the operational synoptic mean sea level pressure chart at 0000 UTC 17 October 2013. An anticyclone was centred over the Tasman Sea north of New Zealand, and a ridge of high pressure extended from the west, covering Western Australia and South Australia. A deep low pressure system was centred in the Southern Ocean. It extended a cold front northwards which was crossing New South Wales during that day, preceded by a prefrontal trough which extended to northern Australia.

Figure 23 shows the meteogram from 0300 UTC 16 October 2013 to 0900 UTC 18 October 2013 at Mount Boyce. The cold front and the prefrontal trough manifested at Mount Boyce as1 a gradual backing from north-westerlies during the morning to south-westerlies by the afternoon on 17 October 2013. Several smaller wind directional changes were embedded in the larger scale backing of the winds.

The maximum temperature of the day recorded by the Mount Boyce AWS was 22.5°C (recorded at 0311 UTC and 0313 UTC). Considering the altitude of the AWS at 1080m above mean sea level and the time of the year, it was a somewhat hot day. Checking against the climatological data (1990 to 2014, inclusive) for October daily maximum temperature at Mount Boyce AWS, 22.5°C converts to a percentile rank of 82.2. Figure 24 shows the histogram of October daily maximum temperatures at Mount Boyce which fits very well with a Gaussian distribution with a mean of 17.8°C and a standard deviation of 4.6°C. The goodness of fit can be illustrated by checking that 22.5°C is about 1.02 standard deviations above the mean, which is equivalent to a percentile rank of about 84.6.

The humidity on 16 October in the Blue Mountains area was very low, with dew point temperatures recorded at Mount Boyce AWS consistently below -5°C. From about 1800 UTC 16 October 2013, the dew point temperatures increased to around 0°C, before decreasing sharply during the early afternoon of 17 October, to a minimum of -7.6°C around 0300 UTC 17 October. The dew point temperature then increased again, quite abruptly, from about 0°C to 5°C from 0400 UTC to 0900 UTC. It was also windy in the Blue Mountains area on 17 October. The Mount Boyce AWS meteogram shows clearly that winds picked up during the afternoon, with 10-minute mean winds predominantly above 12 m s^{-1} between about 0000 UTC and 0600 UTC. During this time, the maximum 10-minute wind recorded was 17.4 m s^{-1}, the maximum 1-minute wind recorded was 20.6 m s^{-1} at 0243 UTC while the maximum gust recorded was 28.3 m s^{-1} at

0237 UTC. Putting in the drought factor (8.6), daily maximum temperature (22.5°C), lowest dew point temperature (-7.6°C) and highest 10-minute wind speed during the afternoon (17.4 m s^{-1}) into the calculation of FFDI yields a number of 63.2, which is categorised as a Forest Fire Danger Rating (FFDR) of "Severe".

NUMERICAL SIMULATION

Configuration

The simulation was performed using the Australian Community Climate and Earth-System Simulator (ACCESS), involving a sequence of nested limited-area models embedded within ACCESS global model runs. The numerical weather prediction (NWP) modelling framework is closely related to the Bureau of Meteorology's operational NWP arrangements but run at higher resolutions than is currently employed in real-time operations. The central core of the ACCESS configuration is the UK Met Office's Unified Model (version 8.5). It is a non-hydrostatic model with an Arakawa-C grid in the horizontal and a Charney-Phillips grid in the vertical (Puri et al. 2013).

The simulation was initialised at 0300 UTC 16 October 2013 and run for 54 hours from the initialisation time. Global initial conditions were real-time analyses prepared by the Bureau of Meteorology's National Operations Centre (BNOC). Within the global model run, which has a grid spacing of around 40 km at the equator), three nested limited-area model runs, named "N4000", "N1300" and "N0440", were embedded with grid spacing of approximately 4 km, 1.3 km and 440m respectively (Figure 25). The nested grids were regular latitude-longitude grids, with a larger longitudinal grid spacing (as measured in degrees of longitude) than latitudinal grid spacing, so as to make the central grid rectangles approximately square, accounting for the meridional convergence. Each stage of the simulations (global + nested) used 70 model levels in the vertical direction. These levels are terrain-following in the lowest levels, transitioning smoothly to constant heights above mean sea level in the highest levels. The global model had a model top of 80 km, while the three nested models had model tops of 40 km. The lowest temperature, humidity, and vertical motion levels in the three nested models were 5m above the surface, while the lowest horizontal winds were 2.5m above the surface. The 1.3-km and 440-m models used a three-dimensional sub-grid turbulence scheme of Smagorinsky type, while the 4-km model used the planetary boundary layer parameterisation.

Evaluation of Simulation near the fire ground

Comparison of the NWP model surface and AWS observations at Mount Boyce on 17 October (Figure 23) shows that the conditions at the AWS were reasonably well simulated. The maximum temperature of the day was very well captured, although the cooling associated with the wind change from about 0300 UTC to 0400 UTC in the simulation is not as quick as observed. The simulated minimum temperature on the morning of 18 October was also about 3°C to 4°C warmer than observed. In general, the simulated dew point temperature time series matched quite well with the AWS observations,

specifically, the very low humidity on 16 October, an increase of dew point temperatures from about 1800 UTC 16 October, and a period of abrupt drying around 0300 UTC (albeit the simulation had this early by about 1 hour). A secondary dryness around 0700 UTC in the AWS observations was, however, missed by the simulation.

The biggest inaccuracy is that the model simulated 10-metre winds did not fully capture the high winds observed during the afternoon of 17 October. Between 0000 UTC and 0600 UTC 17 October, when the AWS observations indicated an increase of wind speeds, the NWP model winds showed a slight decline. The simulation did pick up increased windiness above the surface (Figure 29 and Figure 30), which indicates that this error is perhaps due to a near-surface bias in the model winds. Another error in the simulation is the early arrival, by three hours, of an easterly change during the early morning of 18 October (around 2100 UTC 17 October). This is likely due to the complexity of the development of a Southerly Buster off the New South Wales coast reaching the Blue Mountains area during the early morning of 18 October, and the simulation has not captured this complex feature very well. The wind before the arrival of this easterly change was calm, and the simulation did not capture the calm winds between 1700 UTC 16 October and 2100 UTC 16 October, which likely accounts for the error in the simulated minimum temperature through a lack of radiation inversion.

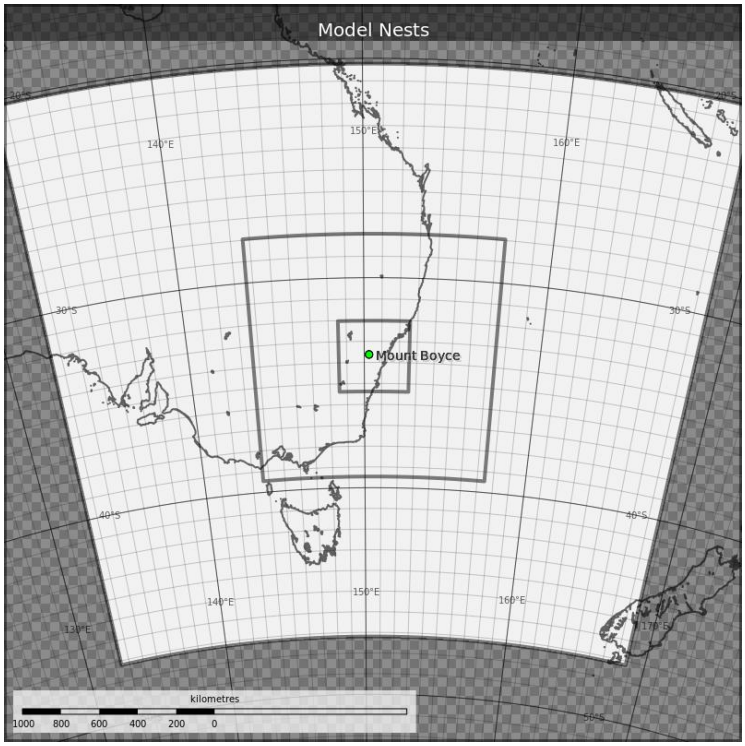

Figure 25. Domain boundaries for the three nested limited-area models, progressively from N4000 (largest) to N1300 and N0440 (smallest). N4000 is nested directly in the global model. Grid spacings are approximately 4:0 km (N4000), 1:3 km (N1300) and 440m (N0440). The dot in the centre marks the approximate location of Mount Boyce in the Blue Mountains.

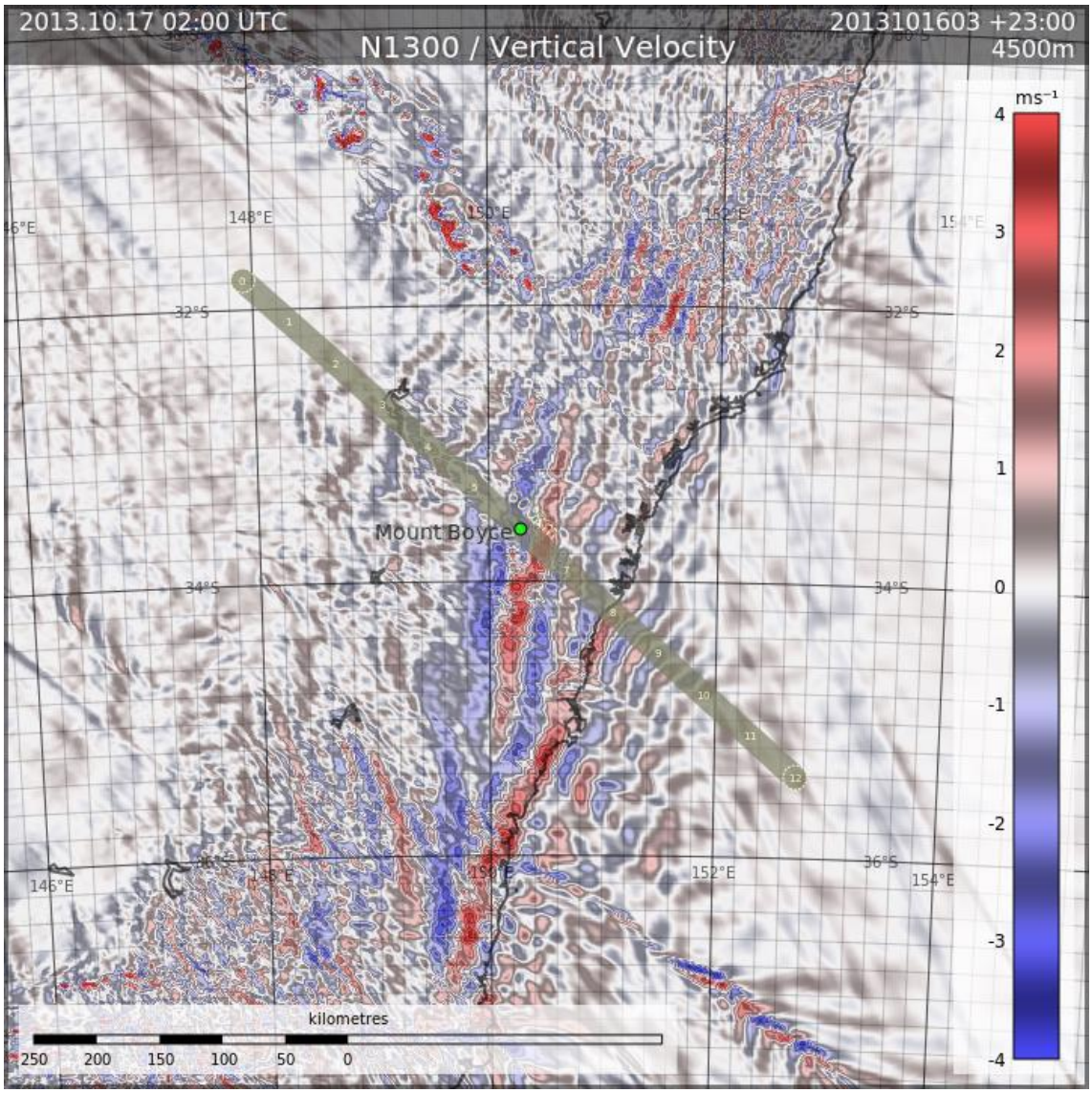

Figure 26. NWP model simulated 4500m above mean sea level vertical velocity at 0200 UTC 17 October 2013 from the N1300 nest. The thick line running northwest to southeast depicts the extent of the vertical cross section in Figure 8, Figure 9, Figure 10 and Figure 11.

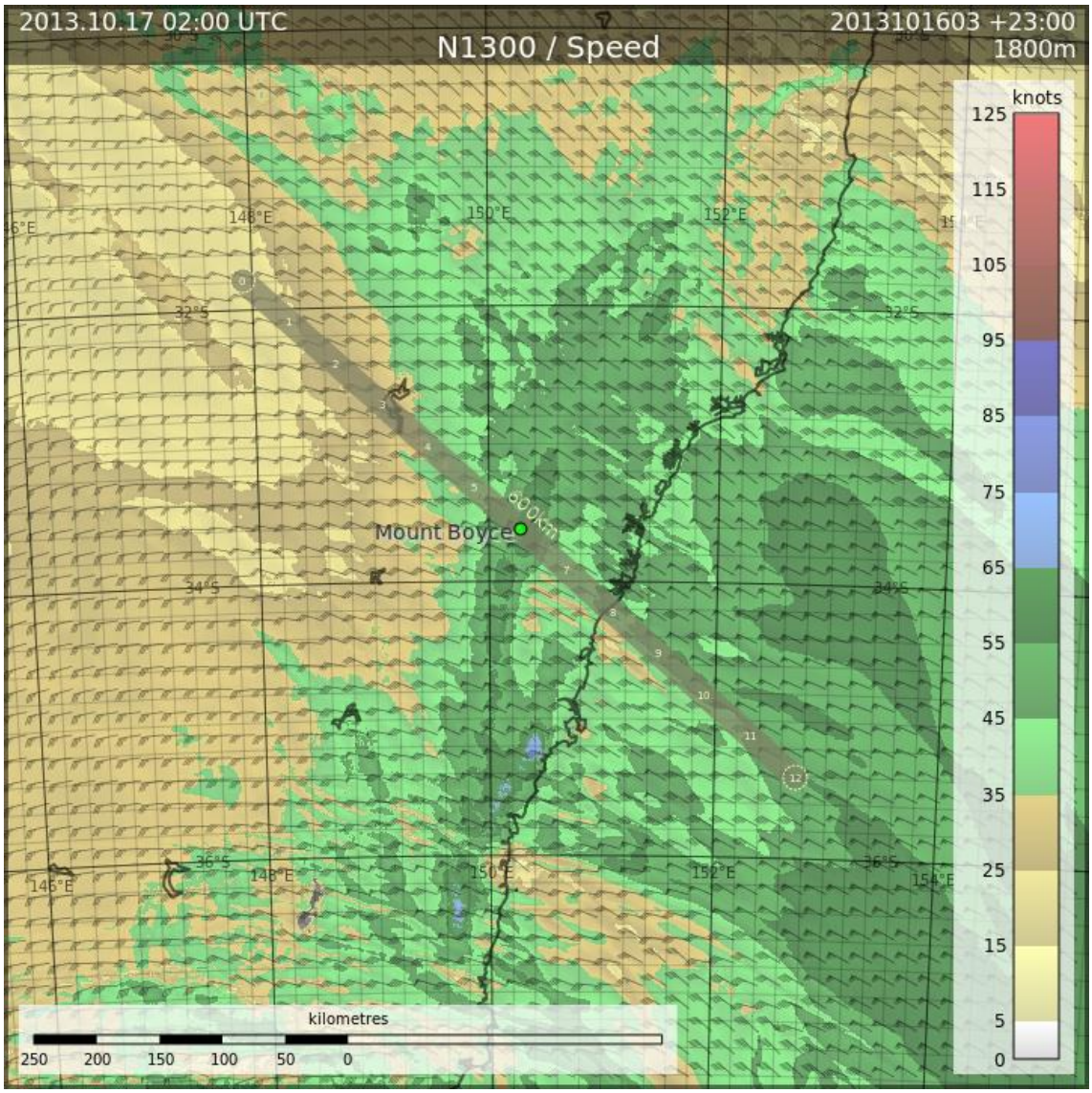

Figure 27: As in Figure 6 but for 1800m above mean sea level horizontal wind speed, also with wind barbs overlaid.

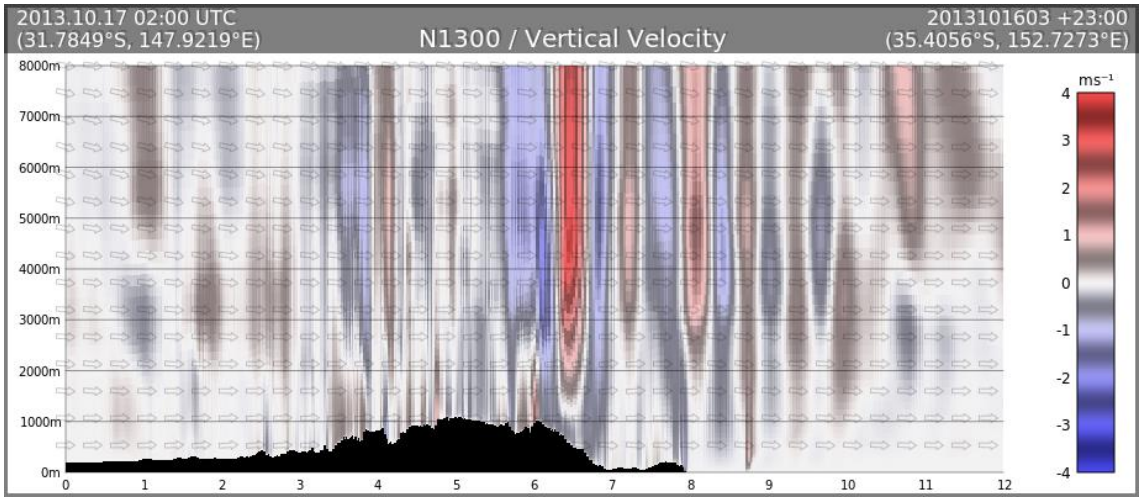

Figure 28. NWP model simulated vertical cross section of vertical velocity at 0200 UTC 17 October 2013 from the N1300 nest. This vertical cross section is 600 km long and is depicted in Figure 6. The numbers 0 to 12 in the horizontal axis are equidistant markers which are 50 km apart. Mount Boyce is located at the position marker 6. Faint arrows indicate the three-dimensional wind direction projected onto the vertical cross sectional plane.

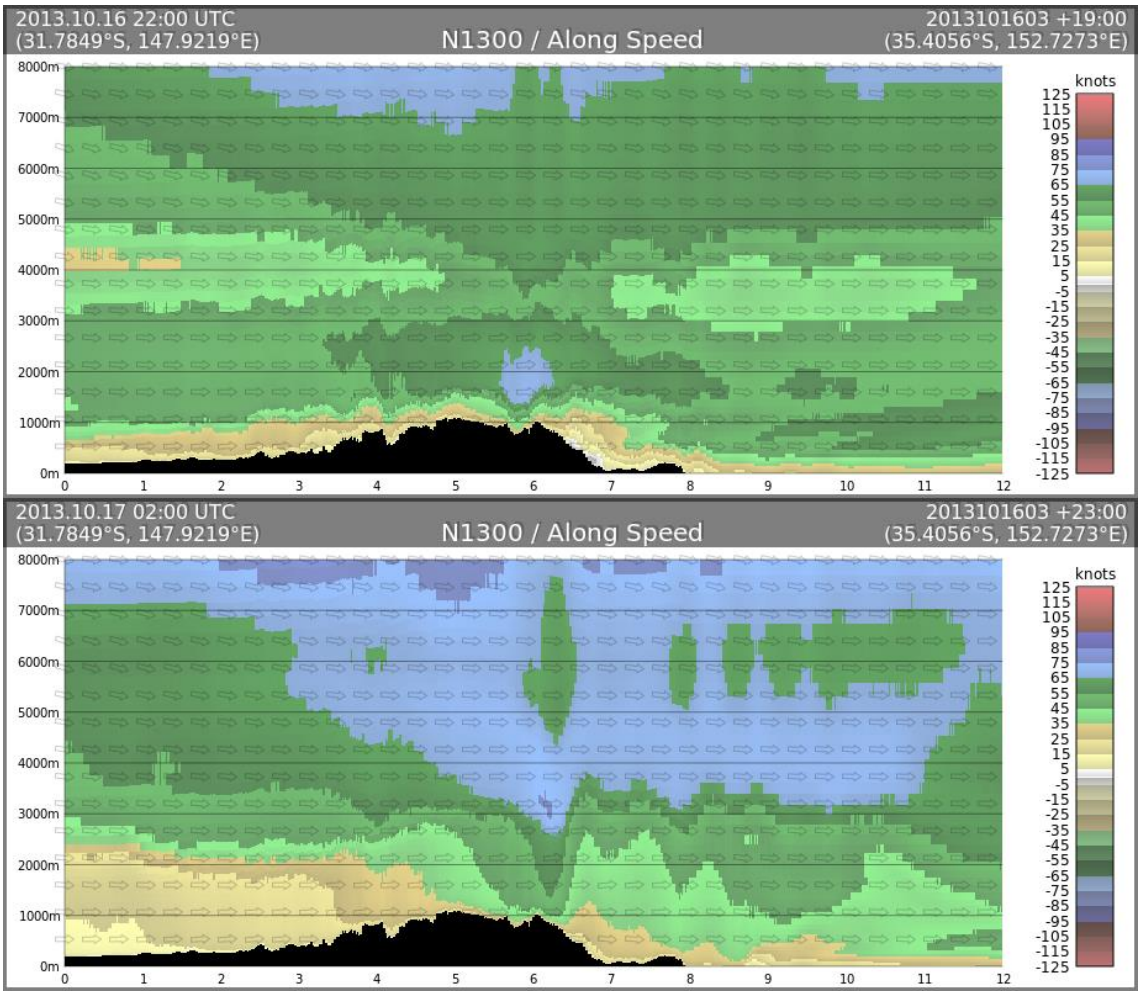

Figure 29. As in Figure 8 but for horizontal winds projected onto the vertical cross section plane for 2200 UTC 16 October and 0200 UTC 17 October.

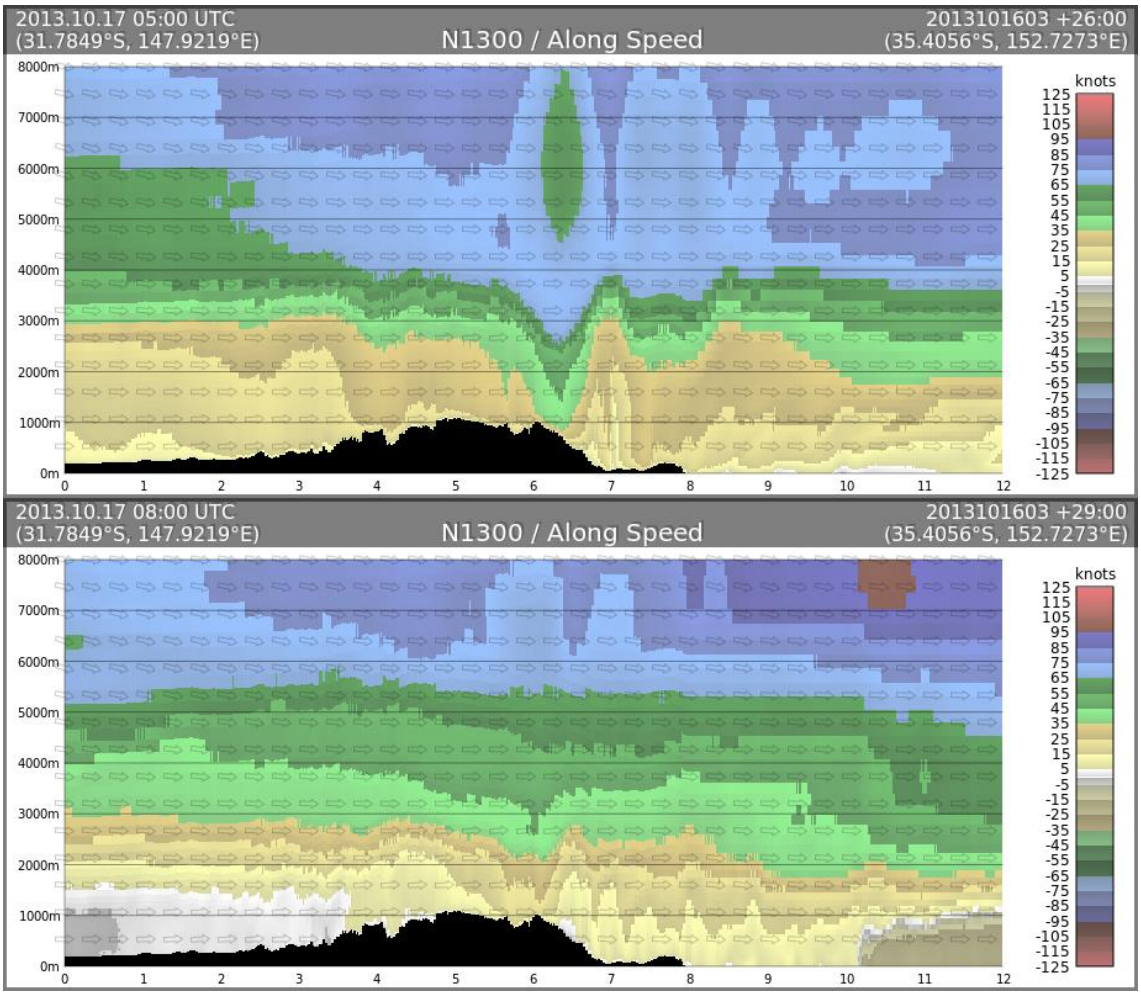

Figure 30. As in Figure 9 but for 0500 UTC 17 October and 0800 UTC 17 October.

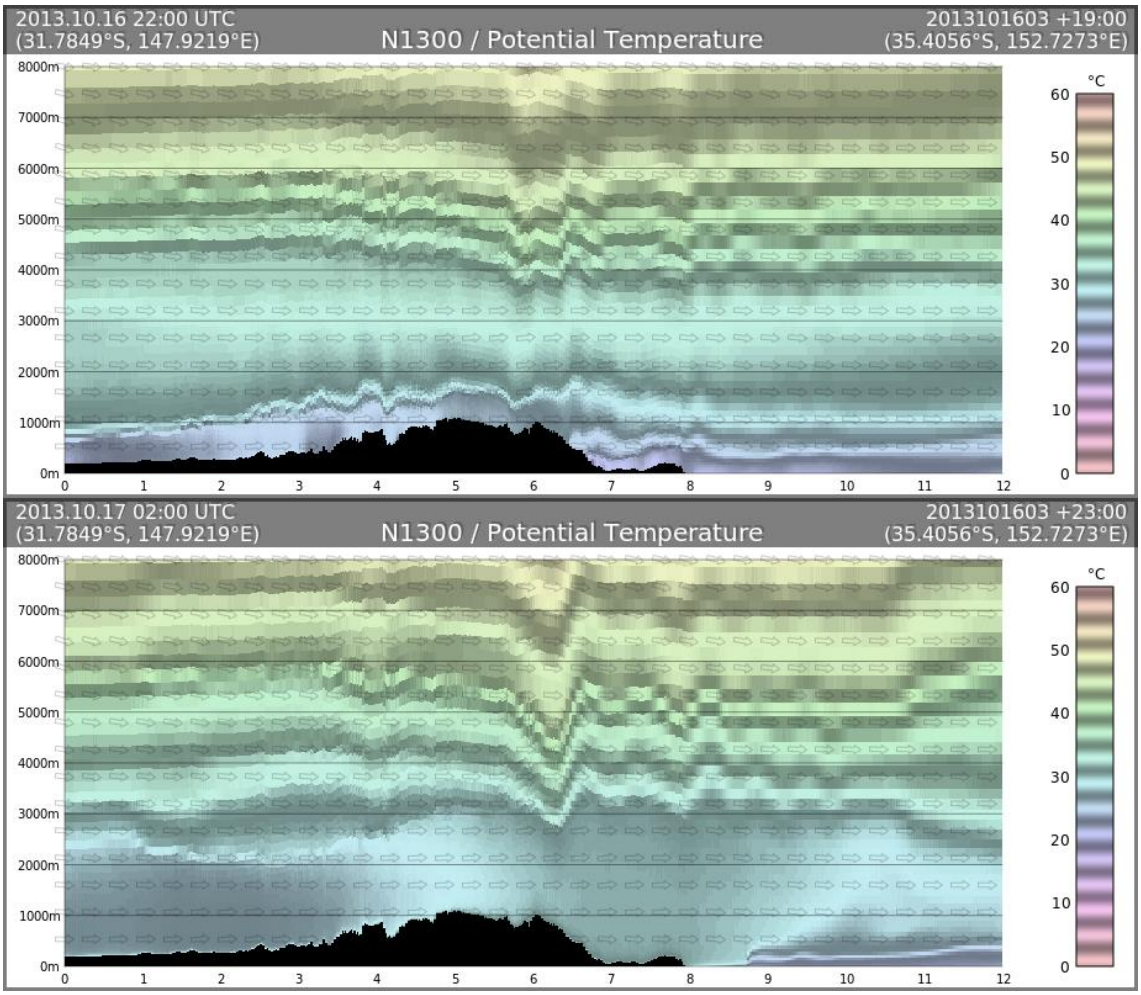

Figure 31. As in Figure 9 but for potential temperature.

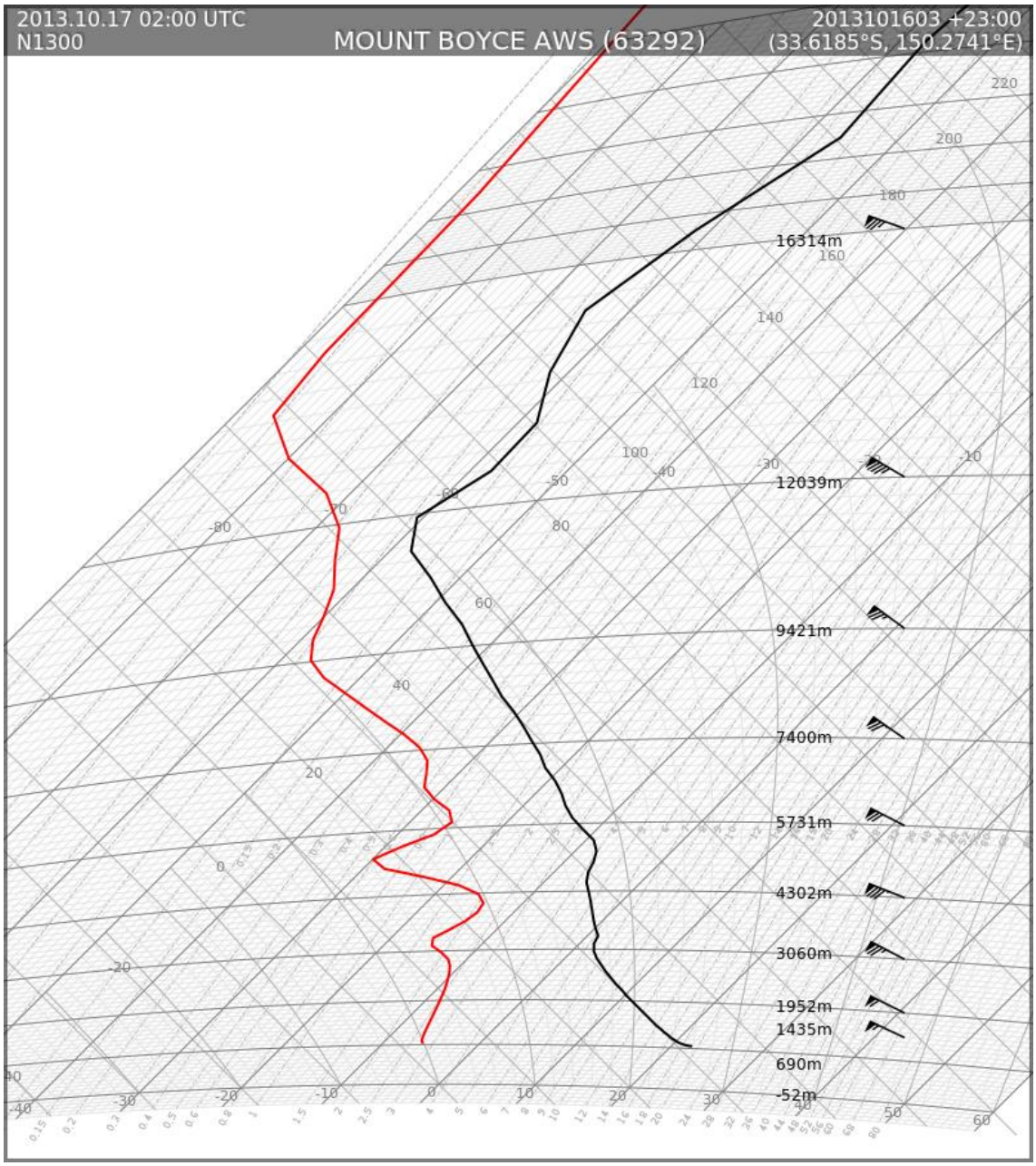

Figure 32. Tephigram of NWP model simulated vertical profile at Mount Boyce at 0200 UTC 17 October 2013 from N1300 nest.

MESOSCALE FEATURES

Downslope winds

A mountain wave pattern was detected in the Blue Mountains region (Figure 26), and an area of enhanced low level downslope winds was present on the downslope side of the mountain ranges (Figure 27) in the simulation. A vertical cross section of vertical wind speed running northwest to southeast across Mount Boyce at 0200 UTC 17 October (Figure 28) clearly depicts a mountain wave pattern with an approximate horizontal wavelength of 35 km. Figure 29 and Figure 30 show several vertical cross sections of horizontal wind speed projected onto the same cross-sectional plane as in Figure 28. At 2200 UTC 16 October, there was a low level wind max near Mount Boyce (at position marker 6) (Figure 29, top panel) which was related to an area of low level temperature inversion (Figure 31, top panel). By around 0000 UTC 17 October, the low level inversion was broken and the low level wind max relaxed both upstream and downstream of Mount Boyce as the horizontal momentum mixed out by the vertical mixing. However it remained rather windy in the vicinity of Mount Boyce and the immediate areas to the lee of the terrain, forming the pattern of a marked area of enhanced horizontal winds near Mount Boyce and the immediate areas to the lee of the terrain (Figure 29, bottom panel). The model tephigram (Figure 32) located at Mount Boyce at 0200 UTC 17 October indicates that the atmospheric column was dry and adiabatic up to a height of about 3 km above mean sea level. Wind speeds were nearing 60 knots (30.8 m s^{-1}) within this unstable, dry air column.

This pattern persisted until around 0500 UTC 17 October (Figure 30, top panel), then somewhat weakened before mostly disappearing by about 0800 UTC 17 October (Figure 30, bottom panel). It is apparent that the strengthened downslope winds were conducive to the rapid fire progression during the afternoon of 17 October. While in the previous section it was noted that the NWP simulated 10-m winds were much less that the observed winds, the existence of an area of increased winds in the upper levels about and in the lee of the Blue Mountains ranges (as depicted by the form of a marked downward extension of stronger winds from aloft (Figure 29 and Figure 30) was a feature that was likely to have occurred during that afternoon and was responsible for the marked increased in observed surface winds speeds. Moreover, the neutral stratification, coupled with a fiercely burning fire at the surface, would have been likely to promote the formation of pyrocumulonimbus clouds reaching the tropopause about 12 km above mean sea level (Figure 32). At these heights, winds were reaching 60 to 70 knots (31 m s^{-1} to 36 m s^{-1}), and firebrands could be lofted and then transported downstream to great distances. We suggest that these are likely to be responsible for the rapid spread of the Blue Mountains Fires during the afternoon of 17 October.

Dynamically forced downslope winds in the lee of mountain ranges have been observed and well documented at many locations worldwide and have received much research effort. The escalations in fire activities at Margaret River (Kepert and Fawcett 2013) and Aberfeldy (Wells et al. 2014), which were also likely due to enhanced downslope winds, also occurred during the night

time. However, this Blue Mountains case is of particular interest because the phenomenon occurred during the day with a deep unstable layer that extended to about 3 km above mean sea level, which is apparent in both the tephigram at Mount Boyce (Figure 32) and the vertical cross section of the potential temperature (Figure 31).

Dry slot

The simulation also revealed the presence of a slot of dry air moving across the Blue Mountains area during the afternoon of 17 October, quite possibly related to the abrupt drying around 0300 UTC as observed in the Mount Boyce AWS. Figure 33, which shows the simulated 2-metre specific humidity at 0145 UTC 17 October, clearly depicts the existence of the dry slot which moved across the Blue Mountains area. A time evolution of the surface specific humidity (Figure 41 and Figure 42) shows that the dry slot was actually not formed within a wetter region of air. Rather, as the moist air-mass from the southwest, associated with the wind change, encountered the moist northerlies over northern New South Wales around 2200 UTC 16 October, the dry area between the two air masses was squeezed into a narrow strip and was maintained until around 0700 UTC 17 October. It is recognised that these moist northerlies are responsible for the increased dew point temperatures observed at Mount Boyce during from 1800 UTC 16 October to 0000 UTC 17 October before the arrival of the dry slot (Figure 23).

Previous studies (Mills 2005, 2008) suggested that such dry slots could be related to middle atmospheric dryness being transported down to the surface ahead of the front by a vertical cross frontal circulation. This theory was supported by middle atmospheric dryness revealed from satellite water vapour imageries in Mills' cases. However, in our study, such middle atmospheric dryness was not seen in the satellite water vapour imagery (Figure 34), and, indeed, the simulated vertical profile do not agree with the notion of middle atmospheric dryness supporting the maintenance of the dry slot (Figure 32). In the vertical profile, there was no marked mid-atmospheric dry layer, but a somewhat moist layer around 3.5 km to 4.5 km, and another around 5 km to 7.5 km, in reasonably good correspondence with the satellite water vapour imagery.

Figure 35 shows a stack of aligned vertical cross sections of simulated specific humidity, vertical velocity and potential temperature, running southwest to northeast at 0145 UTC 17 October, when the dry slot was directly over the Blue Mountains area. The simulated dry slot was about 100 km wide and 3 km deep, with a somewhat moist layer around 3.5 km to 4.5 km, and another around 5 km to 7.5 km, corresponding well with the tephigram (Figure 32). There was upward motion in the north-eastern (right) side of the dry slot and downward motion in the southwestern (left) side of the dry slot, resembling a vertical circulation with the strongest vertical motion between 4 km and 5 km above mean sea level. However it did not appear to be directly related to a frontal invasion as per Mills' cases, but rather, the undulations of the topography. To illustrate this point, Figure 36 shows a similar stack of vertical cross sections several hours earlier at 2030 UTC 17 October. The kink in the potential temperature between the markers 2 and 3 (about 180 km to the southwest of Mount Boyce which is at marker 6) was about 100 km ahead of the moisture discontinuity, and was

associated with a skewed dipole of vertical velocity within the layer below 4.5 km from mean sea level (highlighted by the green ellipse in the middle panel), with the downward motion confined below 3.5 km. Back to Figure 35, the moist layer around 3.5 km to 4.5 km was somewhat distorted by this vertical circulation, but it is not apparent that the dryness within the dry slot below 3 km is related to this vertical circulation. This suggests the notion of vertical cross-frontal circulation dragging down dry middle atmospheric air, as suggested in the papers by Mills (2005, 2008), is not likely to be responsible for the formation and maintenance of the dry slot in this case. Apparently, another mechanism is responsible for this.

To investigate this other mechanism, we note that the north-western portion of the dry slot is much better defined than over the Blue Mountains area (Figure 33), presumably because of the absence of significant terrain and other complicating factors. Therefore, we focus away from the Blue Mountains area, in this north-western portion of the dry slot instead.

Figure 37 and Figure 38 show a sequence of the simulated 10-metre wind direction and 2-metre specific humidity around the north-western portion of the wind change from 1700 UTC 16 October to 0000 UTC 17 October, with a marker X following the leading edge of the wind change. It is clear from the figures that the moisture discontinuity lagged behind the wind change, which resembles an undular bore. The dry slot formed as the dry area was wedged between the two moist air-masses from the southwest and the northeast, and was maintained following the convergence of the two air masses. Figure 39 and Figure 40 show a sequence of vertical cross sections of simulated potential temperature and specific humidity following marker X in Figure 37 and Figure 38, with the faint circles corresponding to the position of marker X. The speed of the marker X is shown on the top right hand corner of the vertical cross section. Before encountering the north-eastern moist air-mass at around 2200 UTC 16 October, marker X travelled at a speed of around 15 m s^{-1}, and decelerated to around 6.5 m s^{-1} after the undular bore encountered the north-eastern air-mass around 2230 UTC 16 October. The dry slot maintained its width thereafter.

It is apparent that the dry air between the undular bore and the moisture discontinuity appears like a "dry nose", attached to the head of the southwestern moist air-mass. Upon convergence with the north-eastern moist air-mass, the "dry nose" was trapped within the two air masses, becoming the dry slot, and continued moving north-eastwards for the next several hours. The simulated dry slot at 0000 UTC 17 October was about 50 km in width with asymmetric depths of moist air on both sides, about 1.3 km in the southwestern side and 3 km in the north-eastern side.

Trajectory analysis was performed to illustrate that the slot of dry air was simply advected by the winds during the afternoon of 17 October. A set of 16 parcels (marked as letters A to P) were placed within the dry slot 400m above ground level at 0100 UTC 17 October, and the trajectories of these air parcels were then calculated by integrating both forward and backward for 7 hours.

Figure 41 and Figure 42 show the trajectories of these parcels from 1800 UTC 16 October to 0800 UTC 17 October. It is clear from the figure that the air parcels lined up at around 2300 UTC 16 October, and approximately defined the dry

slot from about 0000 UTC 17 October to about 0400 UTC 17 October, before encountering moist convective outflow from the north. Parcels B, C, and D were lifted by the moist outflow from the north at around 0400 UTC 17 October, with parcels A, E, F, G, and H following in the subsequent hours. By 0800 UTC 17 October, all the parcels were lifted from near the surface and the dry slot was dissipated.

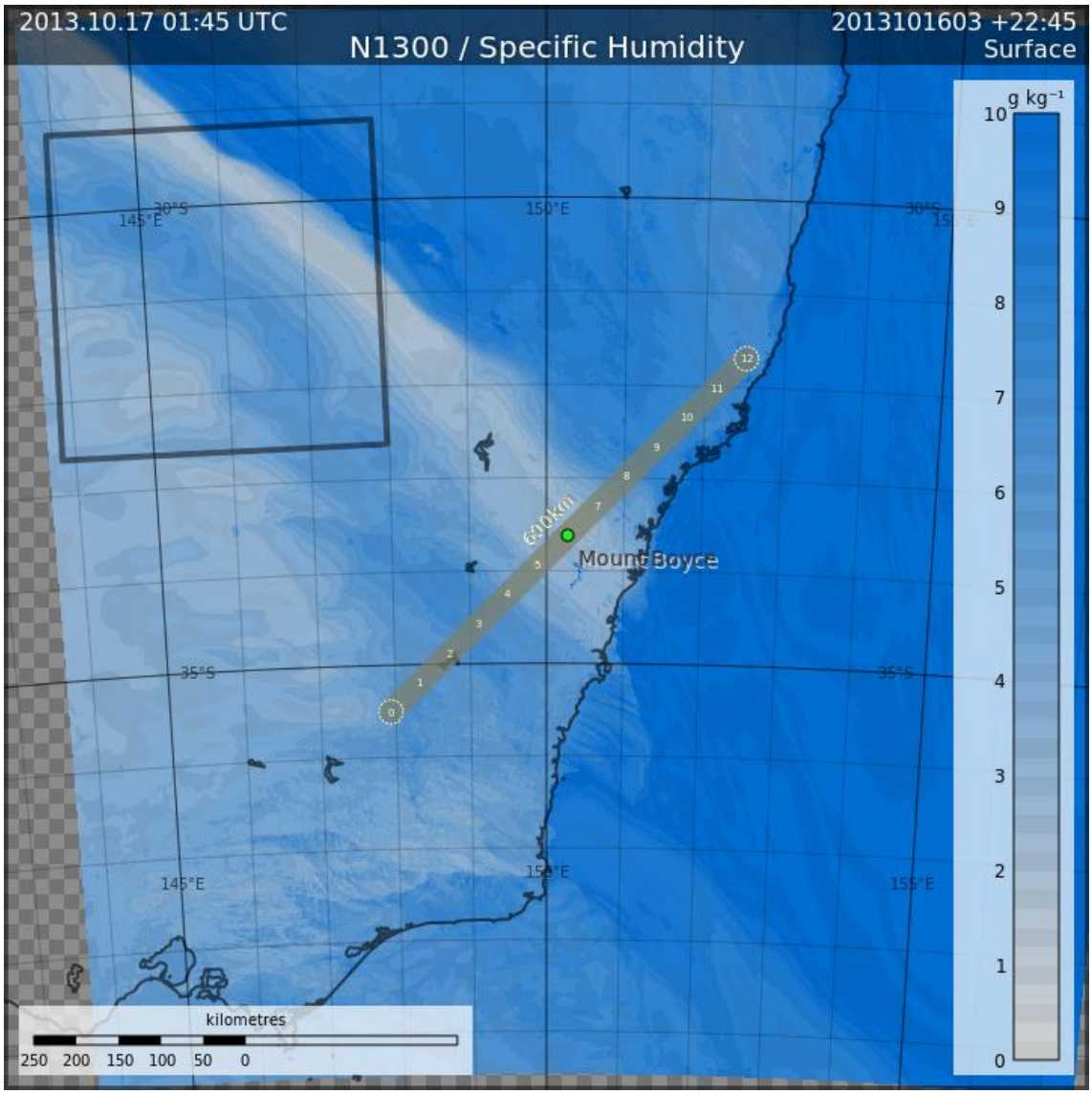

Figure 33. NWP model simulated 2-metre specific humidity at 0145 UTC 17 October 2013 from N1300 nest. The box in the northwest depicts the domain of the charts in Figure 37 and Figure 38. The line running southwest to northeast depicts the extent of the vertical cross section in Figure 35.

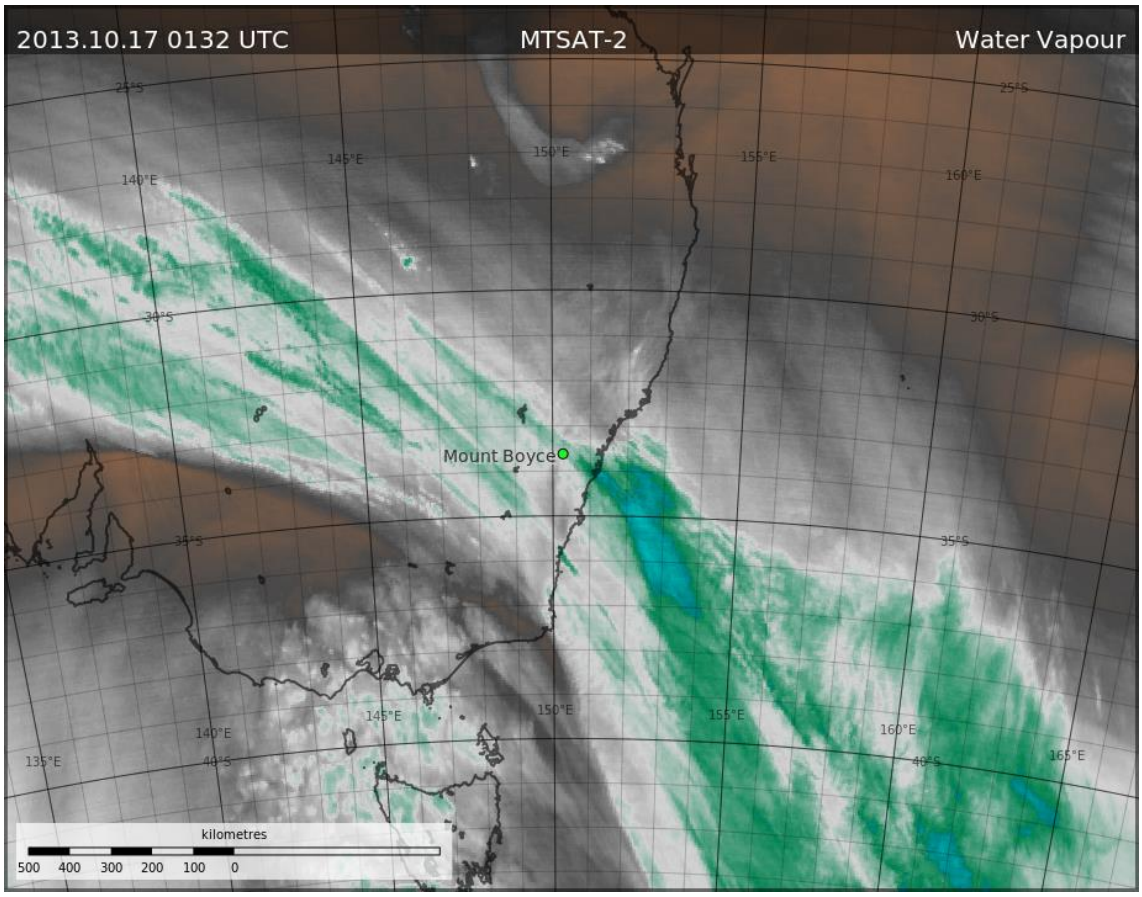

Figure 34. Water vapour imagery at 0132 UTC 17 October 2013 from the MTSAT-2 meteorological satellite. Colour enhancement shows very dry air as brown and more moist air progressively as grey, white, green and cyan.

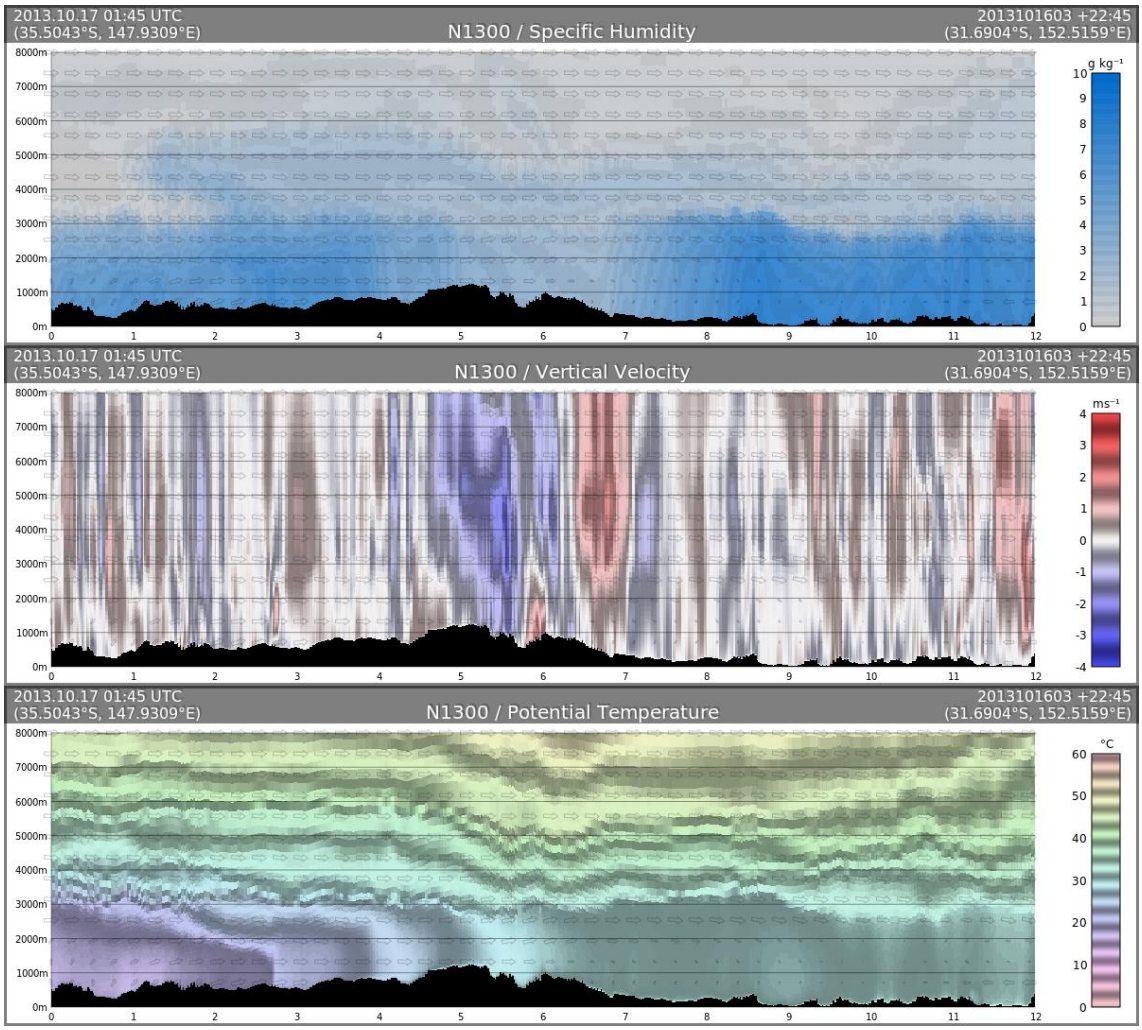

Figure 35. NWP model simulated vertical cross section of specific humidity, vertical velocity and potential temperature at 0145 UTC 17 October 2013 from the N1300 nest. The extent of this vertical cross section is 600 km long and is depicted in Figure 33. Numbers 0 to 12 at the bottom are equidistant position markers which are 50 km apart. Faint arrows indicate the three-dimensional wind direction projected onto the vertical cross sectional plane.

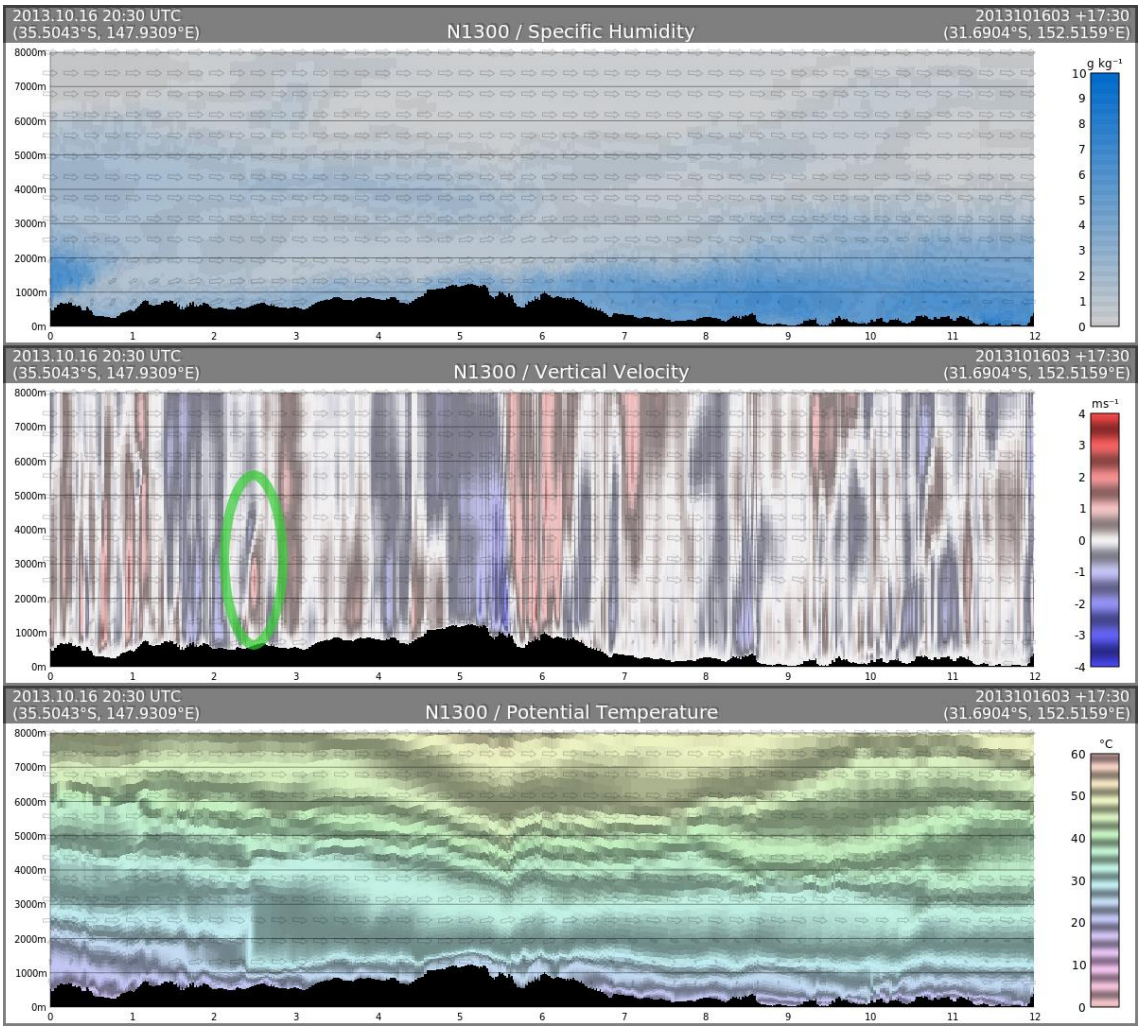

Figure 36. As in Figure 35 but for 2030 UTC 16 October 2013. The green ellipse highlights the vertical velocity dipole associated with the potential temperature discontinuity

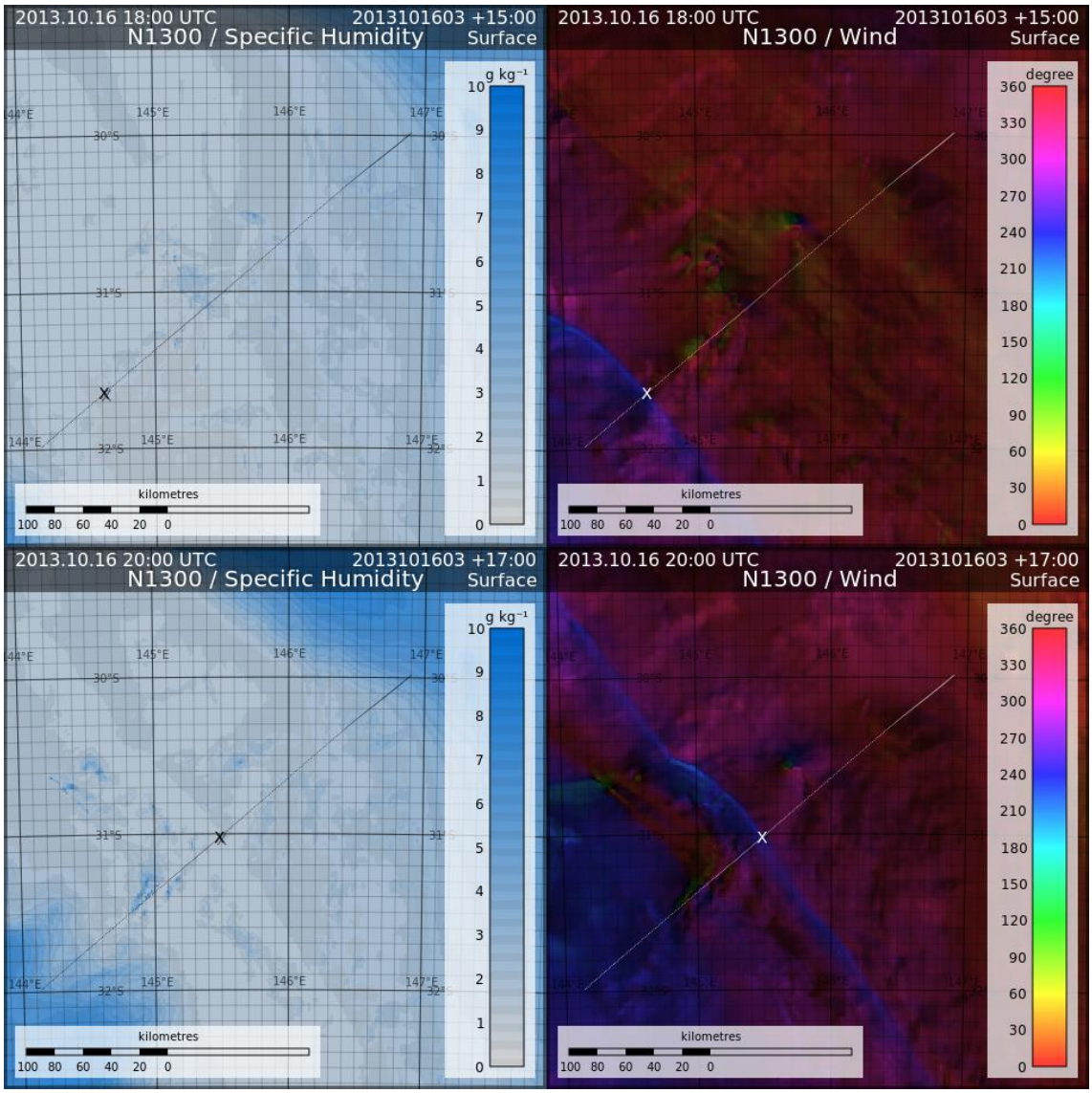

Figure 37. Montage of NWP model simulated 2-metre specific humidity and 10-m wind from 1800 UTC 16 October 2013 to 2000 UTC 16 October 2013. The wind direction is hue coded as per the legend, with brightness varying linearly with wind speed. The dotted line is the track of a marker (X) that moves northeastwards with the wind direction discontinuity. The domain of these charts is depicted by the box over the northwestern region of Figure 33.

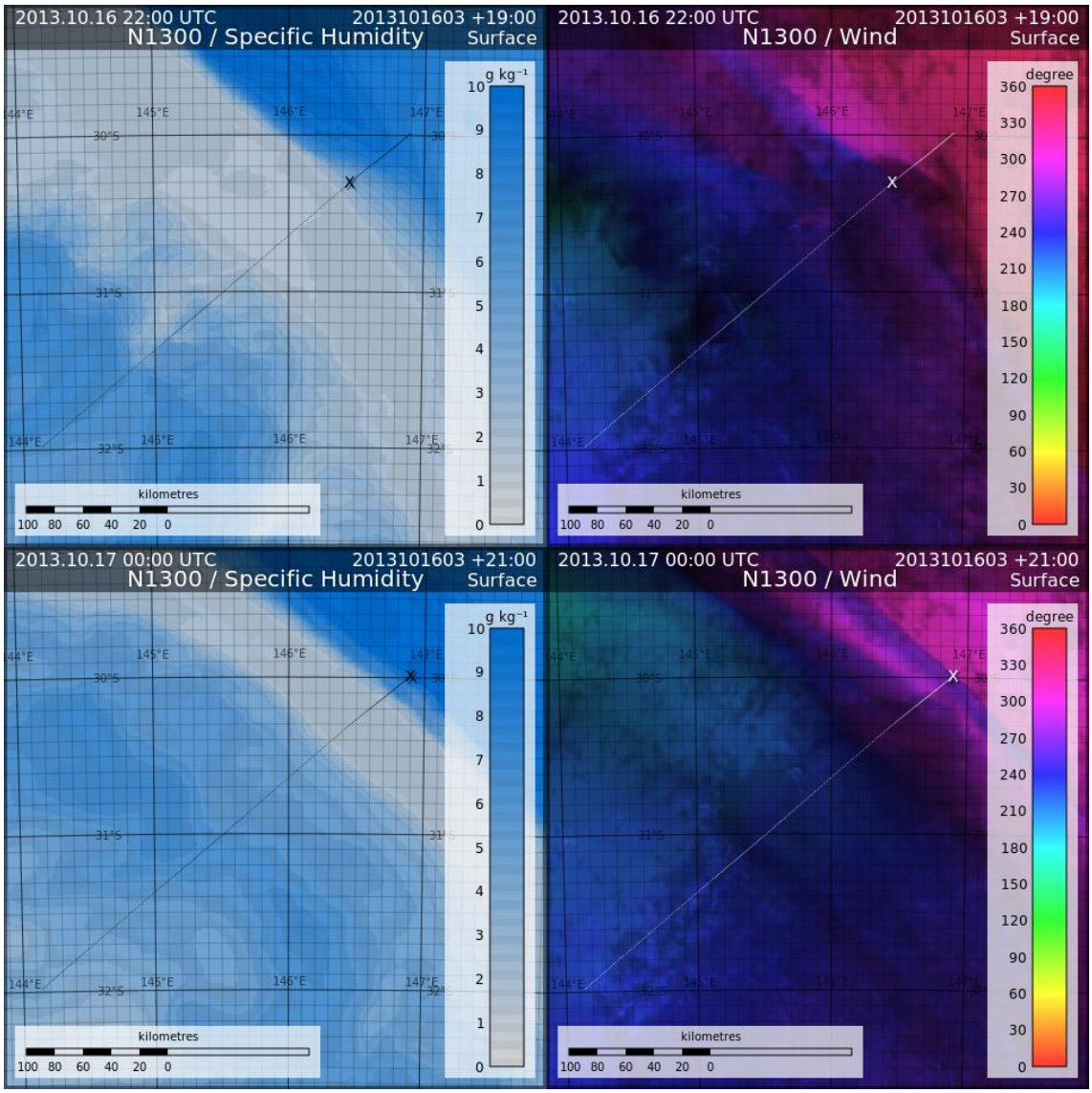

Figure 38. As in Figure 37 but for 2200 UTC 16 October 2013 and 0000 UTC 17 October 2013.

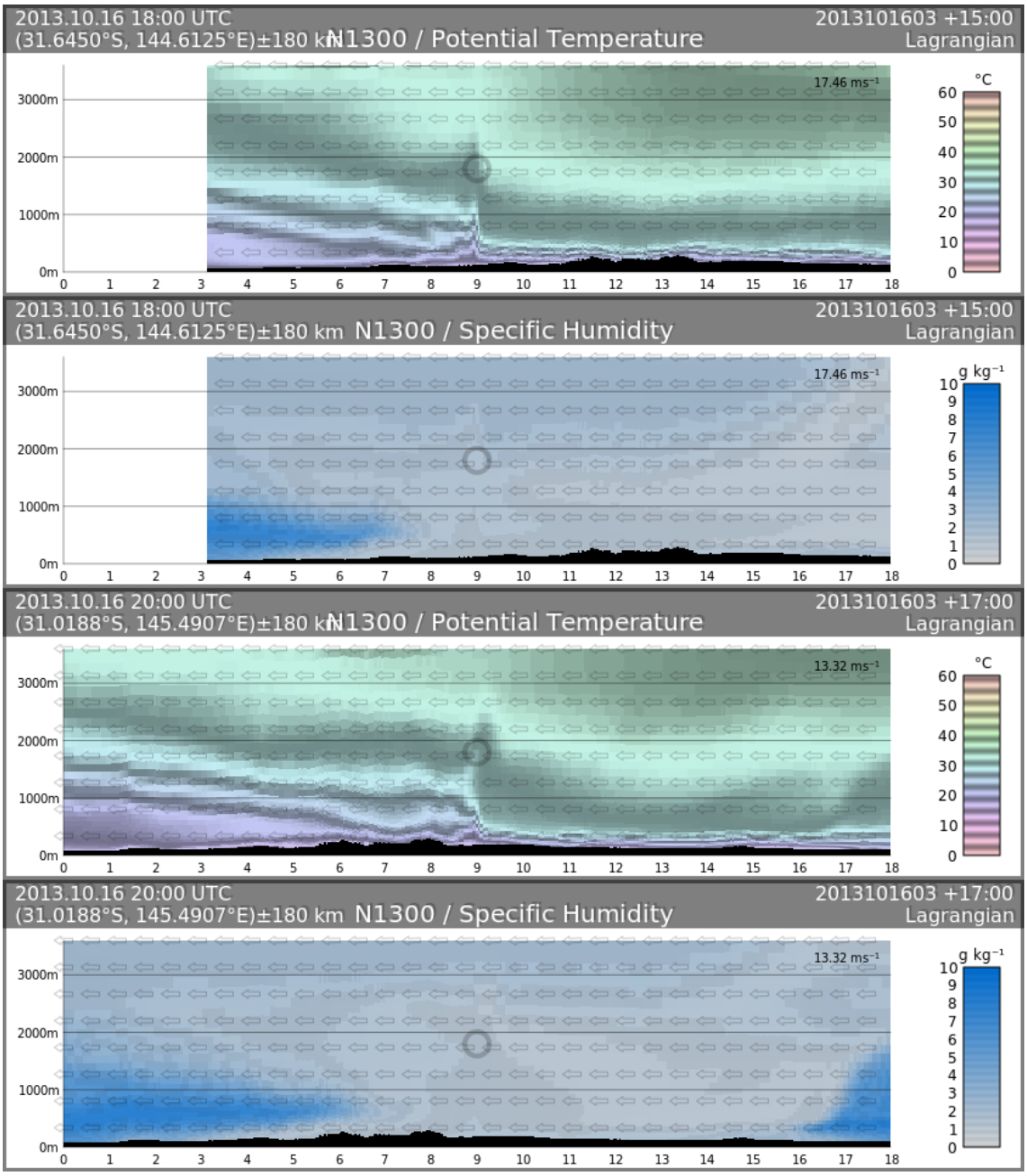

Figure 39. Montage of vertical cross sections of simulated potential temperature and specific humidity at 1800 UTC and 2000 UTC 16 October 2013 from the N1300 nest, centred at the marker X in Figure 37 aligning with the track and spanning 360 km in length. The numbers 0 to 18 in the horizontal axis are equidistant position markers 20 km apart. The faint circle corresponds to the location of X, moving at a speed indicated by the figure marked in the top right hand corner of the chart. Faint arrows indicate the 3-dimensional wind direction, relative to the motion of X, projected onto the vertical cross sectional plane.

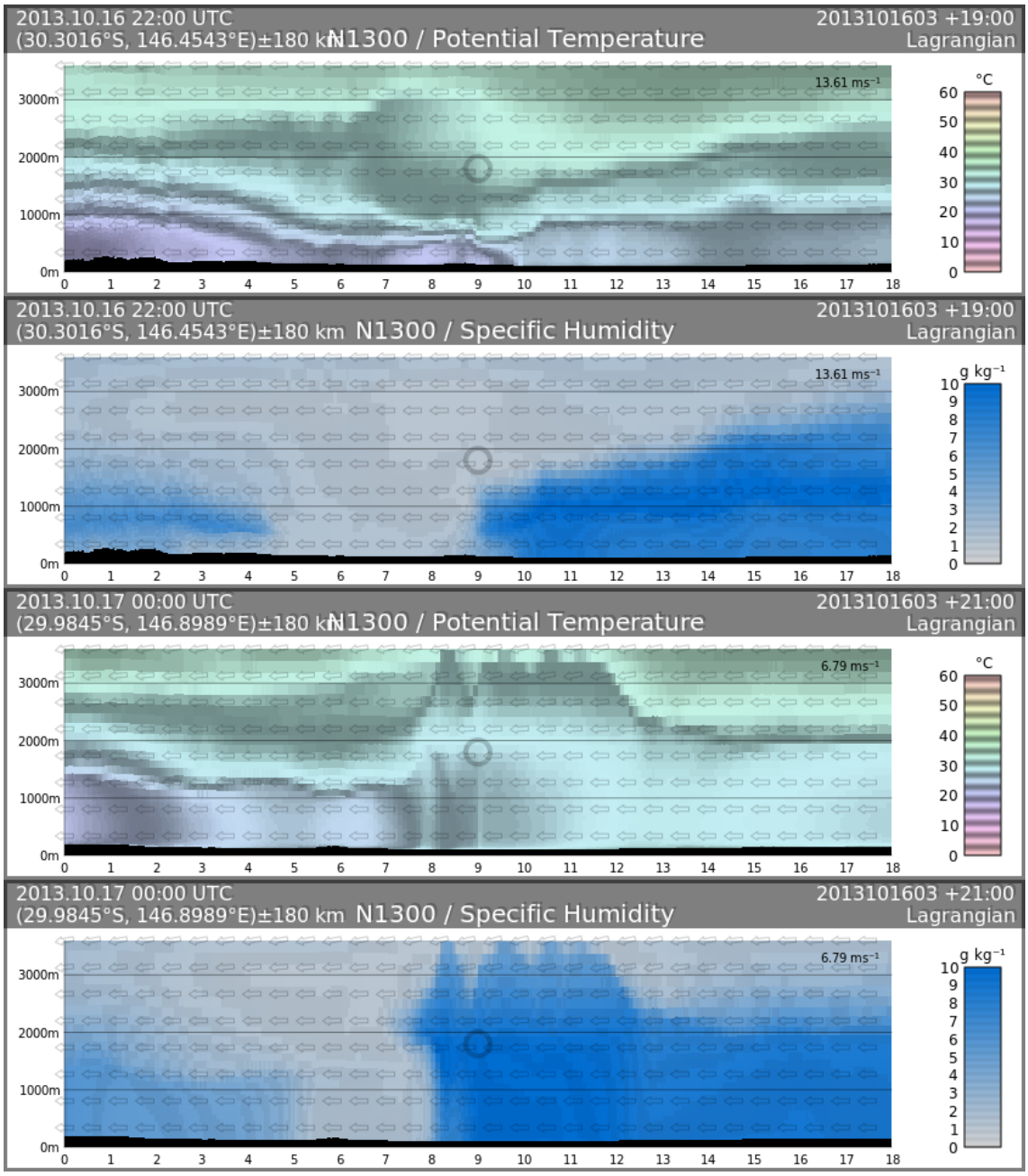

Figure 40. As in Figure 39 but for 2200 UTC 16 October 2013 to 0000 UTC 17 October 2013.

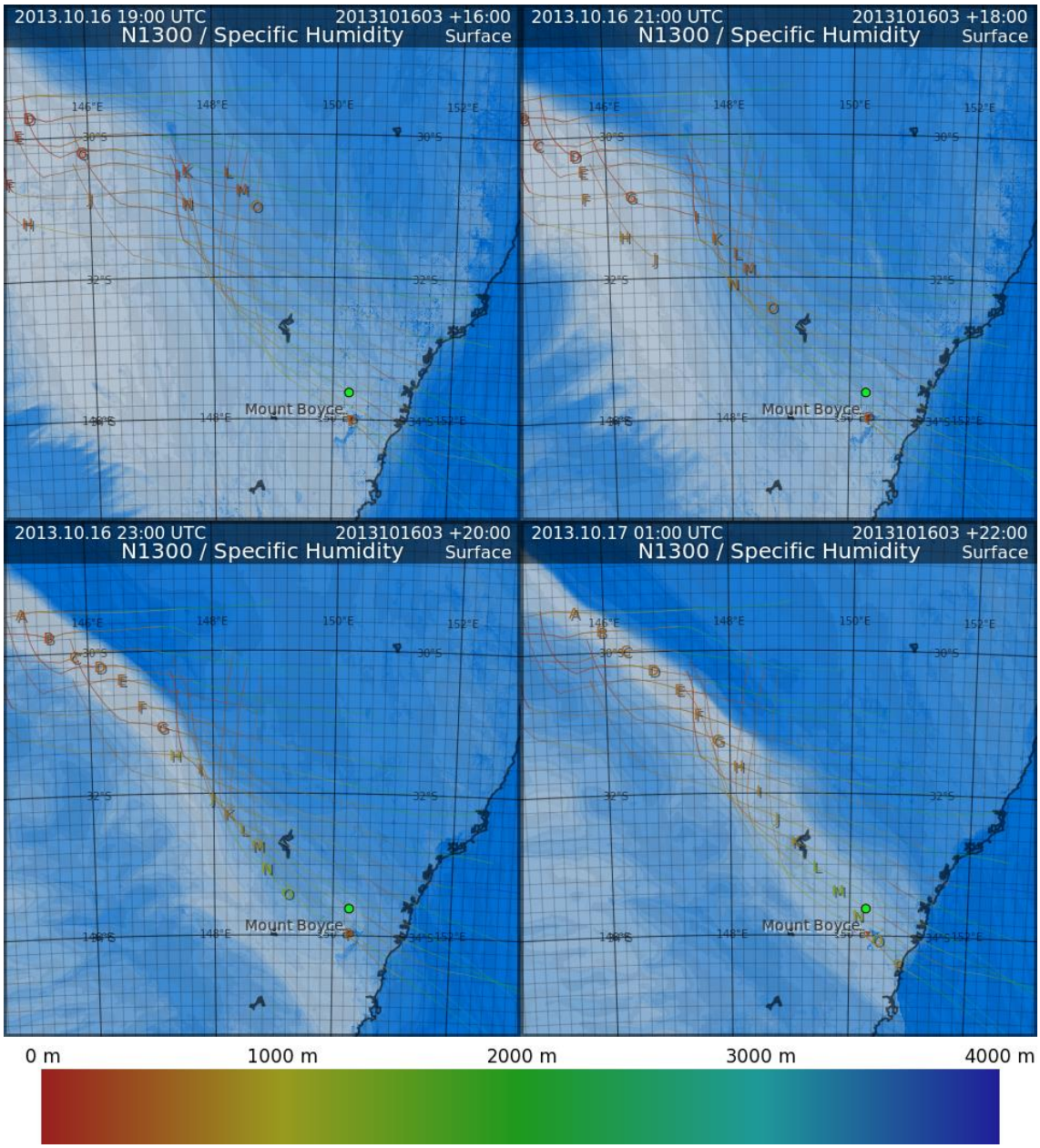

Figure 41. Montage of NWP model simulated 2-metre specific humidity every 2 hours from 1900 UTC 16 October 2013 to 0100 UTC 17 October 2013 from the N1300 nest. The 16 letters A to P depict parcels following trajectories integrated backward for 7 hours initialised at 0100 UTC 17 October 2013, 400m above ground level. Colour coding of specific humidity as in Figure 33. The letters are colour coded with the elevation of the parcel from mean sea level as in the colour legend at the bottom.

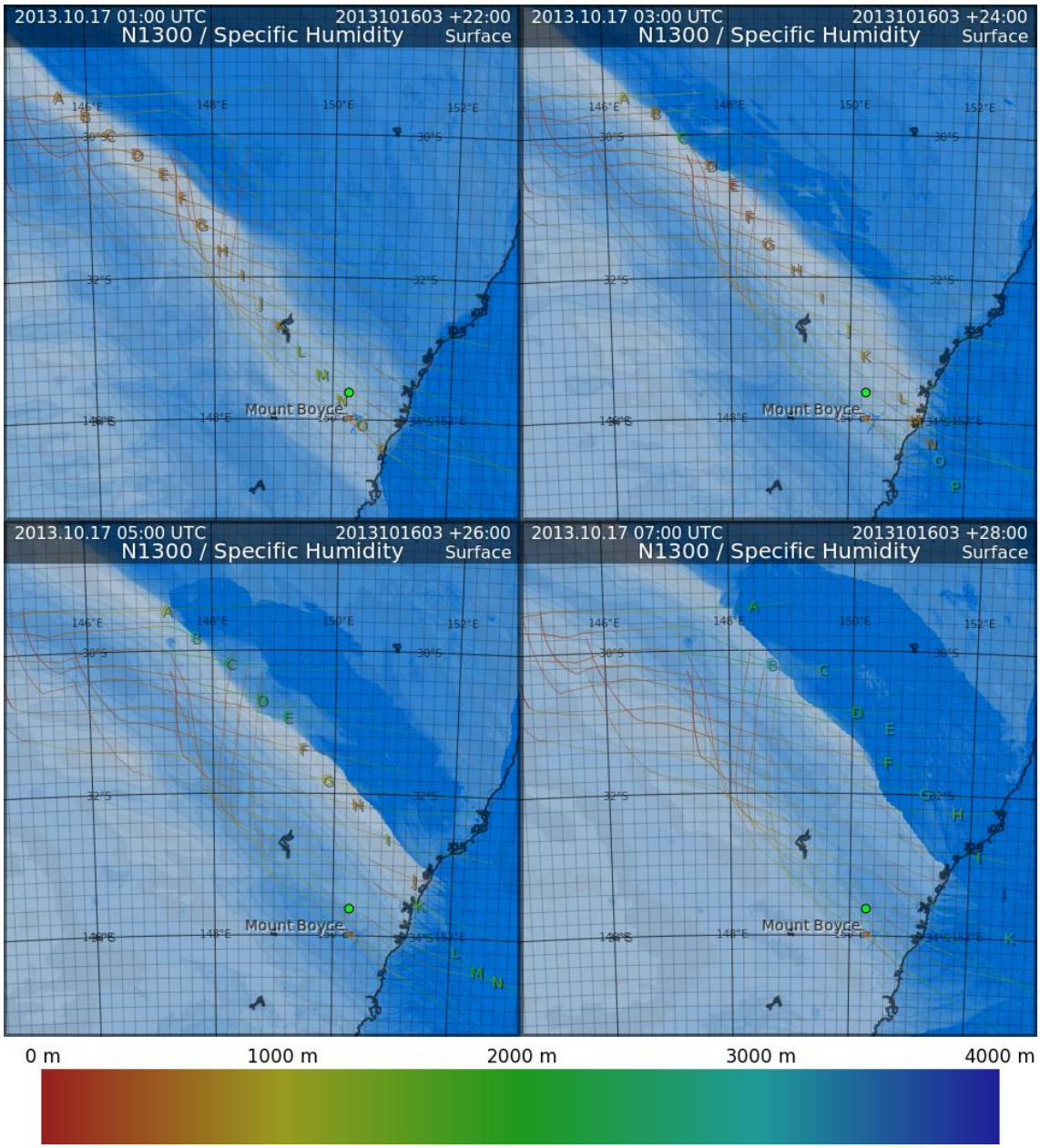

Figure 42. As in Figure 41 but from 0100 UTC to 0700 UTC 17 October 2013 with the alphabets following trajectories integrated forward for 7 hours initialised at 0100 UTC 17 October 2013.

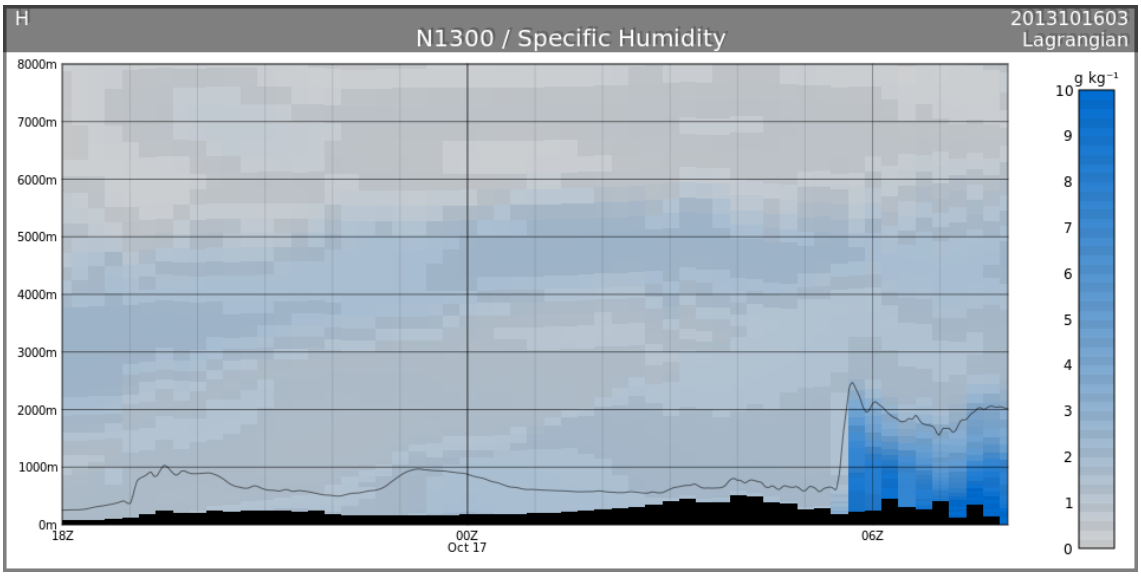

Figure 43. Time cross section of NWP model simulated specific humidity following parcel H in Figure 41 and Figure 42 from 1800 UTC 16 October 2013 to 0800 UTC 17 October 2013 from the N1300 nest. The thin black line depicts the height of parcel H.

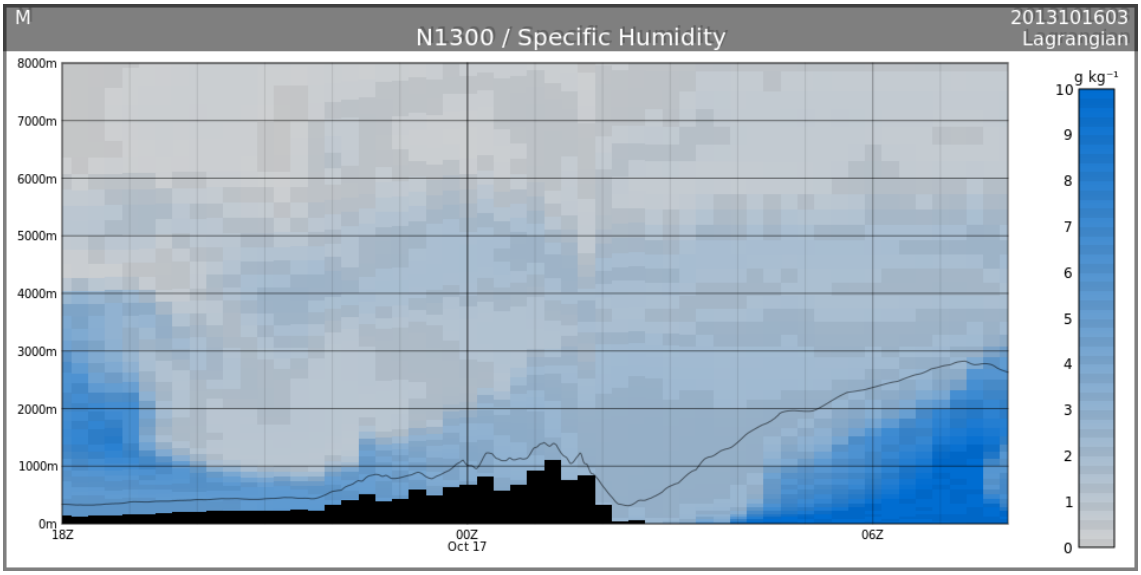

Figure 44. As in Figure 43 but for parcel M in Figures 22 and 23.

DISCUSSION AND CONCLUSIONS

Analysis of the observations at Mount Boyce, a nearby AWS to the Blue Mountains Fires, revealed that the hot, dry and windy conditions are responsible for the severe fire weather conditions on 17 October 2013, leading to the rapid spread of the fires. With substantially below average rainfall in the several months leading up to October 2013, the dryness about the Blue Mountains area was approximately in the top 5 percentile, which laid down the foundation of a potentially significant fire hazard. On 17 October 2013, the daily maximum temperature of Mount Boyce was 22.5°C. Considering the elevation from mean sea level of the AWS site of 1080m, it was actually a rather hot day (82.2 percentile of all October days).

The strong to gale force winds on the day, highlighted by the observation of 28.3 m s^{-1} gust at Mount Boyce, exacerbated by the passage of a slot of very dry air during the afternoon of 17 October 2013, reaching a minimum of -7.6°C, turned out to have elevated the fire risk of the day from high to severe. The NWP simulation suggests that the winds were strengthened by the mountain waves excited by the topography in the form of enhanced downslope winds, and the dry slot moved across the Blue Mountains area coincidentally near the onset time of the increase of wind speed as observed at Mount Boyce. The vertical profile of the atmosphere at Mount Boyce during the afternoon indicated a 3 km column of unstable, dry air with very strong winds (about 30 m s^{-1}), were conducive to the formation of pyrocumulonimbus clouds, and the lofting and transport of fire brands to great distances downstream, which all contributed to the very rapid eastward spread of the State Mine Fire on the afternoon of 17 October 2013.

The formation of the dry slot, according to the simulation, was related to the development of an undular bore which formed upstream the night before, when the cool change slid into the shallow layer of cool air formed by nocturnal cooling. A "dry nose" was formed on the north-eastern periphery of the advancing moist, cool change. Upon collision with the moist air-mass from the north, the "dry nose" became a dry slot of air during the morning of 17 October. The dry slot was then maintained by simple advection and moved across the Blue Mountains area during the afternoon, before dissipating during the early evening when the dry air was lifted from the surface as it encountered the moist outflow of the convective activities further north.

The sparseness of the observational network makes it intrinsically hard to capture mesoscale features, like the ones presented in this paper. Fortunately, good quality, high resolution NWP model simulation data is available, which makes such analyses possible, although certain discrepancies between the observations and the simulation are noted.

PRACTICAL IMPLICATIONS

This fire event was very high impact, and the mid-October timing was well away from the usual seasonal peak in fire activity. We have identified the meteorological factors responsible, being the mountain waves increasing the surface wind speed, and the dry slot. It appears, based on this research and some of our earlier work, that mountain waves are an underappreciated factor

in unexpected fire behaviour. We conducted a major utilization activity, including a *Hazard Note* and media articles, to raise awareness of this issue.

SECONDARY EYEWALL FORMATION IN TROPICAL CYCLONES

This chapter is based on a draft manuscript prepared for the 2017 AFAC meeting, *Kepert, J.D., 2017: Secondary eyewall formation in tropical cyclones.*

SUMMARY

Roughly half of all intense tropical cyclones experience an eyewall replacement cycle. In these events, a new eyewall forms concentrically around the original one. This secondary eyewall develops its own wind maximum, and both the secondary eyewall and the wind maximum typically intensify and contract, whilst the original eyewall and wind maximum weaken and eventually dissipate. While the evolution of a storm with concentric eyewalls is reasonably well understood, the mechanism or mechanisms by which the outer eyewall forms remain elusive. Understanding secondary eyewall formation is an important problem, for the subsequent eyewall replacement cycle can significantly affect the intensity of the storm, and the formation process and replacement cycle are usually associated with a major expansion of the outer wind field. Both these factors significantly affect the cyclone's impact.

We investigate a high resolution simulation of an eyewall replacement cycle. Boundary layer convergence due to friction substantially influences the evolution of the convection, and we present evidence for a positive feedback involving convection, vorticity and frictional convergence that governs the subsequent evolution of the system. In this feedback, frictional convergence strengthens the convection, stretching of vortex tubes in the buoyant updrafts increases the vorticity, and the vorticity structure of the storm determines the strength and location of the frictional updraft.

Changes in the structure and intensity of tropical cyclones cause difficulties for their management, especially if these changes occur in the last day or two before landfall. Our improved knowledge of these processes will lead to better forecasts and mitigation.

INTRODUCTION

In literature, "the eye of the storm" is an apt description for a region of peace and calm, around which tumult and turmoil reign (White, 1973). The analogy is to a tropical cyclone, where the eye, characterised by light winds, little cloud and little or no precipitation, is surrounded by the towering clouds of the eyewall. These eyewall clouds slope outwards from the centre of the storm with height, giving the appearance of a giant amphitheatre. The strongest winds are close to the surface immediately below these clouds, and they generate substantial amounts of rain. Often, the formation of a symmetric eye signifies that the cyclone is entering an intense and destructive phase. Truly, the literary analogy is apt.

About half of all intense tropical cyclones experience an eyewall replacement cycle (ERC). In an ERC, a secondary eyewall forms, concentric about the

existing eyewall. Over the next day or so, the new eyewall intensifies and contracts, while the initial eyewall weakens and eventually disappears. During eyewall replacement, the cyclone's intensity is steady or weakens, but intensification typically resumes once the replacement of the initial eyewall is complete. Notable examples of Australian tropical cyclones with an ERC include cyclones Vance (1999), Larry (2006) and Yasi (2011).

Figure 45 illustrates a typical sequence, using satellite images from a variety of passive microwave sensors in the 85 – 91 GHz band on polar-orbiting satellites. These frequencies can see through the dense cirrus overcast that normally obscures our view of the inner workings of tropical cyclones, and hence reveal the rainband and eyewall structure. At the start of the sequence, the primary eyewall is the red circle near the centre, surrounded by the deep convection of the spiral rainbands. Over the next 12 hours, the rainbands become more symmetric and organise into an outer eyewall by 22:43 on 22 August (panel d). The outer eyewall continues to become more symmetric, while the inner one weakens and decays, with the last vestige visible at 12:47 on 28 August (panel i).

The fundamental dynamics of the tropical cyclone eyewall replacement cycle (ERC), after the outer eyewall has formed, have been understood for over three decades (Shapiro and Willoughby 1982; Willoughby et al. 1982). In contrast, the cause of the initial formation of the outer eyewall has proved to be more elusive. Numerous theories have been proposed (see the reviews by Rozoff et al. 2012; Wu et al. 2012) but a consensus has not been achieved. More recently, attention has focussed on the possible role of the boundary layer in secondary eyewall formation (SEF) (Huang et al. 2012; Kepert 2013; Abarca and Montgomery 2013). Therefore, it is of interest to diagnose the boundary-layer processes occurring during SEF and the subsequent evolution of the eyewalls. This report describes our analysis of a SEF/ERC simulated by a high-resolution WRF simulation of a hurricane. An earlier report (Kepert and Nolan 2014) focussed on the boundary layer dynamics. Here we consider the effects of heating and the cloud processes also.

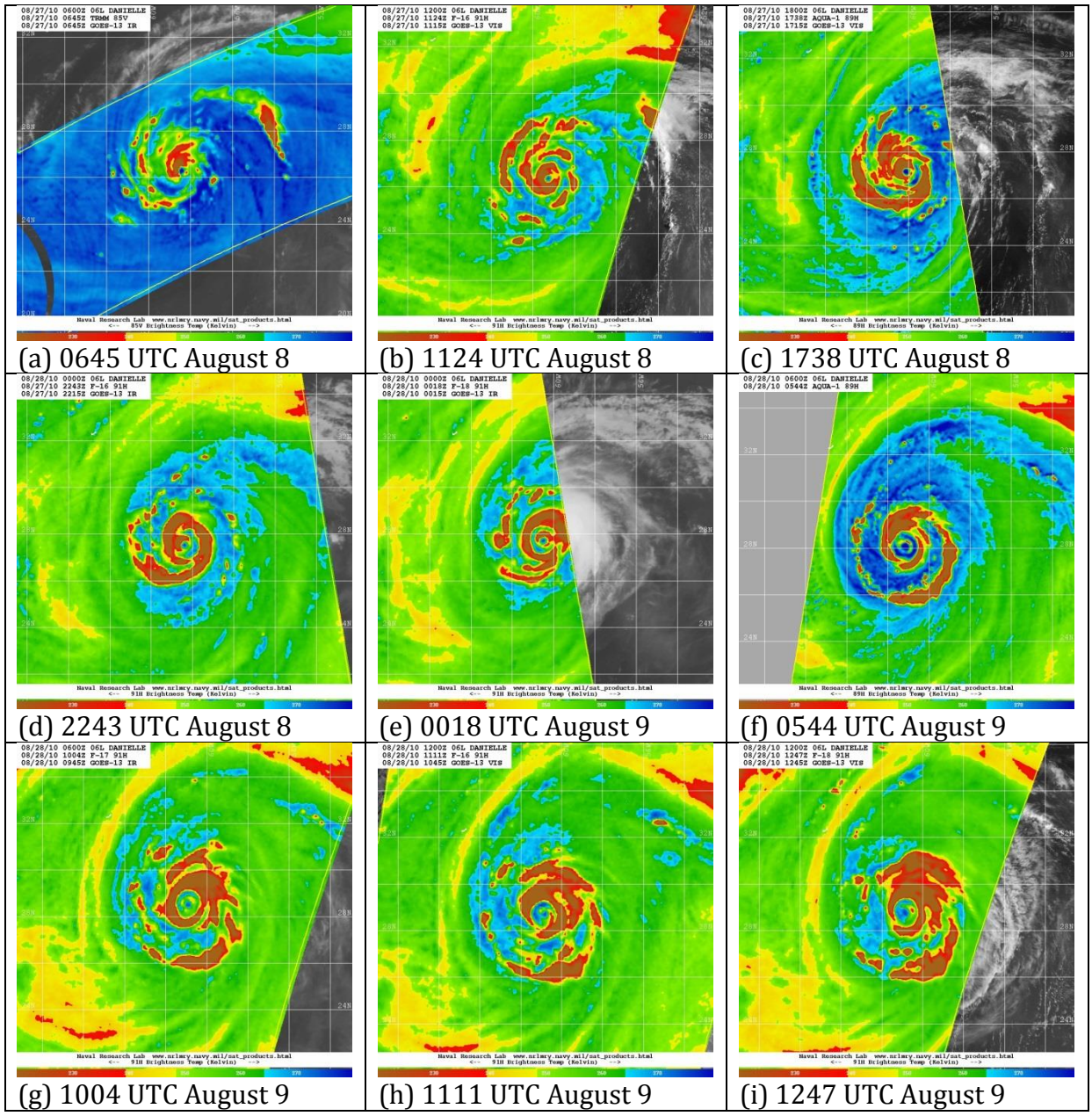

Figure 45: Passive microwave imagery in the 85 – 91 GHz band from TRMM, DMSP and Aqua satellites, for Hurricane Danielle of 2010. Red and brown shading indicate deep convection. Times and dates are indicated beneath each image. Note that the time interval between images varies. Data courtesy of the US Naval Research Laboratories.

THE SIMULATION

We use a WRF simulation of a TC that includes a SEF and ERC, prepared as a nature run for data assimilation experiments and described by Nolan et al. (2013). That simulation nested the WRF model (Skamarock et al 2008) from 27km down to 1 km and covered the full life of the hurricane, although we will focus attention on the 48-h period beginning at 0000 UTC 3 August. Details of the simulation, including the choice of the nesting and initial fields, and the model setup including the physical parameterizations, are given by Nolan et al. (2013).

Figure 46 shows the evolution of relevant fields, azimuthally averaged, from the simulation. Panel (a) shows the latent heat release, which is an indication of the occurrence of deep convection. The initial contraction and intensification of the primary eyewall is apparent, as is the formation and subsequent contraction and intensification of the secondary eyewall, indicated by the magenta curve. Panel (b) shows the similar evolution of the near-surface gradient wind, with the formation of the primary wind maximum and its replacement by the secondary one readily apparent. Note also the general outwards expansion of the wind field during the process. Panels (c) and (d) show the convective available potential energy (CAPE), a measure of the favourability of the atmosphere for convective cloud formation, and the vorticity[1] of the gradient wind, respectively, and will be discussed later, as will the green curve.

[1] In an axisymmetric vortex, the vorticity is defined as $\zeta = v/r + \partial v/\partial r$, where v is the azimuthal wind and r is radius. More generally, it is defined as the vector curl of the wind velocity. Given the crucial importance of vorticity to understanding these processes, it is appropriate to give a physical interpretation. Imagine a paddle wheel suspended in the air, with its axis vertical, moving with the wind. It may rotate, for instance if the flow is curved (curvature vorticity), or if the wind is stronger on one side of the paddle wheel than the other (shear vorticity). If observed from a fixed coordinate system, rather than the earth, it also rotates because the earth is rotating (planetary vorticity, accounted for by the Coriolis parameter f), and the absolute vorticity is the sum of the earth-relative and planetary vorticities. In tropical cyclones, the curvature and shear vorticity are of opposite sign outside of the eyewall, and these two terms cancel to some degree, but the net vorticity is mostly of the same sign as f; that is, cyclonic.

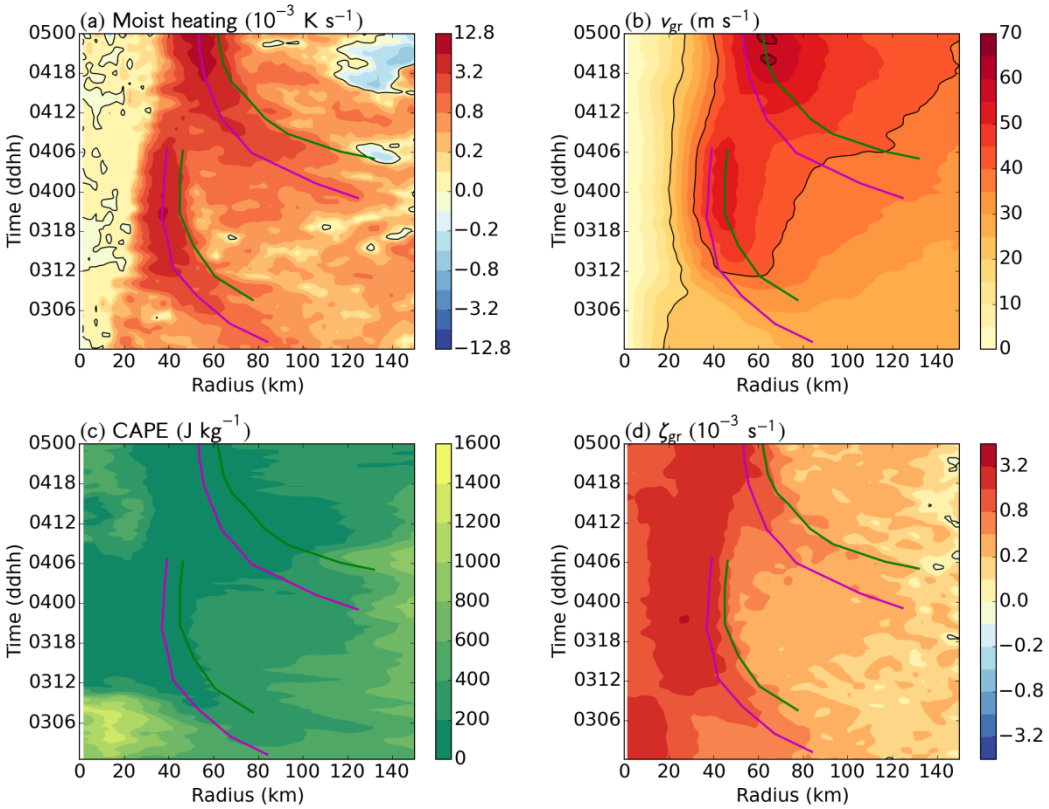

Figure 46: Time-radius diagrams of (a) the moist heating rate, averaged over 1-5 km height; (b) the gradient wind speed at 2-km height; (c) the surface-based CAPE; and (d) the vorticity of the gradient wind. All fields are azimuthally averaged. The magenta curves indicates the approximate location of the Two eyewallS, as determined from the moist heating. The green curves indicate the approximate location of the radiI of maximum negative radial vorticity gradient.

ANALYSIS TOOLS

The tropical cyclone flow can be divided into two components: the primary circulation, which is the rotational flow, and the secondary circulation, which consists of inflow mainly near the earth's surface, ascent mainly near the cyclone centre, and outflow mainly in the upper troposphere. The secondary circulation is often described as "in, up and out". It is forced by two main mechanisms: surface friction causing the near-surface flow to spiral inwards rather than being purely circular, and latent heat release in the clouds, particularly in and around the eyewall, which causes buoyant ascent. Mathematically, we adopt the convention that a radial flow component directed towards the centre of the storm (i.e. inflow) has a negative sign, whereas outflow is positive.

The frictional component of the secondary circulation, to a first order approximation, does not intensify the cyclone or change its structure, because the inwards advection of absolute angular momentum[2] nearly balances its destruction by surface friction (Kepert 2013). The heating component, in contrast, can intensify the cyclone since its lower branch advects absolute angular momentum inwards, spinning up the storm by the "ice-skater effect".

We assess the heating-induced component by the Sawyer-Eliassen equation, and the frictional component using a diagnostic boundary-layer model.

The Sawyer-Eliassen equation

The Sawyer-Eliassen equation (SEeq) diagnoses the secondary circulation due to latent heat release and other diabatic heating sources. It can also diagnose the effect of momentum sources and sinks, but may be less accurate for boundary layer friction due to the violation of a key assumption within the boundary layer.

We use the form of the SEeq given by Pendergrass and Willoughby (2009), discretised on a uniform grid with 75 grid points in radius, from 4 to 300 km, and 39 in height, from 0 to 19.5 km. The boundary conditions are that the flow perpendicular to the inner, upper and lower boundaries is zero, and that the flow is purely horizontal at r = 300 km. The discretised equation is solved directly using QR decomposition, which is feasible on modern computers with a problem of this size. Although not especially efficient, direct solution avoids the problem of potential nonconvergence of iterative methods should the SEeq be slightly non-elliptic, as sometimes happens in the upper-level outflow at large radius.

In this application, the inputs to the SE equation describing the structure of the storm and the heating are taken to be the azimuthal means, calculated directly from the WRF simulation output. Heating is taken to be the sum of latent heat exchanges and radiation.

[2] Absolute angular momentum is similar to the familiar concept of angular momentum, but is calculated from a fixed frame of reference and therefore takes into account the earth's rotation. If r is the radius and v the azimuthal wind, then the absolute angular momentum is $M_a = rv + 0.5fr^2$, where the Coriolis parameter f is the local vertical component of the earth's rotation.

The boundary-layer diagnostic model

The boundary-layer diagnostic model has been described by Kepert and Wang (2001), and Kepert (2012, 2017). It solves the equations of fluid motion, with high-quality parameterisations of friction and turbulence, for a prescribed fixed pressure field representative of a tropical cyclone. It is run forward in time to a steady state, and the resulting flow represents the equilibrium boundary-layer flow given that pressure forcing. One day of model time usually gives a sufficiently steady state. For convenience, the pressure field is specified in terms of the gradient wind,

$$\frac{v^2}{r} + fv = -\frac{1}{\rho}\frac{\partial p}{\partial r},$$

where v is the azimuthal wind, r is radius, f is the Coriolis parameter, ρ is density and p is pressure.

In contrast to the SEeq, where the domain includes the full depth of the troposphere, here the domain is only 2.25 km deep, sufficient to contain the boundary layer.

As with the SE equation, the necessary input to this model of the gradient wind is calculated from the azimuthal mean of the WRF simulation output, at hourly intervals. The boundary-layer models turbulence and friction parameterisations were configured to be reasonably consistent with those in WRF.

The boundary-layer model has been shown to be able to accurately reproduce the distribution of vertical motion in tropical cyclones when used in this way (Kepert and Nolan 2014, Zhang et al 2017).

DYNAMICS OF THE EYEWALL REPLACEMENT CYCLE

Does frictional convergence influence the convection?

Figure 47a shows the azimuthal-mean vertical velocity at 1-km height from the WRF simulation. The evolution of the two eyewalls is clear, and closely follows that of the latent heat release in Figure 46a, as is usual in tropical cyclones. Figure 47b shows the diagnosed frictional updraft from the boundary-layer model, which clearly reflects a very similar pattern. There are two significant differences: the updraft in the boundary-layer model is consistently weaker, and located at slightly larger radius. We will show shortly that the difference in strength of the updraft is due to the absence of buoyant convection in the boundary-layer model.

To confirm that boundary-layer frictional convergence is the cause of the convection, we have to eliminate other possible causes, in particular thermodynamic factors. Convective available potential energy (CAPE), shown in Figure 46c, is a widely-used measure of the favourability of the atmosphere for convection, with higher numbers being more favourable. The values shown there are somewhat, but not strongly, favourable. There are no features in the CAPE field which would promote convection at the time and location of the secondary eyewall. Indeed, the CAPE at this time is amongst the lowest in the figure, and decreases as the eyewall strengthens. This decrease is due to two reasons (not shown): cold downdrafts from convection cooling and drying the lower troposphere, and the broadening of the upper warm core reducing the equilibrium level for deep convection.

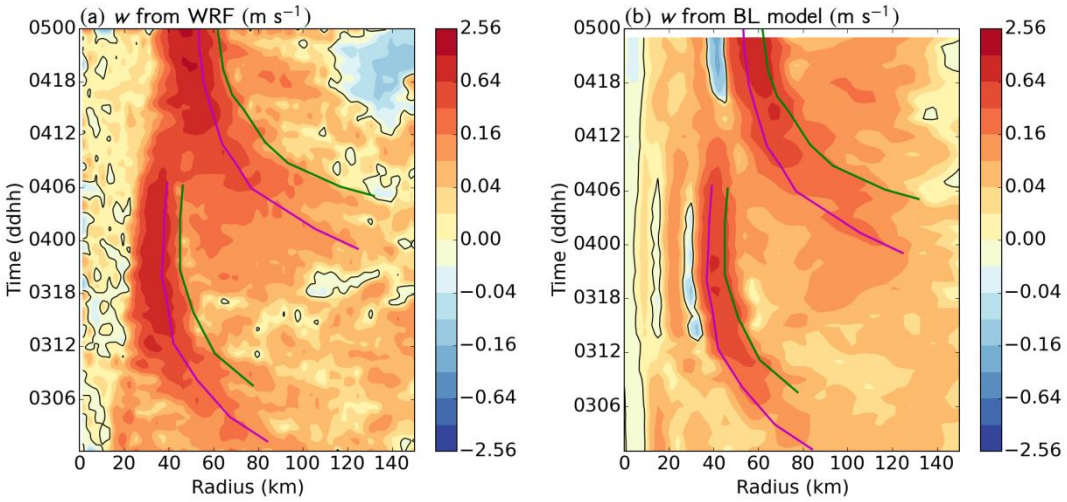

Figure 47: Time-radius plots of the azimuthal-mean vertical velocity at 1-km height, from (a) the WRF simulation and (b) the diagnostic boundary-layer model.

How does the convection alter the cyclone structure and intensity?

The modelled secondary circulation at four key times before and during the ERC are shown in Figure 48, together with the corresponding diagnosed fields from a preliminary calculation with the SEeq. There is generally quite good agreement. One systematic differences is that the diagnosed main updrafts are often too weak in the lowest 2 km of the atmosphere, likely due to the absence of friction in this calculation. Indeed, the updraft in this region appears to be forced by both latent heat release and friction, since both diagnostic methods underestimate it. The diagnostic calculation also has inflow around 3 km height and 80 km radius, whereas WRF has outflow. Again, this may be due to the absence of friction. There are also a number of technical issues still to be resolved with the SEeq calculation, whose contribution is presently unknown – we note that this is a preliminary calculation.

Nevertheless, there is quite good agreement with the WRF simulation. We may therefore appeal to earlier studies with the SEeq (Shapiro and Willoughby 1982, Willoughby et al 1982) to note that the expected storm evolution from this pattern would be for the outer wind maximum to intensify and contract, qualitatively consistent with the evolution in Figure 46b. Future work will examine the extent to which quantitative agreement is obtained.

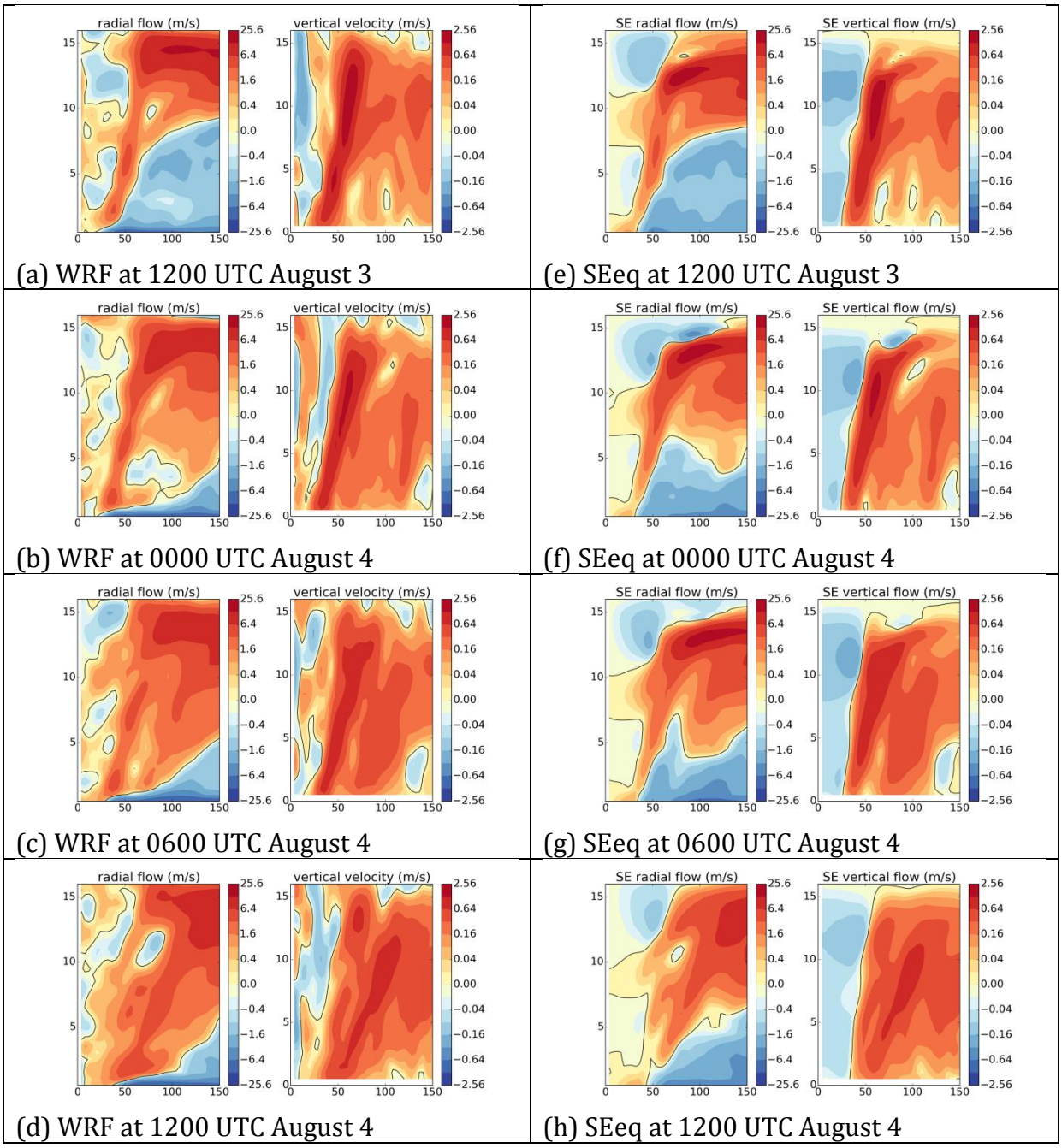

Figure 48: Secondary circulation during the ERC and SEF. Panels (a – d) show the azimuthal-mean radial wind (left, positive is outwards) and vertical wind (right, positive is upwards) from the WRF simulation at times as indicated. Panels (e – h) show the corresponding diagnosed secondary circulation using the SEeq.

How does the cyclone's pressure field affect the frictional convergence?

We have seen above that the diagnosed frictional convergence determines the location and intensity of the convective heating. The only data passed from WRF to the diagnostic model in this calculation is the pressure field, in the form of the gradient wind. The question, then, is what characteristic of the pressure field leads to localised updrafts outside of the primary eyewall?

In Figure 47, we saw that the diagnostic BL model reproduces the location and relative strength of the two eyewall updrafts reasonably accurately, although underpredicts the strength because in the WRF simulation that is enhanced by the additional forcing from buoyant convection. It is also apparent in this figure that the changes in the gradient wind are spatially smoother than the vertical velocity response, and are relatively subtle. Pressure is the radial integral of the gradient wind equation, so the changes in pressure must be even smoother than for gradient wind[3]. Nevertheless, these subtle changes must be responsible for the changes in the frictional forcing of the updraft, because they are the only information passed to the boundary-layer model. In other words, we know **that** the pressure field affects the frictional convergence, and we need to determine **how**.

Kepert (2001) developed a simplified diagnostic tropical cyclone boundary layer model. Compared to the model used here, the simplifications included a linearization, and adoption of less realistic representations of turbulent diffusion and the air-sea momentum transfer. While calculations with this model are expected to be less accurate than from the full diagnostic model, they offer the great benefit that an analytic solution is available. That is, we can directly examine the equations to understand how the vertical velocity relates to the pressure (or gradient wind) structure.

Kepert (2013) used that model to show that near the eyewall(s) of typical tropical cyclones, the updraft is approximately proportional to the radial gradient of the vorticity of the gradient wind, multiplied by the drag the wind exerts on the sea surface (approximately proportional to the square of the wind speed), divided by the square of the absolute vorticity. This equation suggests that we can expect to find enhanced updrafts where there is a locally strong negative radial vorticity gradient. Such gradients are especially effective if they occur where the vorticity is relatively low, because of the division by the square of the vorticity. The surface friction has a lesser effect on locating the updraft, because it varies relatively slowly with radius.

DISCUSSION AND CONCLUSIONS

Figure 46b,d and Figure 47a compare the joint evolution of the vorticity of the gradient wind, the frictional updraft, and the moist heating. These figures show the mutual contraction of the region of strong vorticity gradient and the region of strong convective latent heat release. Indeed, a similar relationship is also apparent earlier in the cyclone's life, during the initial contraction and

[3] Differentiation acts as a high-pass filter, emphasising the small scales, as can be easily shown using the Fourier transform.

intensification of the primary eyewall between 0000UTC and 1200UTC on August 3.

Clearly, these features are strongly correlated. However, correlation is not causation. Two phenomena, A and B may be correlated may occur for several reasons: A causes B, B causes A, or that both are caused by some third factor C.

In this chapter, we have provided additional information that does allow us to attribute cause. In particular, using the diagnosed frictional convergence, which depends only on the cyclone's pressure field, we have shown that the distribution of vertical velocity at the top of the boundary layer is determined largely by frictional processes, although friction is insufficient to explain the full magnitude of the ascent. By comparing the evolution of the diagnosed frictional convergence to that of the convective latent heat release, together with the absence of any features sufficient to explain the localisation of the convection in the stability or moisture fields, we show that the frictional updraft is largely determining the location and strength of the convection. Calculating that part of the secondary circulation induced by heating, using the Sawyer-Eliassen equation largely accounts for that part of the low-level updraft missing from the frictional calculation. The evolution of the vortex structure explained by advection of absolute angular momentum by this secondary circulation is largely consistent with the evolution of the cyclone; that is, it leads to changes in the gradient wind that are similar to those in the WRF simulation. Most importantly, these include an inwards migration and strengthening of the vorticity features that we have theoretically linked to the evolving frictional updraft.

To summarise, we have confirmed that the positive feedback mechanism hypothesised by Kepert (2013) and further discussed by Kepert and Nolan (2014) and Kepert (2017) is indeed operating in this case. Here, vorticity-induced boundary-layer convergence acts to promote convection, provided that the stability and moisture are also favourable. Vortex-stretching in convective updrafts increases the local vorticity. We have analysed the combined, cyclone-scale, effect of many individual clouds by applying their combined heating to the Sawyer-Eliassen equation, but analyses at the cloud scale (not shown) similarly show that convective updrafts are acting to increase the vorticity beneath the developing secondary eyewall. These vorticity changes in turn further strengthen the frictional updraft. There is a further important subtlety in all of this, in that the relative location of the various processes is important for the precise details of the interaction, particularly the initial rapid contraction of the outer eyewall, followed later by slower contraction and intensification. These can be largely explained as a contribution of nonlinearity in the boundary layer, as detailed in Kepert (2017).

PRACTICAL IMPLICATIONS

Forecasting ERCs is challenging, because it is clear from the work described here that the changes in the early stages are quite subtle, and therefore difficult to detect. This is especially true in the harsh environment of tropical cyclones, where observations are difficult to take. Modelling ERCs is likewise

challenging, for this work implies that the interaction between friction, clouds and pressure in the cyclone must be represented with sufficient fidelity. Nevertheless, the success of the simulation used here and others shows that that fidelity has been achieved in current NWP systems.

The initialization of such simulations is challenging, especially since the early signs of an ERC are subtle. Small errors in the initial pressure field could completely remove the local vorticity perturbation and hence the frictional updraft, or add a spurious one. The necessary precision in the initialization will be beyond the reach of our observing and data assimilation systems, at least in the absence of aircraft reconnaissance, for some time. Ensemble prediction methods provide the only presently viable means of dealing with this uncertainty.

In spite of these considerable difficulties, forecasting ERCs is important. They represent a substantial additional difficulty for intensity forecasting, because of their large impact on the intensity evolution of the storm. They also strongly affect the ocean response. A substantial import of vorticity to the storm in the region of the developing outer eyewall seems to be an inherent part of the ERC process, and this import of vorticity explains the wind field expansion. The wind field expansion affects not just the width of the damage swath, but also the timing and duration of damaging winds. It also profoundly increases the ocean hazard, because applying strong winds to a larger area of the ocean's surface greatly increases the severity and extent of storm surge, damaging waves and coastal erosion. With the high concentration of vulnerable populations and infrastructure near the coast in Australia, improving our ability to predict ERC will clearly help mitigate tropical cyclone impacts.

SUMMARY

The project has studied a wide range of hazardous meteorological phenomena, hazardous either on their own or in conjunction with bushfires. We have used state-of-the-art high resolution modelling for this purpose, including ensemble modelling and large-eddy simulations.

We have studied long-range ember transport and found that turbulence within the bushfire plume is an important factor, roughly doubling the maximum distance that embers can be carried and also substantially increasing the spread of the landing distribution. The landing distribution has substantial cross-wind spread in light winds, but little in strong winds. We will be looking to build these findings into a computationally cheap parametrization of the underlying processes in the next phase of the project, for use in operational fire simulators.

We studied the formation of pyrocumulus clouds in two frameworks, one involving detailed simulation and the other a consideration of the underlying thermodynamics. These have shown that, most of the time, the moisture from the combustion process plays a negligible role in the formation of pyrocumulus. We have also identified the rare situations in which this is not so. This outcome is most encouraging, for it shows that forecasting methods for pyrocumulus can mostly ignore the combustion moisture, which is an exceedingly difficult parameter to quantify. We plan to incorporate this new knowledge into a prototype forecasting method in the next phase of the project.

We prepared a detailed case study of the east coast low of April 2015, which caused severe wind damage and flooding to the Hunter Valley and surrounding regions. This study was novel in its use of a 24-member high-resolution ensemble, rather than just a single simulation. The use of the ensemble facilitated certain diagnostics, as well as providing an excellent example of some of the advantages of ensemble prediction, including increased accuracy, probabilistic forecasts and reduced likelihood of missing significant developments.

Our second case study was the Blue Mountains fires of October 2013, focusing on the day of the most damaging fire activity, on which some 200 houses were lost. We identified two meteorological factors that likely contributed to this disaster, the development of mountain waves causing strong surface winds, and a dry slot of unusual origin. This is the third case we have studied with a clear mountain wave signature in the fire escalation, so we prepared a BNHCRC *Hazard Note* as well as other publications, to communicate these findings. By raising awareness, we hope that weather forecasters and fire fighters will be better able to recognize these events and respond appropriately.

Our final research activity for this project has been the analysis of a simulation of a tropical cyclone eyewall replacement cycle. We have developed a clear understanding of the processes involved, a complex and subtle interaction between clouds, surface convergence and the local rotation of the flow. The critical phase is the formation of the outer eyewall, and our new knowledge indicates the critical factors to being able to predict this. Eyewall replacement

cycles are important, for they affect several aspects of the tropical cyclone's impact, including the intensity, extent of damaging winds, and storm surge.

Numerous fctors are placing an increased burden on the ability of the Australian community to cope with natural hazards. These include greater exposure to risk, increased societal expectations, and climate change. Advanced modelling has come to be an indispensable tool in meteorology and oceanography for supporting forecasts, warnings and action, and is gaining a place in fire prediction also. Ensuring that the modelling reflects the best possible science, makes efficient use of expensive computer resources, and is appropriately communicated to and used by those responsible for mitigation, is a critical task. The results of this project, presented herein, play an important role in reaching these targets. In short, the knowledge gained is being used to help mitigate future disasters, and our future plans will take us even further down that path.

ACKNOWLEDGEMENTS

We thank the UK Met Office for the provision of their Large-Eddy Model code and Adrian Hill and Ben Devenish for their assistance in setting up model. We are also grateful to our colleagues at the Bureau of Meteorology for their assistance with the ACCESS system, and for their excellent work in implementing it. The analysis of the State Mine fire was greatly assisted by advice and data from the NSW Rural Fire Service, particularly Lawrence McCoy and Mel O'Halloran. This research was undertaken with the assistance of resources from the National Computational Infrastructure (NCI), which is supported by the Australian Government.

REFERENCES

Bednarczyk, C. N. and B. C. Ancell, 2015: Ensemble Sensitivity Analysis Applied to a Southern Plains Convective Event. Mon. Wea. Rev., 143, 230-249, doi:10.1175/MWR-D-13-00321.1.

Bowler, N. E., A. Arribas, K. R. Mylne, K. B. Robertson, and S. E. Beare, 2008: The MOGREPS short-range ensemble prediction system. Q. J. R. Meteorol. Soc., 134, 703-722, doi:10.1002/qj.234.

Brinkmann,W. A. R., 1974: Strong DownslopeWinds at Boulder, Colorado. Mon. Wea. Rev., 102, 592–602.

Brown, A. R., S. H. Derbyshire, and P. J. Mason, 1994: Large-eddy simulation of stable atmospheric boundary layers with a revised stochastic subgrid model. Quarterly Journal of the Royal Meteorological Society, 120, 1485–1512.

Ching, S.E., R.J.B. Fawcett, W. Thurston, K.J. Tory and J.D. Kepert, Mesoscale features related to the Blue Mountains Fires of 17 October 2013 revealed by high resolution numerical weather prediction modelling, submitted to *Monthly Weather Review*.

Cruz, M. G., A. L. Sullivan, J. S. Gould, N. C. Sims, A. J. Bannister, J. J. Hollis, and R. J. Hurley, 2012: Anatomy of a catastrophic wildfire: The Black Saturday Kilmore East fire in Victoria, Australia. *Forest Ecol. Manag.*, **284**, 269–285.

Cunningham, P. and M. J. Reeder, 2009: Severe convective storms initiated by intense wildfires: Numerical simulations of pyro-convection and pyro-tornadogenesis. *Geophys. Res. Lett.*, **36**, L12812, doi:10/1029/2009GLO39262.

Devenish, B. J., and J. M. Edwards, 2009: Large-eddy simulation of the plume 246 generated by the fire at the Buncefield oil depot in December 2005. Proceedings of the Royal Society A, 465, 397–419.

Devenish, B. J., G. G. Rooney, and D. J. Thomson, 2010: Large-eddy simulation of a buoyant plume in uniform and stably stratified environments. Journal of Fluid Mechanics, 652, 75–103.

Dowdy, A. J., G. A. Mills, and B. Timbal, 2013: Large-scale diagnostics of extratropical cyclogenesis in eastern Australia. Int. J. Climatol., 33, 2318-2327, doi:10.1002/joc.3599.

Durran, D. R., 1990: Mountain waves and downslope winds. Atmospheric Process over Complex Terrain., Meteor. Monogr., Vol. 23, Amer. Met. Soc., 59–83.

Durran, D. R., and J. B. Klemp, 1987: Another look at downslope winds. Part II: Nonlinear amplification beneath wave-overturning layers. J. Atmos. Sci., 44, 3402–3412.

Ellis, P. F. M., 2010: The effect of the aerodynamic behaviour of flakes of jarrah and karri bark on their potential as firebrands. *J. Roy. Soc. West. Aust.*, **93**, 21–27.

Finkele, K., G. A. Mills, G. Beard, and D. A. Jones, 2006: National gridded drought factors and comparison of two soil moisture deficit formulations used in

prediction of Forest Fire Danger Index in Australia. Australian Meteorological Magazine, 55, 183–197.

Fromm, M. D., A. Tupper, D. Rosenfeld, R. Servranckx and R. McRae, 2006: Violent pyro-convective storm devastates Australia's capital and pollutes the stratosphere. *Geophys. Res. Lett.*, **33**, L05815, doi:10.1029/2005FL025161.

Fromm, M. D.,R. H. D. McRae, J. J. Sharples and G. P. Kablick III, 2012: Pyrocumulonimbus pair in Wollemi and Blue Mountains National parks, 22 November 2006. *Aus. Met. Ocean J.*, **62**, 117—126.

Goens, D. W. and P. L. Andrews, 1998: Weather and fire behavior factors related to the 1990 Dude Fire near Payson, Arizona. In: Proceedings: 2nd symposium on fire and forest meteorology. Boston, MA: American Meteorological Society: 153-158.

Gray, M. E. B., J. Petch, S. H. Derbyshire, A. R. Brown, A. P. Lock, H. A. Swann, and P. R. A.Brown, 2001: Version 2.3 of the Met Office large eddy model: Part II. Scientific documentation. Turbulence and Diffusion Note 276, UK Met Office, Exeter, United Kingdom, 49 pp.

Griffiths, D., 1998: Improved Formulae for the McArthur Forest Fire Danger Meter. Meteorological Note 214, Bureau of Meteorology.

Hakim, G. J. and R. D. Torn, 2008: Ensemble Synoptic Analysis. Meteorol. Monogr., 33, 147-162, doi:10.1175/0065-9401-33.55.147.

Hall J., P. F. Ellis, G. J. Cary, G. Bishop and A. Sullivan, 2015: Long-distance spotting potential of bark strips of a ribbon gum (*Eucalyptus viminalis*). *Int. J. Wildland Fire* **24**, 1109–1117.

Hill, A. J., C. C. Weiss, B. C. Ancell, A. J. Hill, C. C. Weiss, and B. C. Ancell, 2016: Ensemble Sensitivity Analysis for Mesoscale Forecasts of Dryline Convection Initiation. Mon. Wea. Rev., 144, 4161-4182, doi:10.1175/MWR-D-15-0338.1.

Holland, G. J., A. H. Lynch, and L. M. Leslie, 1987: Australian East-Coast Cyclones. Part I: Synoptic Overview and Case Study. Mon. Weather Rev., 115, 3024-3036, doi:10.1175/1520-0493(1987)115<3024:AECCPI>2.0.CO;2.

Johnson, R. H., R. S. Schumacher, J. H. Ruppert Jr., D. T. Lindsey, J. E. Ruthford and L. Kriederman, 2014: The role of convective outflow in the Waldo Canyon fire. *Mon. Wea. Rev.*, **142**, 3061—3080.

Kepert, J. D., 2001: The dynamics of boundary layer jets within the tropical cyclone core. Part I: Linear theory. *J. Atmos. Sci*., **58**, 2469–2484, doi:10.1175/1520-469(2001)058,2469:TDOBLJ.2.0.CO;2.

Kepert, J.D., 2013: How does the boundary layer contribute to eyewall replacement cycles in axisymmetric tropical cyclones? *J. Atmos. Sci*., **70**, 2808–2830, doi:10.1175/JAS-D-13-046.1.

Kepert, J.D., 2017: Time and space scales in the tropical cyclone boundary layer, and the location of the eyewall updraft. Accepted for publication, *J. Atmos. Sci.*

Kepert, J. D., and R. J. B. Fawcett, 2013: Meteorological Aspects of the Margaret River Fires of November 2011. 20th International Congress on

Modelling and Simulation, Adelaide, Australia, The Modelling and Simulation Society of Australia and New Zealand Inc., 180–186.

Kepert, J.D. and D.S. Nolan, 2014: Reply to ''Comments on 'How Does the Boundary Layer Contribute to Eyewall Replacement Cycles in Axisymmetric Tropical Cyclones?''' *J. Atmos. Sci*., **71**, 4692-4704, DOI: 10.1175/JAS-D-14-0014.1

Kepert, J.D., and Y. Wang, 2001: The dynamics of boundary layer jets within the tropical cyclone core. Part II: Nonlinear enhancement. *J. Atmos. Sci*., **58**, 2485–2501, doi:10.1175/1520- 469(2001)058,2485:TDOBLJ.2.0.CO;2.

Klemp, J. B., and D. R. Lilly, 1975: The dynamics of wave-induced downslope winds. J. Atmos. Sci., 32, 320–339.

Koo, E., P. J. Pagni, D. R. Weise and J. P. Woycheese, 2010: Firebrands and spotting ignition in large-scale fires. *Int. J. Wild. Fire*, **19**, 818—843.

Lareau, N. P., and C. B. Clements, 2016: Environmental controls on pyrocumulus and pyrocumulonimbus initiation and development. Atmospheric Chemistry and Physics, 16, 4005–4022.

Leslie, L. M. and M. S. Speer, 1998: Short-range ensemble forecasting of explosive Australian east coast cyclogenesis. Wea. Forecast., 13, 822-832, doi:10.1175/1520-0434(1998)013<1205:COSREF>2.0.CO;2.

Locatelli, J. D., M. T. Stoelinga, P. V. Hobbs, and J. Johnson, 1998: Structure and evolution of an undular bore on the high plains and its effects on migrating birds. Bull. Amer. Meteor. Soc., 79,1043–1060.

Long, R. B., 1955: Some aspects of the flow of stratified fluids. III. Continuous density gradients. Tellus, 22, 471–479.

Luderer, G., J. Trentmann and M. O. Andreae, 2009: A new look at the role of fire released moisture on the dynamics of atmospheric pyro-convection. *Int. J. Wild. Fire*, **18**, 554—562.

Luke, R. H., and A. G.McArthur, 1986: Bushfires in Australia. Australian Government Publishing Service, Canberra.

Mason, P. J., and D. J. Thomson, 1987: Large-eddy simulations of the neutral-static-stability planetary boundary layer. Quarterly Journal of the Royal Meteorological Society, 113, 413–443.

McRae, R. H. D., J. J. Sharples, S. R. Wilkes, and A. Walker, 2013: An Australian pyro-tornadogenesis event. Nat. Hazards, 65, 1801–1811.

McArthur, A. G., 1967: Fire behaviour in eucalypt forests. Department of National Development Forestry and Timber Bureau, Canberra, Leaflet 107.

Mills, G.M., 2005: On the subsynoptic scale meteorology of two extreme fire weather days during the eastern Australian fires of January 2003. Australian Meteorological Magazine, 54, 265–290.

Mills, G. M., 2008: Abrupt surface drying and fire weather. Part I: overview and case study of the South Australian fires of 11 January 2005. Australian Meteorological Magazine, 57, 299–309.

Mills, G. A., R. Webb, N. E. Davidson, J. Kepert, A. Seed, and A. D., 2010: The Pasha Bulker east coast low of 8 June 2007. Technical Report 023.

New South Wales Rural Fire Service, 2014: Bush Fire Bulletin. Number 2/2014.

Noble, I. R., G. A. B. Barry, and G. A. M., 1980: McArthur's fire-danger meters expressed as equations. Australian Journal of Ecology, 5, 201–203.

Nolan. D.S., R. Atlas, K. T. Bhatia, and L. R. Bucci, 2013: Development and validation of a hurricane nature run using the joint OSSE nature run and the WRF model. *J. Adv. Model. Earth Syst.*, **5**, 382–405, doi:10.1002/jame.20031.

Peace, M., L. McCaw, B. Santos , J.D. Kepert, N. Burrows, and R.J.B. Fawcett, 2017: Meteorological drivers of extreme behaviour during the Waroona bushfire, Western Australia, January 2016. Submitted to *J. SH. Earth System Science.*

Pendergrass, A. G., and H. E. Willoughby, 2009: Diabatically induced secondary flows in tropical cyclones. Part I: Quasisteady forcing. *Mon. Wea. Rev.*, **137**, 805–821.

Pepler, A. S. and C. S. Rakich, 2010: Extreme inflow events and synoptic forcing in Sydney catchments. IOP Conference Series: Earth and Environmental Science, 11, 012010.

Petch, J. C., and M. E. B. Gray, 2001: Sensitivity studies using a cloudresolving model simulation of the tropical west Pacific. Quarterly Journal of the Royal Meteorological Society, 127, 2287–2306.

Peterson, D. A., E. J. Hyer, J. R. Campbell, M. D. Fromm, J. W. H. C. F. 274 Butler, and M. A. Fenn, 2015: The 2013 Rim Fire: Implications for predicting extreme fire spread, pyroconvection, and smoke emissions. Bulletin of the American Meteorological Society, 96, 229–247.

Peterson, D. A., E. J. Hyer, J. R. Campbell, J. E. Solbrig, and M. D. Fromm, 2017: A conceptual model for development of intense pyrocumulonimbus in western North America. Mon. Weather Rev., 145, 2235–2255.

Potter, B. E., 2005: The role of released moisture in the atmospheric dynamics associated with wildland fires. *Int. J. Wild. Fire*, **14**, 77—84.

Puri, K., G. Dietachmayer, P. Steinle, M. Dix, L. Rikus, L. Logan, M. Naughton, C. Tingwell, Y. Xiao, V. Barras, I. Bermous, R. Bowen, L. Deschamps, C. Franklin, J. Fraser, T. Glowacki, B. Harris, J. Lee, T. Le, G. Roff, A. Sulaiman, H. Sims, X. Sun, Z. Sun, H. Zhu, M. Chattopadhyay, and C. Engel, 2013: Implementation of the initial ACCESS numerical weather prediction system. Aust. Meteorol. Oceanogr. J., 63, 265-284.

Rabenhorst, S., D. N. Whiteman, D. L. Zhang, and B. Demoz, 2014: A Case Study of Mid-Atlantic Nocturnal Boundary Layer Events during WAVES 2006. J. Appl. Meteor. Climatol., 53, 2627–2648.

Rosenfeld, D., M. D. Fromm, J. Trentmann, G. Luderer, M. O. Andreae and R. Servanckx, 2007: The Chisolm firestorm: observed microstructure, precipitation and lightning activity of a pyro-cumulonimbus. *Atmos. Chem. Phys.*, **7**, 645—659.

Rudlosky, S. D and H. E. Fuelberg, 2011: Seasonal, Regional, and Storm-Scale Variability of Cloud-to-Ground Lightning Characteristics in Florida. *Mon. Wea. Rev*., **139**, 1826–1843.

Sanders, F., 1986: Explosive Cyclogenesis in the West-Central North Atlantic Ocean, 1981-84. Part I: Composite Structure and Mean Behavior. Mon. Wea. Rev., 114, 1781-1794, doi:10.1175/1520-0493(1986)114<1781:ECITWC>2.0.CO;2.

Scorer, R., 1949: Theory of waves in the lee of mountains. Quart. J. Roy. Meteor. Soc., 75, 41–56.

Shapiro, L. J. and H. E. Willoughby, 1982: The response of balanced hurricanes to local sources of heat and momentum. *J. Atmos. Sci*., **39**, 378–394.

Simpson, J. E., 1998: Gravity Currents: In the Environment and the Laboratory. Cambridge University Press, 262 pp.

Skamarock, W. C., J. B. Klemp, J. Dudhia, D. O. Gill, D. M. Barker, M. G. Duda, X.-Y. Huang, W. Wang, and J. G. Powers (2008), A description of the advanced research WRF version 3, NCAR Tech. Note, 4751STR, Boulder, Colorado, pp. 113.

Smith, R. B., 1985: On severe downslope winds. J. Atmos. Sci., 42, 2597–2603.

Speer, M. S., P. Wiles, and A. S. Pepler, 2009: Low pressure systems of the New South Wales coast and associated hazardous weather: establishment of a database. Aust. Meteorol. Oceanogr. J., 58, 29-39.

Swann, H., 1998: Sensitivity to the representation of precipitating ice in CRM simulations of deep convection. Atmos. Res., 47–48, 415–435.

Thurston, W., K. J. Tory, J. D. Kepert, and R. J. B. Fawcett, 2014: The effects of fire-plume dynamics on the lateral and longitudinal spread of long-range spotting. *Proceedings of the Research Forum at the Bushfire and Natural Hazards CRC & AFAC 2014 Conference*, M. Rumsewicz, Ed., Bushfire and Natural Hazards CRC, 85–94, ISBN: 978-0-9941696-3-15.

Thurston, W., K. J. Tory, R. J. B. Fawcett and J. D. Kepert, 2016: Large-eddy simulations of pyro-convection and its sensitivity to moisture, *5th International Fire Behaviour and Fuels Conference proceedings.* 6pp.

Thurston, W., J. D. Kepert, K. J. Tory, and R. J. B. Fawcett, 2017: The contribution of turbulent plume dynamics to long-range spotting. International Journal of Wildland Fire, 26, 317–330.

Tory, K. J., 2014: The turning winds with height thermal advection rainfall diagnostic: Why does it work in the tropics? Aust. Meteorol. Oceanogr. J., 64, 231-238.

Tory, K. J. and W. Thurston, 2015: Pyrocumulonimbus: A literature review. *Bushfire and Natural Hazards CRC Report*, NO. 2015.067.

Tory, K. J., M. Peace and W. Thurston, 2016: Pyrocumulonimbus forecasting: Needs and issues. *Bushfire and Natural Hazards CRC Report, NO. 2016.239.*

Trentmann, J., G. Luderer, T. Winterrath, M. D. Fromm, R. Servranckx, M. Herzog, H.-F. Graf and M. O. Andrea, 2006: Modeling of biomass smoke injection into

the lower stratosphere by a large forest fire (Part I): reference simulation. *Atmos. Chem. Phys.,* **6**, 5247—5260.

Vase, J., and Coauthors, 2013: The Australian Water Resource Assessment Modelling System (AWRA). 20th International Congress on Modelling and Simulation, Adelaide, Australia, The Modelling and Simulation Society of Australia and New Zealand Inc., 3015–3021.

Verdon-Kidd, D. C., A. S. Kiem, and G. R. Willgoose, 2016: East Coast Lows and the Pasha Bulker storm - lessons learned nine years on. J. South. Hemisph. Earth Syst. Sci., 66, 152-161, doi:10.22499/3.6002.005.

Vosper, S. B., and D. J. Parker, 2002: Some perspectives on wave clouds. Weather, 57, 3–8.

Wells, T., C. S. Yeo, and R. J. B. Fawcett, 2014: Meteorological and fire behavioural lessons learned from the Aberfeldy Fire, Victoria, 17 January 2013. 2014 Conference of the Australian Fire and Emergency Services Council and the Bushfire and Natural Hazards Cooperative Research Centre., Wellington, New Zealand.

White, P.V.M., 1973: *The Eye of the Storm.* Jonathan Cape, 608pp.

Whiteman, C. D., and J. G. Whiteman, 1974: A historical climatology of damaging downslope windstorms at Boulder, Colarado. NOAA Tech. Rep. ERL336-APCL35, NOAA, 62 pp.

Willoughby, H. E., J. A. Clos, and M. G. Shoreibah, 1982: Concentric eyewalls, secondary wind maxima, and the evolution of the hurricane vortex. *J. Atmos. Sci*., **39**, 395–411.